AD-753 409

THE EFFECT OF PROJECTILE STRENGTH ON CRATER FORMATION

Nicholas C. Byrnside, et al

Air Force Institute of Technology

Prepared for:

Air Force Materials Laboratory

February 1971

Unclassified

Security Classification

DOCUMENT CONTROL DATA - R & D

(Security classification of title, body of abstract and indexing annotation must be entered when the overall report is classified)

1. ORIGINATING ACTIVITY *(Corporate author)*

Air Force Institute of Technology (AFIT-SE)
Wright-Patterson AFB, Ohio 45433

2a. REPORT SECURITY CLASSIFICATION

Unclassified

2b. GROUP

3. REPORT TITLE

THE EFFECT OF PROJECTILE STRENGTH ON CRATER FORMATION

4. DESCRIPTIVE NOTES *(Type of report and inclusive dates)*

Technical Report

5. AUTHOR(S) *(First name, middle initial, last name)*

Captain Nicholas C. Byrnside and Peter J. Torvik

6. REPORT DATE	7a. TOTAL NO. OF PAGES	7b. NO. OF REFS
February 1971	~~101~~ 113	36

8a. CONTRACT OR GRANT NO.

N/A

b. PROJECT NO.

7360

c. Task N. 736006

d.

9a. ORIGINATOR'S REPORT NUMBER(S)

AFML-TR-70-309

9b. OTHER REPORT NO(S) *(Any other numbers that may be assigned this report)*

10. DISTRIBUTION STATEMENT

This document has been approved for public release and sale; its distribution is unlimited.

11. SUPPLEMENTARY NOTES

12. SPONSORING MILITARY ACTIVITY

Air Force Materials Laboratory
Wright-Patterson AFB, Ohio 45433

13. ABSTRACT

The influence of projectile strength on cratering was investigated for projectiles of four aluminum alloys impacting semi-infinite aluminum targets over the velocity range of 1 km/sec to 5.0 km/sec. Final crater dimensions and peak shock pressure were selected as parameters for comparing the influence of projectile strength. The experimental results showed that crater diameters were not significantly influenced by varying projectile strength. The crater depths were found to vary appreciably with strength at lower velocities but to become virtually the same at 3.5 km/sec for the series of projectile alloys investigated. Experimental results for peak shock pressures were inconclusive due to the large scatter in the experimental data.

A simple dynamic model for cratering was developed and compared with experimental results of this study and other AFML experimental results at higher velocities. These comparisons showed that the Model provided predictions of crater diameter which were within 8% for the experimental results of this study and within 13% for the Hypervelocity data. Crater depth predictions showed good agreement with the experimental results of this study for projectiles having greater yield strength than the target material. The predictions of depth as a function of velocity showed qualitative agreement with AFML Hypervelocity data.

DD FORM 1 NOV 65 1473

Unclassified

Security Classification

Security Classification

14. KEY WORDS	LINK A		LINK B		LINK C	
	ROLE	WT	ROLE	WT	ROLE	WT
Impact						
Strength Effects						
Cratering						
Crater Formation						
Penetration						

Security Classification

AFML-TR-70-309

THE EFFECT OF PROJECTILE STRENGTH ON CRATER FORMATION

Nicholas C. Byrnside, Capt., U.S.A.F.
Peter J. Torvik

Air Force Institute of Technology

This document has been approved for public release and sales; its distribution is unlimited.

ic

FOREWORD

This report is based on a thesis prepared by Captain Nicholas C. Byrnside of the Air Force Institute of Technology as partial fulfillment of requirements for the degree of Master of Science under the guidance of Professor Peter J. Torvik and at the suggestion of Mr. H. F. Swift of the University of Dayton Research Institute. The work was administered by Mr. Gordon H. Griffith of the Air Force Materials Laboratory under Project 7360, "Chemical, Physical and Thermodynamic Properties of Aircraft, Missile and Spacecraft Materials," Task 736006, "Impact Damage and Weapons Effects on Aerospace System Materials."

The authors gratefully acknowledge the assistance of Major Ronald Prater of the Air Force Materials Laboratory and members of the staff of the University of Dayton Research Institute, particularly Mr. Diamantis D. Preonas and Mr. Michael F. Lehman for their pertinent advice; and Mr. Michael D. Nagy and Mr. Edward A. Strader for their technical assistance and support under Contract F33615-70-C-1228, Response of Materials to Impulsive Loads.

The manuscript was released by the authors in February 1971 for publication.

This technical report has been reviewed and is approved.

Herbert M. Rosenberg
HERBERT M. ROSENBERG
Chief, Exploratory Studies Branch
Materials Physics Division
Air Force Materials Laboratory

Abstract

The influence of projectile strength on cratering was investigated for projectiles of four aluminum alloys impacting semi-infinite aluminum targets over the velocity range of 1 km/sec to 5.0 km/sec. Final crater dimensions and peak shock pressure were selected as parameters for comparing the influence of projectile strength. The experimental results showed that crater diameters were not signigicantly influenced by varying projectile strength. The crater depths were found to vary appreciably with strength at lower velocities but to become virtually the same at 3.5 km/sec for the series of projectile alloys investigated. Experimental results for peak shock pressures were inconclusive due to the large scatter in the experimental data.

A simple dynamic model for cratering was developed and compared with experimental results of this study and other AFML experimental results at higher velocities. These comparisons showed that the Model provided predictions of crater diameter which were within 8% for the experimental results of this study and within 13% for the Hypervelocity data. Crater depth predictions showed good agreement with the experimental results of this study for projectiles having greater yield strength than the target material. The predictions of depth as a function of velocity showed qualitative agreement with AFML Hypervelocity data.

Contents

Preceding page blank

Contents (continued)

<u>List of Figures</u>

List of Figures (continued)

List of Figures (continued)

Figure | Page

<u>List of Tables</u>

THE EFFECT OF PROJECTILE STRENGTH ON CRATER FORMATION

I Introduction

Background

The question of what happens when two bodies impact at some velocity has challenged man for years. The initial interest rose out of the quest by the military arms makers to develop armor which could defeat projectiles. This quest has been characterized by Charters as a contest between stronger armor and faster projectiles (Ref 6:128). One of the milestones in this contest occurred during World War II when armor was developed which defeated the heaviest projectile an antitank gun could fire, at velocities up to 3,000 ft/sec. The projectile velocity could have been increased, but it would have been of little or no help. At higher velocities the strongest projectiles simply shattered upon impact and their penetration failed to increase or even decrease (Ref 6:128).

More recently, methods for protecting spacecraft from meteoroids have become necessary. Part of the research in this area has involved launching projectiles at hypervelocity (velocity greater than the speed of sound in the target material) so as to impact metal targets (Ref 32:1). The craters produced by hypervelocity projectiles impacting semi-infinite targets are roughly spherically symmetrical (Ref 11:242). This spherical symmetry seems to show that the cratering process in this velocity region is hydrodynamic (Ref 6:134).

Investigation of projectiles impacting between the low velocity and hypervelocity range has been very limited. As a consequence, little information is available on the effect of projectile material strength in this velocity region.

In Fig. 1, after Charters, the velocity impact spectrum is broken up into three regions. The first region is characterized by the unbroken projectile and constitutes the classical low velocity region. The transition region is next and is characterized by the projectile fragmenting upon impact and includes the traditional high velocity region. The last region is called the fluid impact region and is characterized by the projectile acting as a fluid impactor. This last region is analogous to the hypervelocity or hydrodynamic region (Ref 6:128).

Most authors and researchers have devoted their interest to either the unbroken projectile or the fluid impact regions. Their interests were motivated by the specific needs (i.e., armor design for combat or spacecraft protection), thus the transition region has been neglected to a large degree except for the recognition of its existence and the shifting of its starting and ending points with projectile and target material properties.

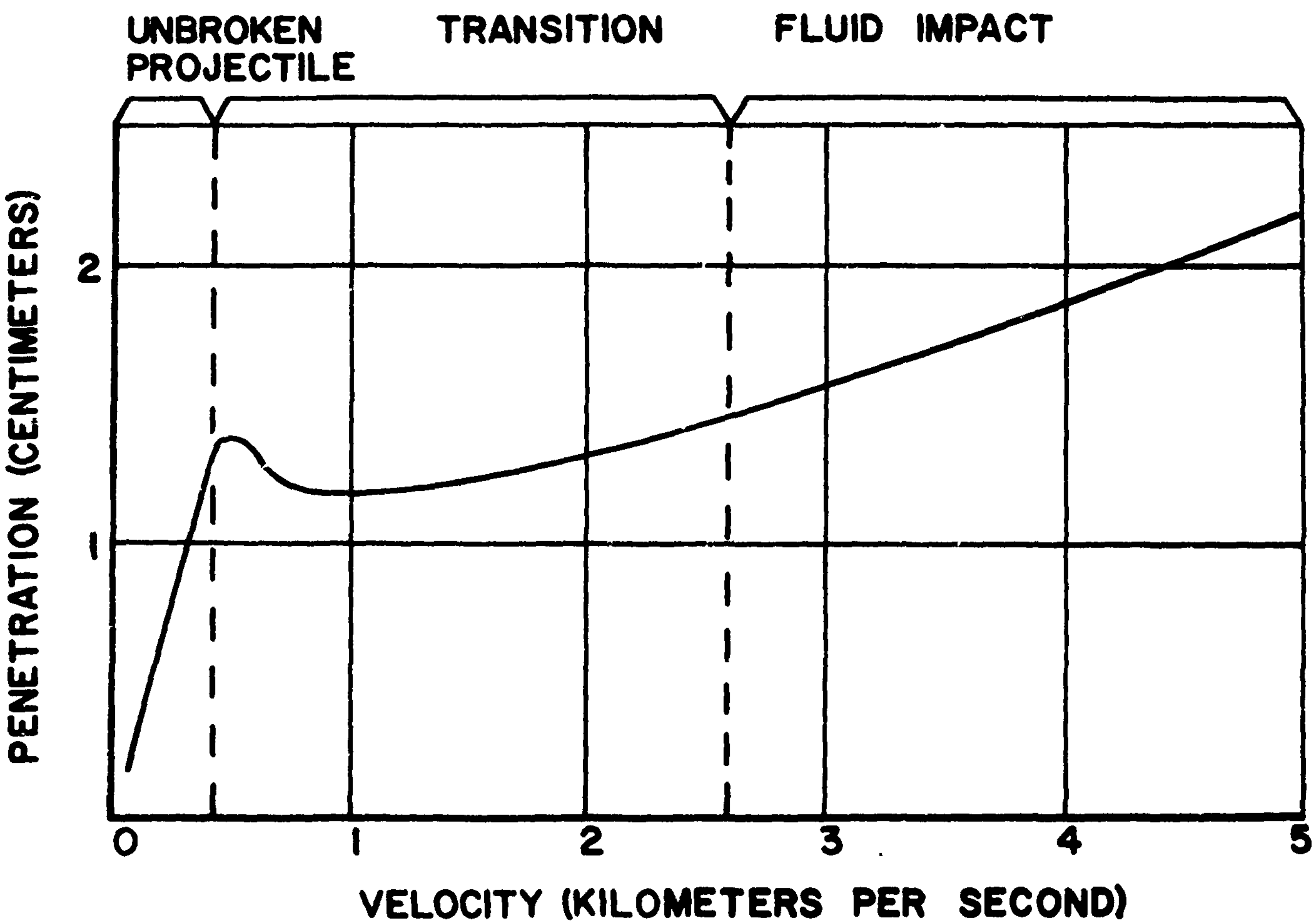

Fig. 1. Impact Spectrum (Ref 6:129)

Objective

In light of the foregoing discussion, it is evident that a significant gap exists in our understanding of impacts in the transition region. The purpose of this study is to help bridge this gap. To achieve this purpose the following objectives were set:

a. Formulate a mathematical description of the cratering event.

b. Devise experimental procedures and conduct experiments to establish the projectile strength effects on crater formation.

Final crater dimensions and target shock pressure were selected as parameters for comparing projectile material properties effects. As a consequence, the experimental procedures were keyed to observe and measure these quantities over the impacting velocity range of 1.0 to 5.0 km/sec.

II. Postulated Model for Cratering in Semi-Infinite Targets

In order to establish relationships between crater formation and the material properties of impacting projectile and target, it was necessary to postulate a model for the cratering process. In spite of disagreements on the importance and effect of material properties on the actual cratering process, most investigators concur that crater formation in thick targets occurs in the following stages. Projectile penetrates target surface generating a shock wave. Cavity expansion (cavitation) ensues behind this shock wave. The expansion rate of the crater decreases and the shock wave is detached from the crater surface. Projectile and target material flows along the walls of the crater and a portion of this material is ejected. Crater expansion continues until it is arrested by the dynamic strength of the material (Ref 30:9).

The recent developments in the "hydrodynamic codes" provide powerful techniques for theoretically predicting the crater growth and final crater dimensions. These numerical methods are complicated and require very fast computers with large memory capacity (Ref 27:17-24, 94-104). The cost of using these methods for predicting cratering results limit their application. With these considerations in mind, a simple model for cratering was sought.

In Ref 11, Goodier formulates the dynamics of cratering in

stages which are associated with the kinetic energy of the impacting projectile. A brief discussion of these theories is presented first, then a coupled cratering theory is presented.

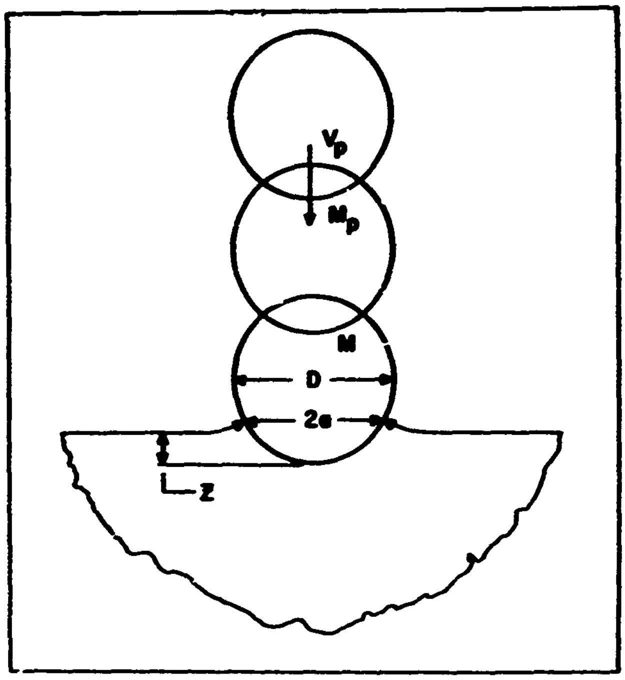

Fig. 2 Rigid Penetrator (Ref 11:221)

Rigid Penetrator Theory (Goodier)

In this theory, the projectile is considered as a rigid Brinell indenter with penetration up to one projectile radius. Figure 2 is a schematic representation of this process. Considering the projectile to be a rigid sphere of mass M_p, diameter D, and to impact the target with a normal velocity V_p, at some time t, the depth of penetration is Z and the crater diameter is 2a. Thus from geometry we have

$$2Z = D - \sqrt{D^2 - 4a^2} \tag{1}$$

Assuming the material to obey Meyer's law (Ref 11:220), the force resisting the sphere at time t is

$$F_r = k(2a)^n \tag{2}$$

where k and n are constants of the material. Now from the work energy relationship, we have

$$\frac{1}{2} M_p V_p^2 = \int_{Z=0}^{Z=Z_f} k(2a)^n dZ \tag{3}$$

where Z_f is the depth at which penetration ceases. Using Equation 1 this becomes

$$\frac{1}{2} M_p V_p^2 = k \int_0^d \frac{(2a)^{n+1}}{\sqrt{D^2 - 4a^2}} da \tag{4}$$

where d is the final radius of the indentation.

The Meyer index n for fully work-hardened metals is close to 2. Using this value, the Meyer coefficient k obeys the following relationship:

$$k = 2.77 Y \tag{5}$$

where Y is yield stress (value of stress at which plastic deformation becomes measurable) of the target material expressed in pounds per square inch (Ref 11:224). Hence Equations 4 and 1 with n = 2 and k given by Equation 5 prescribes the crater parameters d and Z for penetration up to one-half projectile diameter.

Cavity Expansion Theory (Goodier)

In this theory, the projectile is assumed to undergo gross deformation. The crater produced is assumed to be hemispherical and the pressure exerted on the crater surface is assumed uniform. The process can be considered as the detonation of a point explosive at point "0" of Fig. 3, resulting in the uniform pressure distribution P as shown. The radius of the hemispherical crater at some time t is r.

In Ref 15, Hopkins derives the following equation which is the solution to the problem of the large expansion of a spherical cavity by internal pressure when the material is considered incompressible elastically as well as plastically:

$$P = \frac{2}{3} Y_t \left(1 + \ln \frac{2E}{3Y_t} \right) + \frac{2}{27} \pi^2 E_t + \rho_t \left(r\ddot{r} + \frac{3}{2}\dot{r}^2 \right) \tag{6}$$

where Y_t = target yield stress

E = Young's modulus

ρ_t = target density

E_t = tangent modulus for linear strain-hardening in true stress-true strain

r = cavity radius at some time t

$\dot{r} = \frac{dr}{dt}$

$\ddot{r} = \frac{d^2r}{dt^2}$

letting

$$P_1 = \frac{2}{3} Y_t \left(1 + \ln \frac{2}{3} \frac{E}{Y_t}\right) + \frac{2}{27} \pi^2 E_t \tag{7}$$

then

$$P = P_1 + \rho_t \left(r \ddot{r} + \frac{3}{2} \dot{r}^2\right) \tag{8}$$

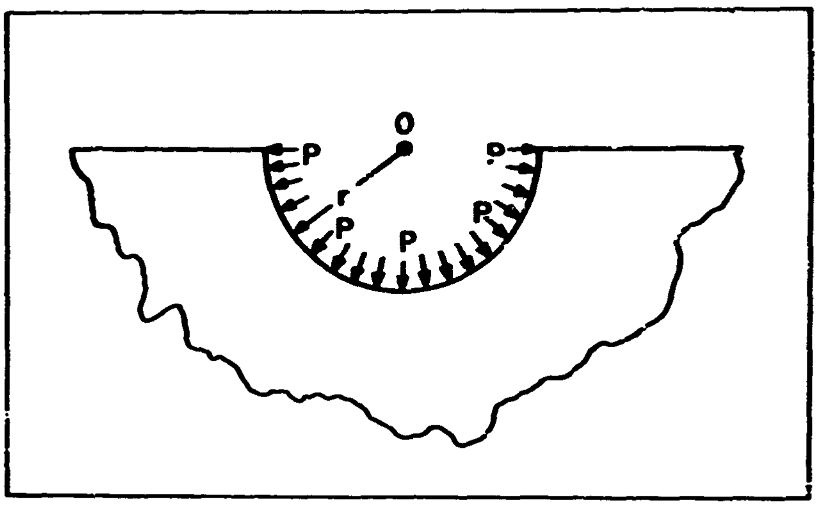

Fig. 3 Cavity Expansion

The work done in expanding the cavity from zero radius to some radius r can be found as follows:

$$W = \int_0^r PA \, dr \tag{9}$$

where A is surface area of the hemispherical shell. Thus,

$$W = \frac{2\pi r^3 P_1}{3} + \pi \rho r^3 \dot{r}^2 \Big]_{\text{initial configuration}}^{\text{final configuration}} \tag{10}$$

From work-energy considerations and assuming that cavity expansion ceases when $r_f = a_2$, $\dot{r}_f = 0$, and initial conditions of $r_i = 0$ yields

$$\frac{1}{2} M_p V_p^2 = \frac{2\pi r^3}{3} P_1 + \pi \rho r^3 \dot{r}^2 \Big]_{\text{initial}}^{\text{final}} \tag{11}$$

or

$$a_2 = \frac{D}{2}\left(\frac{\rho}{P_1} V_p^2\right)^{\frac{1}{3}} \tag{12}$$

Since the Cavity Expansion model is hemispherical, Equation 12 also provides a prediction of the depth of penetration.

Deep Penetration (Goodier)

For the case where the kinetic energy of the impacting projectile is greater than the energy required to produce a crater with depth of a projectile radius as prescribed by the Rigid Penetrator Theory and not great enough to cause the projectile to undergo gross deformation, Goodier proposed the Deep Penetration Theory to account for the inertia of the target material being displaced by the projectile and target strain hardening.

During the Deep Penetration phase the projectile is assumed to be a rigid sphere and experience a resisting pressure on its frontal surface similar to that described by Equation 8 (Ref 11:230). Taking the static part, P_1, of the pressure as acting over the entire hemispherical surface, for the point A of Fig. 4, it is reasonable to identify the r with the projectile radius D/2 for the dynamic part of Equation 8. Likewise $\ddot{r}$ and $\dot{r}$ can be related to $\ddot{q}$ and $\dot{q}$ respectively, where q is defined as the depth of penetration measured from the initial surface to the lower surface of the projectile. At point C the radial velocity and acceleration are zero, thus the dynamic pressure is zero also. Recognizing that the pressure at point C in Fig. 4 is likely less than the pressure at point A due to the fact that the flow at C is tangential to the surface, a factor of cosine θ was introduced into the dynamic portion of the pressure distribution on the surface of the projectile. After integrating the pressure over the hemispherical

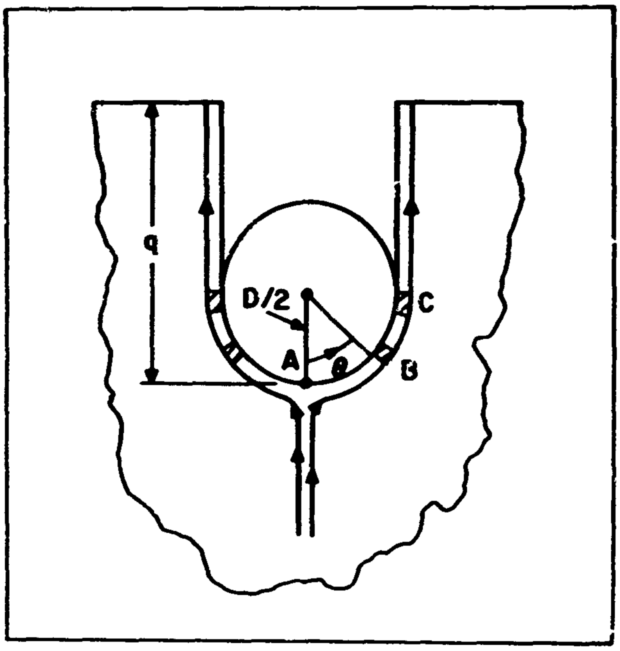

Fig. 4 Deep Penetration (Ref 11:232)

surface, the average pressure on the frontal part of projectile (analogous to Equation 8) is found to be:

$$P = P_1 + \frac{2}{3}\rho_t\left(\frac{D}{2}\ddot{q} + \frac{3}{2}\dot{q}^2\right) \tag{13}$$

the resulting resistive force is

$$F_r = \frac{\pi}{4} D^2\left[P_1 + \frac{2}{3}\rho_t\left(\frac{D}{2}\ddot{q} + \frac{3}{2}\dot{q}^2\right)\right] \tag{14}$$

From Newton's second law, the dynamical equation for the sphere is

$$-M_p\ddot{q} = \left[P_1 + \frac{2}{3}\rho_t\left(\frac{D}{2}\ddot{q} + \frac{3}{2}\dot{q}^2\right)\right]\frac{\pi}{4} D \tag{15}$$

After the following substitutions,

$$\ddot{q} = \dot{q}\,\frac{d\dot{q}}{dq} \tag{16}$$

$$M_p = \frac{4}{3}\pi\left(\frac{D}{2}\right)^3 \rho_p \tag{17}$$

Equation 15 may be integrated between initial and final values of q and $\dot{q}$. The result of this integration is

$$-\left.\frac{6\rho_t q}{D(2\rho_p + \rho_t)}\right]_{q_{initial}}^{q_{final}} = \ln(\rho_t\dot{q}^2 + P_1)\Big]_{\dot{q}_{initial}}^{\dot{q}_{final}} \tag{18}$$

Taking $\dot{q}$ (initial) = V_1, q (initial) = D/2, $\dot{q}$ (final) = $\dot{q}$, and q (final) = q, Equation 18 becomes

$$\ln(P_1 + \rho_t\dot{q}^2) - \ln(\rho_t V_1^2 + P_1) = -\frac{6\rho_t}{D(2\rho_p + \rho_t)}\left(q - \frac{D}{2}\right) \tag{19}$$

Rewriting yields

$$\ln\left(\frac{\rho_t V_1^2 + P_1}{\rho_t \dot{q}^2 + P_1}\right) = \left(q - \frac{D}{2}\right) \frac{6\,\rho_t}{D(2\rho_p+\rho_t)} \tag{20}$$

Now considering $\dot{q}$ (final) = 0, we can solve for q as follows:

$$q = \frac{D}{2} + \frac{D}{6}\left(2\,\frac{\rho_p}{\rho_t} + 1\right) \ln\left(\frac{\rho_t V_1^2}{P_1} + 1\right) \tag{21}$$

where V_1 is the velocity of the projectile at the start of this phase, rather than the initial impact velocity. Thus Equation 21 yields a prediction for crater depth if Deep Penetration by a rigid spherical projectile is the method of cratering. The velocity V_1 can be obtained from the Rigid Penetrator Theory with the following results

$$V_1^2 = V_p^2 - \frac{4}{\pi}\frac{k}{\rho_p} \tag{22}$$

Discussion

The Rigid Penetrator and Deep Penetration models as presented by Goodier were coupled through the velocity V_1, where V_1 was the velocity at termination of Penetrator phase and initiation of Deep Penetration phase. The Cavity Expansion model was used by Goodier as a separate model of particular importance in the higher velocity ranges. In his development, Goodier compared the predicted results of these models with experimental results and found that they gave results which were of at least the same order of magnitude as experimentally measured values (Ref 11:239-242).

It is our view that the theories discussed previously are not applicable at intermediate velocities, for they fail to provide for simultaneous penetration and cavity expansion. In this range, cratering cannot be regarded as strictly a cavity expansion phenomenon or as strictly penetration.

Coupled Model

The cratering process is divided into three phases, as shown in Fig. 5. In the first phase, the projectile is considered to be a rigid penetrator for penetration up to a half diameter as in Goodier's Rigid Penetrator Theory. Equations 1 and 4 give predictions of the crater depth and diameter respectively if the impact velocity is not great enough to produce a crater with depth equal to half a projectile diameter.

If the projectile kinetic energy is such that there is energy left after the projectile has penetrated to half a diameter, the cratering process is assumed to begin. At this point, the projectile is assumed to deform and the cavity is assumed to simultaneously expand radially and to translate. This process is termed Cavity Expansion (Fig. 5, Phase II). Taking the start of Phase II to be at penetration to half projectile diameter, from the Rigid Penetrator Theory (Phase I), we have

$$V_1^2 = V_p^2 - \frac{4}{\pi}\frac{k}{\rho_p} \tag{23}$$

where V_1 is the velocity at the beginning of Phase II.

Adding an estimate of the work done in deforming the projectile to the work required to expand the cavity from the initial radius D/2 to the final value r leads to a modified form of the Cavity Expansion Theory (Equation 11).

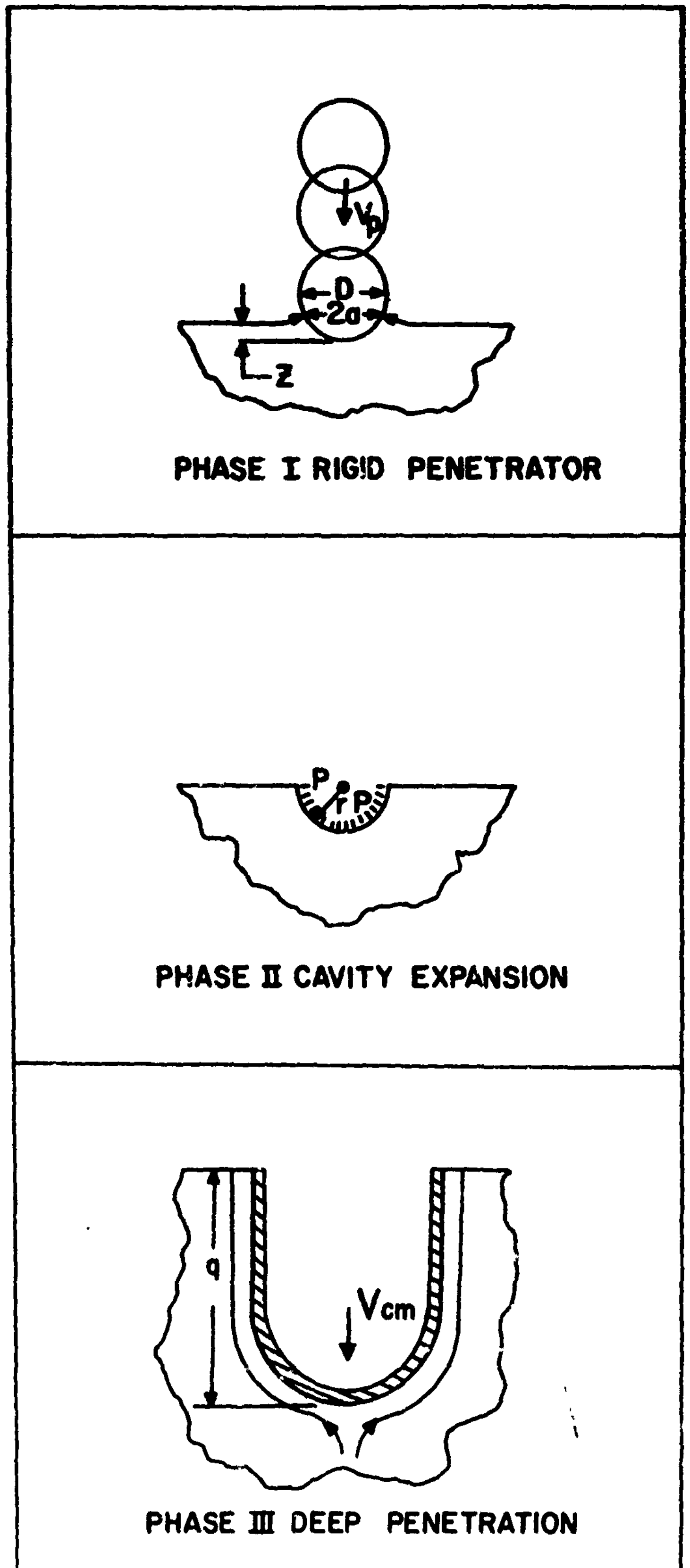

Fig. 5 Coupled Model

$$\frac{1}{2} M_p V_1^2 = \int_{\frac{D}{2}}^{r} PA \, dr + Y_p D^3 \tag{24}$$

where P is prescribed by Fquation 8, A is the frontal surface area of the hemisphere, M_p is the mass of the projectile, and $Y_p D^3$ is an approximation of the work required to deform the projectile. This approximation was proposed by Goodier[7] who noted that it is negligible compared to the kinetic energy, in the hypervelocity region. At velocities in the transition region (Fig. 1), it can, however, be significant. Equation 24 then becomes

$$\frac{1}{2} M_p V_1^2 - Y_p D^3 = \frac{2}{3} P_1 \pi r^3 + \pi \rho_t r^3 \dot{r}^2 \Big]_{\text{initial configuration}}^{\text{final configuration}} \tag{25}$$

with the initial and final values of $\dot{r}$ assumed to be zero, while r increases from D/2. Solving for the final radius, r_1, yields

$$r_1 = \left(\frac{3}{2P_1\pi}\right)^{\frac{1}{3}} \left[\frac{1}{2} M_p V_1^2 + \frac{2}{3} P_1 \pi \left(\frac{D}{2}\right)^3 - Y_p D^3\right]^{\frac{1}{3}} \tag{26}$$

Equation 26 is a modified form of the Cavity Expansion model due to Goodier and given as Equation 12.

We now assume that during Cavity Expansion the mass of the projectile and displaced target material

$$M_{s1} = M_p + \frac{2}{3} \pi \rho_t \left[r^3 - D^3/8\right] \tag{27}$$

is contained in a uniform hemispherical shell of radius r. The mass of target material $2/3\ \pi\ \rho_t D^3/8$ was assumed to be displaced statically during Phase I. The projectile and displaced target material are assumed to be initially traveling at speed V_1, but are retarded by the pressure force. From the principle of impulse and momentum,

$$M_pV_1 - M_{s1}V_{cm} = \int_{t_1}^{t_2} P_1 A \, dt \tag{28}$$

where P_1 is static pressure prescribed by Equation 7. V_{cm} is the velocity of the center of mass of the hemispherical shell containing M_{s1}, t_1 corresponds to the end of Phase I, and t corresponds to the time when the radius has reached r. Rewriting Equation 28 yields

$$M_pV_1 - M_{s1}V_{cm} = 2P_1\pi \int_{t_1}^{t_2} r^2 \, dt \tag{29}$$

Using Equation 25, but with final conditions of r and $\dot{r}$, and solving for r, we have

$$\dot{r} = \left\{ \left(\frac{1}{\pi \rho_t r^3} \right) \left[\frac{1}{2} M_p V_1^2 - Y_p D^3 + \frac{2}{3}\pi P_1 \left(\frac{D^3}{8} - r^3 \right) \right] \right\}^{\frac{1}{2}} \tag{30}$$

Substituting

$$dt = \frac{dr}{\dot{r}} \tag{31}$$

and Equation 30 into 29 yields

$$M_pV_1 - M_{s1}V_{cm} = 2P_1\pi\sqrt{\pi\rho_t} \int_{\frac{D}{2}}^{r_1} \frac{r^{\frac{7}{2}} \, dr}{\sqrt{\frac{1}{2}M_pV_1^2 - Y_pD^3 + \frac{2}{3}\pi P_1(\frac{1}{8}D^3 - r^3)}} \tag{32}$$

Making the substitutions

$$c = \frac{1}{2}M_pV_1^2 - Y_pD^3 + \frac{2}{3}P_1\pi\left(\frac{D}{2}\right)^3 \tag{33}$$

$$b = \frac{2}{3}\pi P_1 \tag{34}$$

Equation 32 reduces to

$$M_pV_1 - M_{s1}V_{cm} = 2P_1\pi\sqrt{\pi\rho_t} \int_{\frac{D}{2}}^{r_1} \frac{r^{\frac{7}{2}} \, dr}{\sqrt{c - br^3}} \tag{35}$$

which integrates to

$$M_p V_1 - M_{s1} V_{cm} = \frac{2}{3}\pi P_1 \sqrt{\pi \rho_1}\left[-\frac{1}{b}\sqrt{c r_1^3 - b r_1^6} - \right.$$

$$\left. \frac{c}{b\sqrt{b}} \arcsin\sqrt{\frac{c - b r_1^3}{c}} + \frac{1}{b}\sqrt{c\left(\frac{D}{2}\right)^3 - b\left(\frac{D}{2}\right)^6} + \frac{c}{b\sqrt{b}} \arcsin\sqrt{\frac{c - b\frac{D^3}{8}}{c}}\right] \quad (36)$$

We may now compute the translation of the shell during the expansion phase. The velocity of the center of mass of the hemispherical shell assumed to contain the mass of projectile and target material displaced during Phase II is given by Equation 36. The translation of the center of mass can be determined from

$$x_{cm} = x_0 + \int_{t_1}^{t} V_{cm}\, dt \quad (37)$$

$$= x_0 + \int_{D/2}^{r} \left[V_{cm}/\dot{r}\right] dr \quad (38)$$

With Equation 36 being solved for V_{cm} and Equation 30 employed for $\dot{r}$. No attempt was made to integrate Equation 38 in closed form, but numerical integration was found to present no difficulty. The range of r was divided into equal increments, Δr. At the end of the first increment, the radius r is

$$r = D/2 + \Delta r \quad (39)$$

Substituting this into Equation 35 provides a value for V_{cm} at $r = D/2 + \Delta r$. An average V_{cm} over the interval may be defined as

$$V_{cm_{avg}} = \frac{V_{cm(D/2)} + V_{cm(D/2+\Delta r)}}{2} \quad (40)$$

where

$$V_{cm(D/2)} = V_1$$

An average radius over this increment is

$$r_{avg} = D/2 + \Delta r/2 \tag{41}$$

and an average $\dot{r}$ may be computed from Equation 30. The time required for the cavity to expand the increment Δr and the translation of the center of mass during this interval may now be computed

$$\Delta t = \Delta r/\dot{r}_{ave} \tag{42}$$

$$\Delta q = \Delta t \cdot V_{cm_{ave}} \tag{43}$$

The total translation of the center of mass during the cavity expansion phase is obtained by repeating the above process for n increments and summing the values of Δq.

The velocity of the center of mass, as determined from Equation 36, may go to zero before the cavity expansion phase (Phase II) ends. In this case, the depth of the crater bottom below the initial surface is given by

$$q = x_{cm_o} + \int_{t_1}^{t} V_{cm}\,dt - x_{cm_{rel}} + r \tag{44}$$

where x_{cmo} is the distance from the initial surface to the center of mass at $t = t_1$

$x_{cm_{rel}}$ is the distance from the base plane of the hemisphere to the center of mass at time t, and r is the crater radius at that time. The center of mass of a hemispherical shell of inner radius r_i and outer radius r_o is located at a distance

$$x_{cm} = \frac{3}{8} r_o \frac{1-(r_i/r_o)^4}{1-(r_i/r_o)^3} = f r_o \tag{45}$$

from the base plane. f is between 3/8 and 1/2, depending on the thickness of the shell.

The final crater depth in the case where translation terminates during Phase II is therefore

$$q_1 = r_f + \int_{D/2}^{r_f} V_{cm} \frac{dr}{\dot{r}} - f(r_f - D/2) \tag{46}$$

where the integration is to be performed numerically, as described earlier.

If the velocity V_{cm} is not yet zero at the time when cavity expansion ceases (the end of Phase II), an additional translation, (Phase III of Figure 5) analogous to Goodiers Deep Penetration Theory will take place after the expansion ceases. The mass of the shell is assumed to remain constant during this phase. Substituting Equation 33 and 34 into 26 yields

$$r_1 = (c/b)^{1/3} \tag{47}$$

as the final value of crater radius. Substituting this into Equation 36 yields a value for the velocity of the center of mass at the end of Phase II of

$$V_{cm_1} = \left\{ M_p V_1 - \frac{2}{3}\pi P_1 \sqrt{\pi \rho_1} \left[\frac{1}{b}\frac{D}{2}\sqrt{\frac{cD}{2} - \frac{bD^4}{16}} + \frac{c}{b\sqrt{b}} \arc\sin\sqrt{\frac{c - \frac{bD^3}{8}}{c}} \right] \right\} \left(\frac{1}{M_{s1}} \right) \tag{48}$$

Once again, the force retarding the translation is assumed to be the resultant of the pressure distribution given by Equation 11. Thus

$$-M_{s1}\ddot{q} = \pi r_1^2 \left[P_1 + \frac{2}{3}\rho \left(r_1 \ddot{q} + \frac{3}{2}\dot{q}^2 \right) \right] \tag{49}$$

Integration yields

$$q\Big]_{\text{initial}}^{\text{final}} = \frac{M_{s1} + \frac{2}{3}\pi \rho_t r_1^3}{2\pi \rho_t r_1^2} \ln(\rho_t \dot{q}^2 + P_1)\Big]_{\text{initial}}^{\text{final}} \tag{50}$$

with the limits of integration being: $q_{initial} = V_{cm_1}$; $q_{final} = o$; $q_{initial} = q_i$; $q_{final} = q_1$. The final expression for the depth is then

$$q_2 = q_1 + \frac{M_{s1} + \frac{2}{3}\Pi \rho_t r_1^3}{2\Pi \rho_t r_1^2} \ln\left(1 + \frac{\rho_t V_{cm}^2}{P_1}\right) \tag{51}$$

<u>Observations.</u> From Equations 26 and 51, the Coupled Model provides a means of predicting crater dimensions if V_1, computed from Equation 22, is greater than zero. It was assumed that the mass displaced during Phase II as well as the mass of the original projectile is distributed in a shell of uniform thickness. For a relatively soft projectile impacting at moderate velocity, it has been observed that the crater is coated with a thin shell of the projectile material, lending credence to such an assumption. The shell depth has been measured in craters formed by hypervelocity impact (Ref 7:64).

The ejecta resulting from the impact has not been considered. Since the momentum of the ejecta is of opposite sign to the momentum of the mass in front of the translating cavity, it is expected that the theory will under predict the depth of the cavity.

The mode of cratering assumed by an inclusion of Phase I (Rigid Penetration) limits the application of this Coupled Model to impacts where the projectile strength is significantly greater than the target strength so that the projectile initially acts as a rigid penetrator

III. Experimental Approach

General

In order to establish the relationships between crater dimensions, peak shock pressure and projectile material strength, a series of experiments were conducted. In all experiments the target material was 6061-H aluminum and the projectiles were 0.9525 cm diameter spheres of different aluminum alloys, these alloys being: 1100-T0, 6061-T6, 2017-T4, and 7075-T6. Primary interest was placed on examination of impacts at 1.0 to 5.0 km/sec into semi-infinite targets (5.08 cm thick by 8.89 cm diameter cyclinders).

Fragment Launch Range

The AFML fragment launch range was used for all shots in this experimental program except for those at velocities greater than 2.9 km/sec. The AFML light-gas gun used for the highest velocity shots is described in the next section. A brief description of the range setup and facility instrumentation as applied to this investigation is included here. Figure 6 shows the component parts of the facility and Ref 1 contains a complete description of the facility.

The fragment launch range uses a conventional research gun to launch a projectile with principal dimensions up to 1.27 cm at velocities of up to 3 km/sec. Viewing ports and instrumentation along trajectory permit various dynamic measurements.

Figure 7 shows the range set up for firing the lower velocity

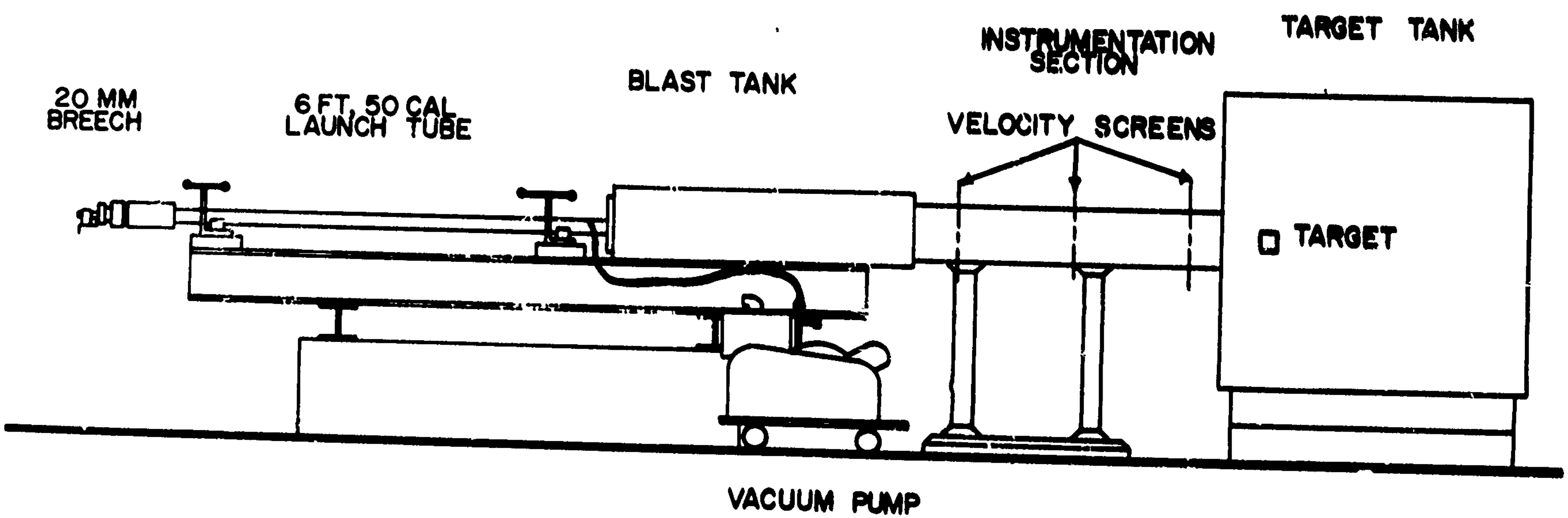

Fig. 6. Component Parts of Fragment Launch Range

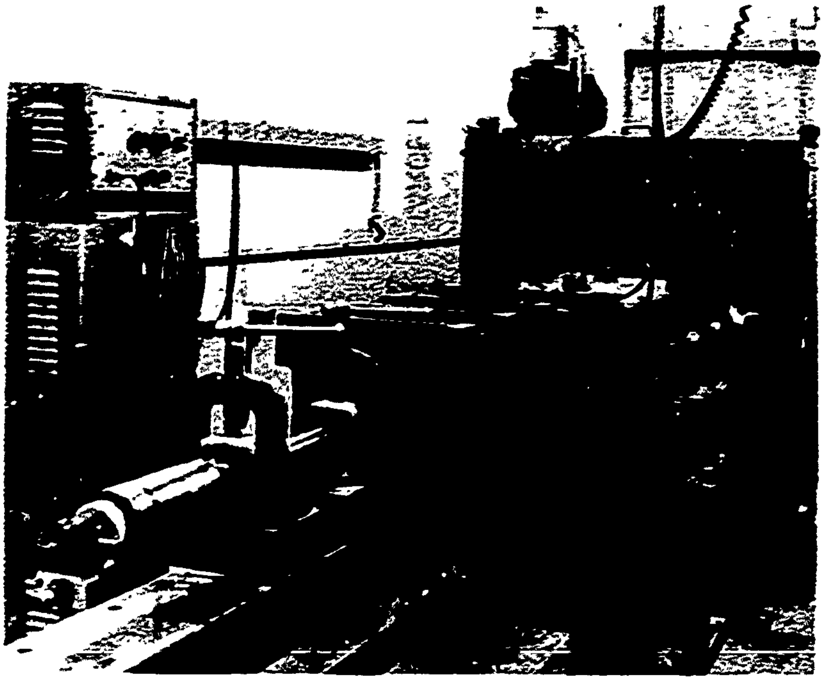

Fig. 7. Fragment Launch Range Setup for Low Velocity Shots

shots (less than 1.6 km/sec). In this configuration a five foot standard research barrel is used with a twelve gage shotgun shell with varying amount of powder providing the propulsion.

The range setup for the medium velocity shots (1.6 to 2.6 km/sec) is shown in Fig. 8. A six foot standard research barrel is used, however it has been modified so that the bore can be evacuated. In addition, a petal valve with shear disk was installed in the breach to aid in pressure buildup. A 20 mm shell with varying amounts and types of powder was used for propulsion.

Figure 8 shows the configuration for the highest velocities (up to 2.83 km/sec) achieved on the open air fragment range. The

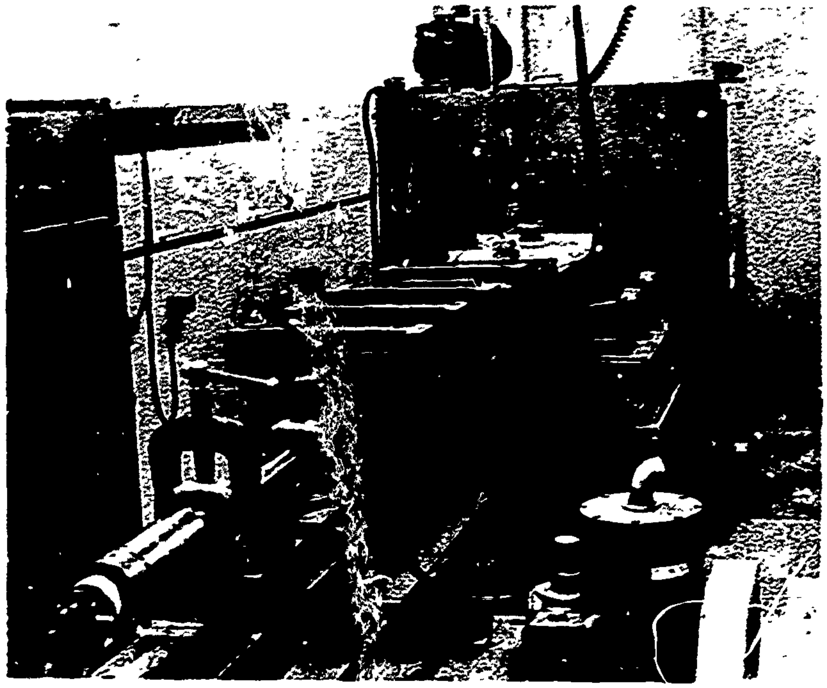

Fig. 8. Fragment Launch Range Setup for Medium and High Velocity Shots

configuration is the same as for the description for the medium velocity shots, except that a ten foot barrel was used.

The range setups described and shown in the figures were the final results of range modifications to overcome problems as they arose in the course of the experiments.

Fragment Launch Range Experimental Procedures

Fifty caliber barrels were used for launching the aluminum spheres. The required velocities were obtained by varying the range setup as described previously and by varying the powder charge. Two section sabots (Fig. 9), which are separated by aerodynamic drag, were used to hold the projectile during launching.

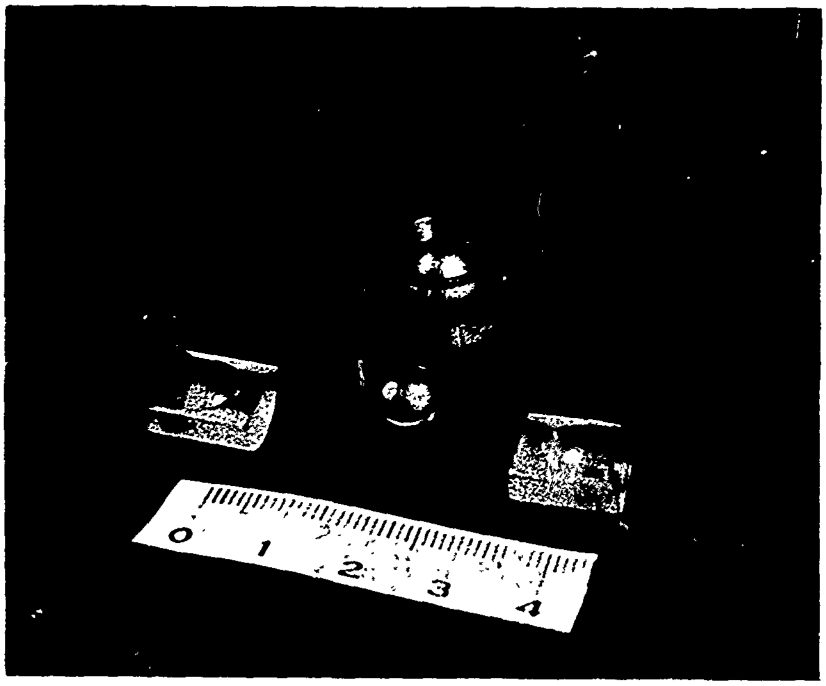

Fig. 9. Two Section Sabot and Projectile

Velocity Determination. The average projectile velocity was obtained by measuring the elapsed time of travel between two contact screens placed 0.915 meters apart. An Eldorado Model 1410 Counter Timer was the time measuring instrument. The effect of velocity loss between measured point and impact due to drag, discussed in Appendix A, was found to be no more than 2.5 percent.

Shock Pressure Measurement. Figure 10 shows the basic mechanism of the "flyer" technique used to measure the free surface velocity. When a target is impacted by a projectile, a spherical disturbance is generated at the impact point and propagated through the target material. After traveling a short distance into the target, the shock profile is established as shown in Fig. 10 (b). Neglecting the

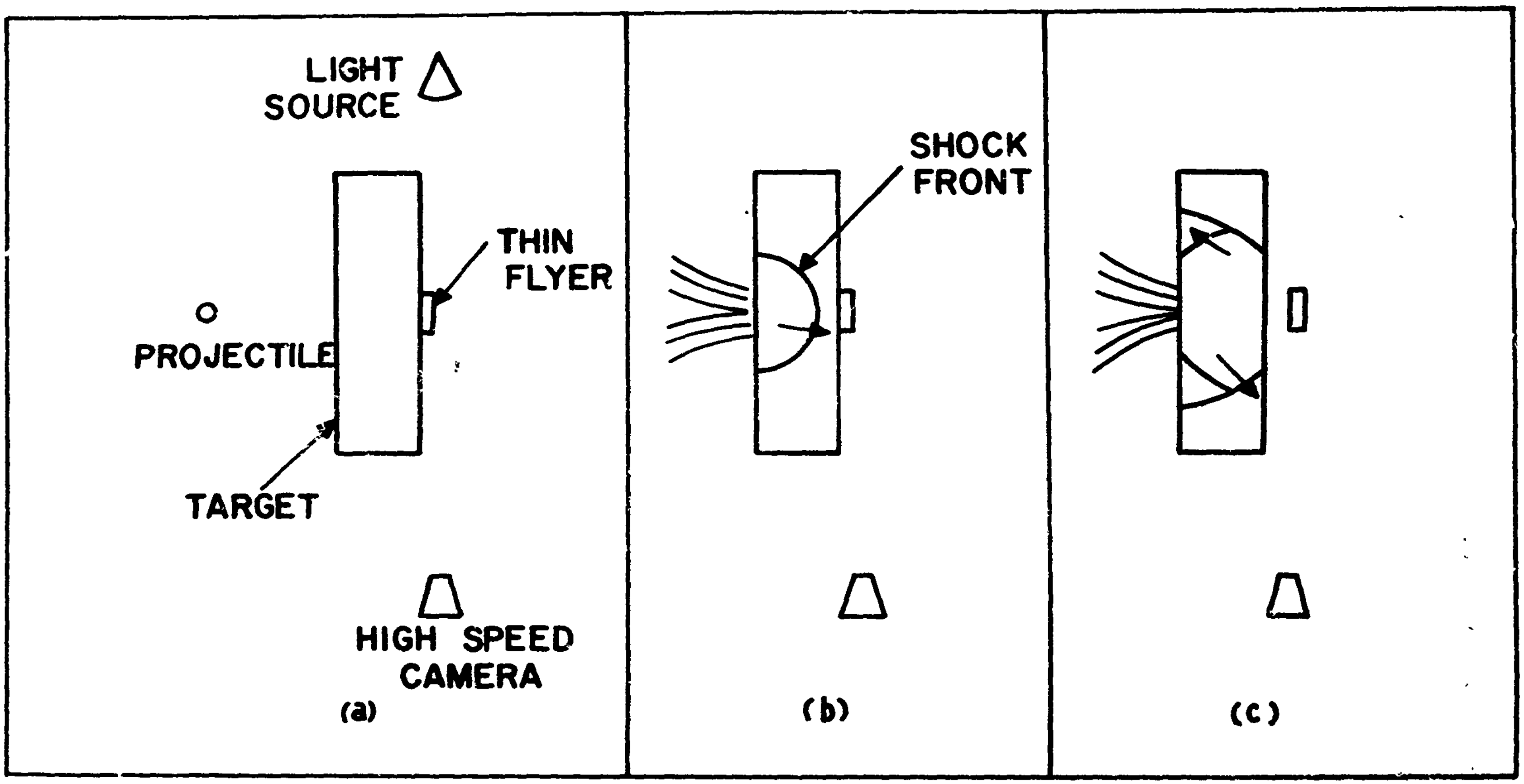

Fig. 10 "Flyer" Technique (Ref 10:179)

effect of rarefaction waves generated at the interface, the shock wave enters the flyer across the interface. After reaching the free surface of the flyer, the compression shock wave is reflected as a tension wave which moves back through the flyer. Assuming the bond between target and flyer to be of zero strength, at the instant that the stress at the interface goes into tension, the flyer will fly off with a velocity which is twice that of the material velocity in the target material (Ref 10:178-180). Using this free surface velocity to determine the particle velocity, then applying the Rankine-Hugoniot jump condition as described in Appendix C, enables a calculation of the shock pressure.

Three 0.6 cm diameter by 0.03 cm thick flyers were attached to the vertical centerline of the back of the targets as shown in Fig. 11. An essentially zero strength bond was achieved by using a thin film of vacuum grease between the target and flyers. To eliminate the effect of drag on the flyers, a 8.25 cm by 5.0 cm by 5.0 cm Plexiglas® box with a hole drilled and taped in one side to permit connection of vacuum pump was placed over the flyers, glued to the target, and evacuated (Fig. 12).

A Wollensak Fastax high speed motion picture camera was used to measure the flyer velocities. The procedure was as follows: a Wollensak Goose Control Unit was used as the control unit for operating the Fastax Camera and firing the gun. When the range was ready, the Goose control unit was triggered which in turn started the camera and at a preset time delay emitted a signal to fire the gun. The time delay

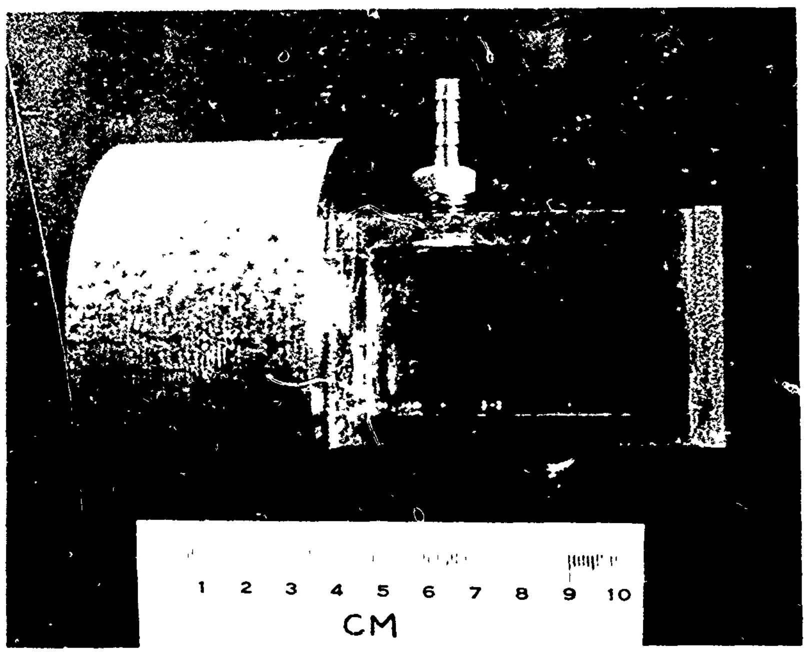

Fig. 11 Flyer Configuration

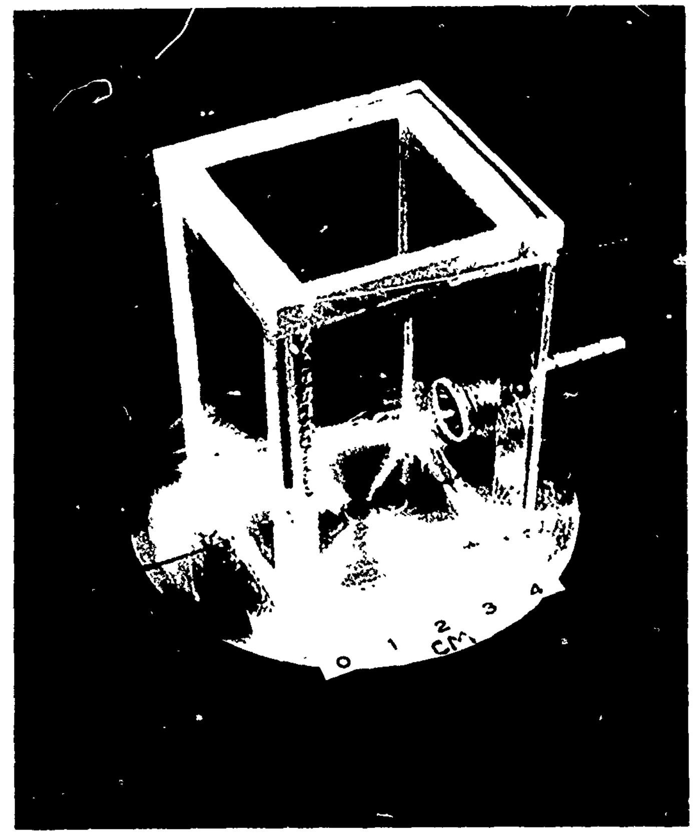

Fig. 12 Flyer Target Configuration

was required so the camera could reach the desired framing rate before the gun fired. The Fastax camera is a constant speed-drive camera (for a specific input voltage), thus its framing rate is continuously changing as the amount of film on the take-up reel increases. The framing rate of the camera was obtained by placing timing marks on the film during event photographing. The timing marks were produced by a neon glow lamp mounted under the drive sprocket in the camera housing. The glow lamp is energized by a 1,000 cps signal generated by a Wollensak Model WF 311 Fastax Pulse Generator. This provides 1,000 light flashes per second. The light emitted from the glow lamp is focused on the edge of the film producing 2.5 mm wide timing marks along one edge of the developed film (Fig. 13) outside of the picture area (Ref 17:1-5).

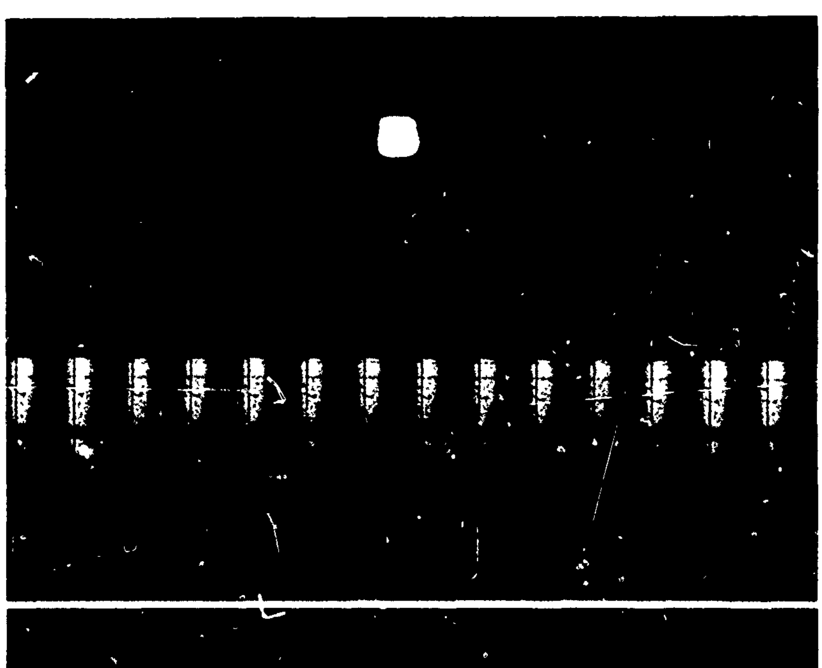

Fig. 13. Fastax Timing Mark

A computer program available at AFML was used in the reduction of flyer data (Ref 28). The program input requires the x, y coordinates of a stationary reference point for each frame, and those of the moving points of interest, respective frame number, designation of a zero time frame, as well as x and y magnification factors, and camera speed. The output of this program gives velocity based on a least squares fit of position-time data to a straight line.

To provide the stationary reference required by the program, the grid shown in Fig. 14 was placed in the field of view between the camera and target as shown in Fig. 16. The grid consisted of two vertical wires and one horizontal wire. In addition, at selected intervals a wire grid (Fig. 15) was photographed with the Fastax Camera to check parallax and to verify the magnification factors determined by the normal grid.

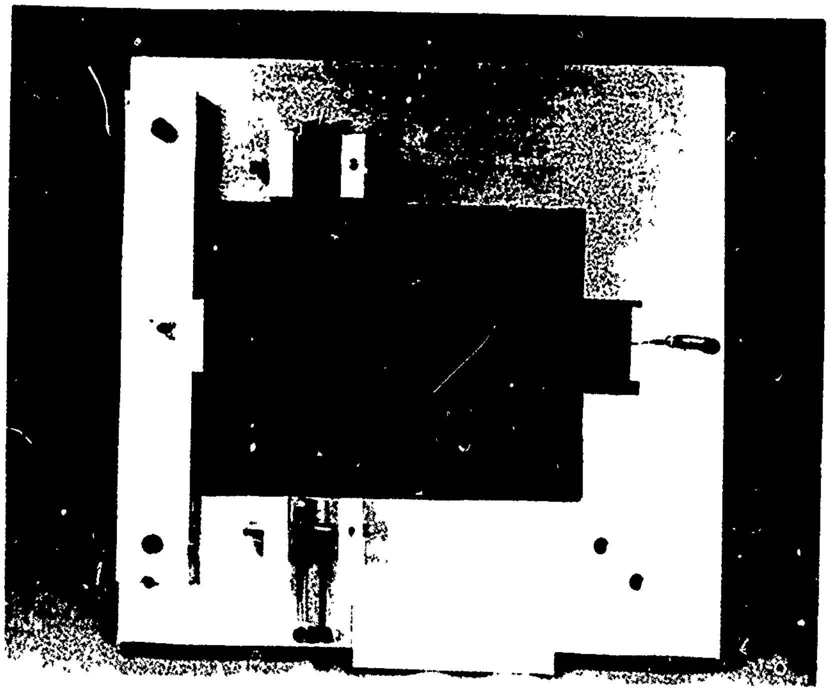

Fig. 14 Reference Grid

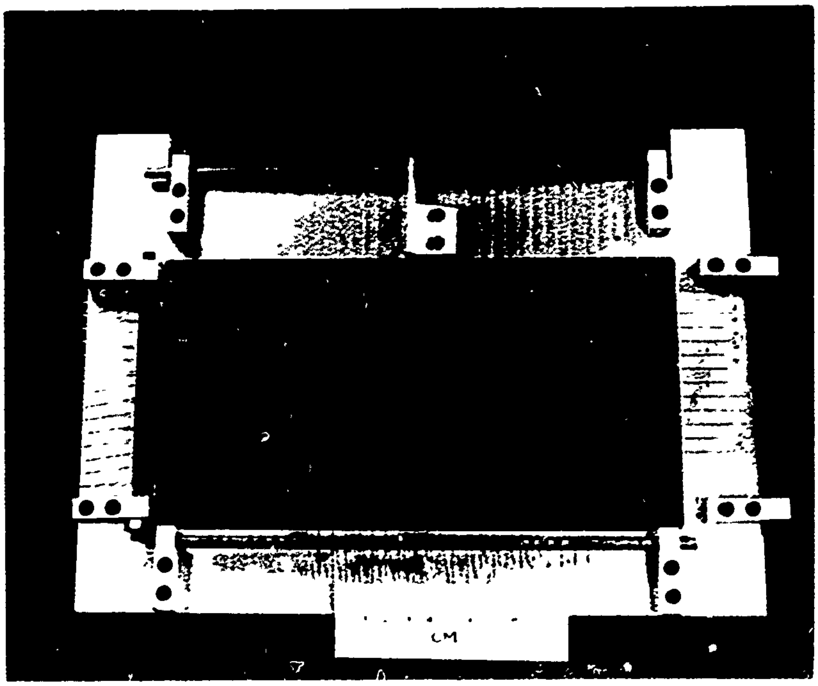

Fig. 15 Calibration Grid

Fig. 16 Reference Grid Position

Light-Gas Gun

The AFML light-gas gun was used for the higher velocity shots (greater than 2.83 km/sec) of this experimental program. Figure 17 shows the main parts of the light-gas gun and Ref 20 contains a complete description of its operation. A brief discussion of the light-gas gun is included here for completeness.

The light-gas gun uses a conventional 40 mm shell to drive a piston which in turn compresses hydrogen gas. The compressed gas then launches the projectile. The gun has the capability of launching projectiles weighing one gram at velocities of up to 9 km/sec. Viewing ports and instrumentation along trajectory facilitate measurement of various dynamic events. The target is mounted in a cubic target tank which has removable ports to permit instrumentation of the impact events (Ref 32:18-19).

Light-Gas Gun Experimental Procedures

A fifty caliber barrel was used for launching the projectile. The required velocities were obtained by varying the powder charge. The same two section sabots (Fig. 9) as used in the fragment launch range experiments were used to hold the projectile during launching.

Velocity Determination. A Wollensak Corporation 16-mm Fastax Oscillographic Camera was used to measure the velocity of the projectile. The system shown in Fig. 18 generates shadowgraph images of the projectile on the camera film. The camera is positioned to view two slits placed adjacent and perpendicular to the range axis as shown

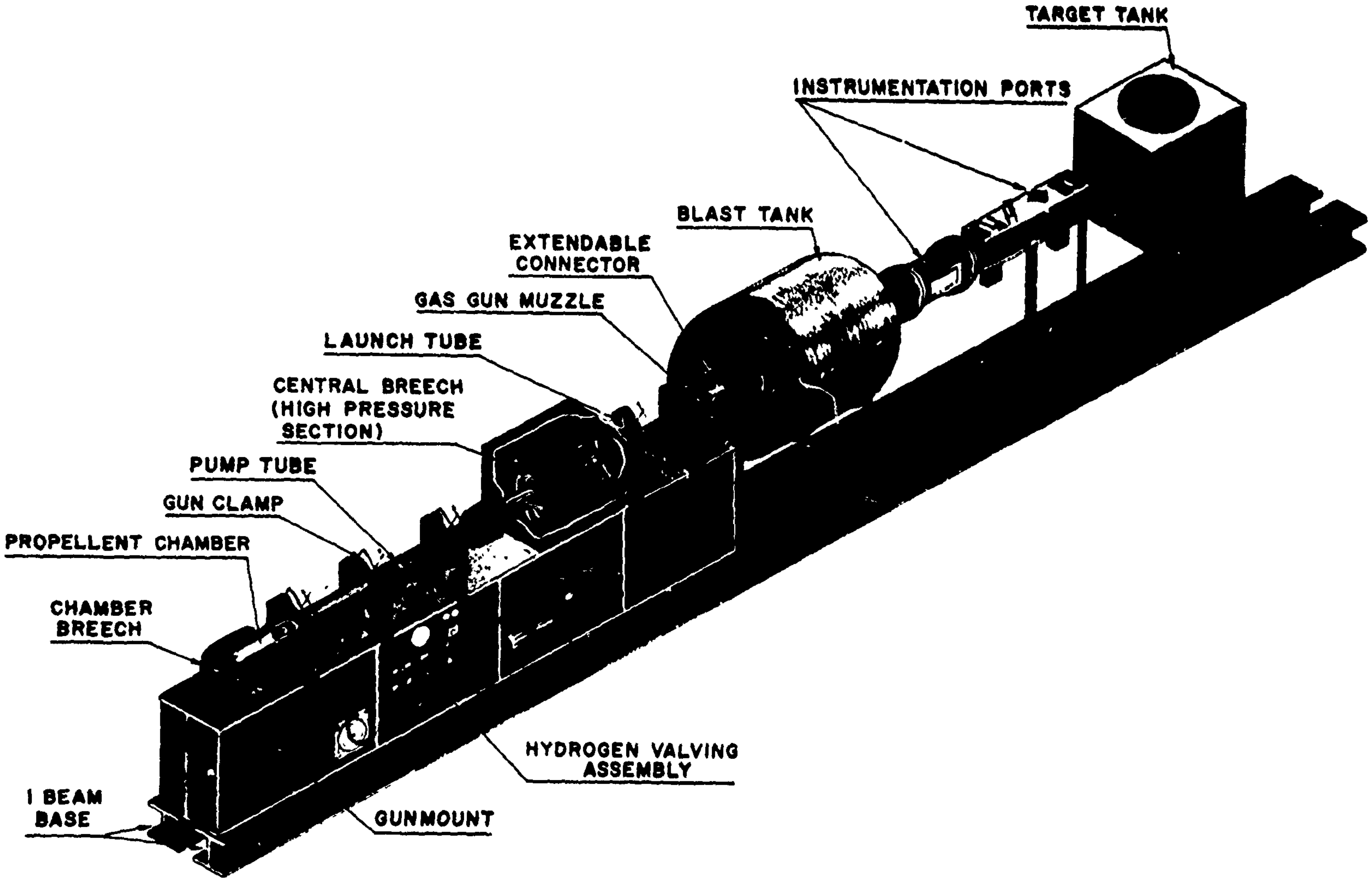

Fig. 17 Component Parts of Light Gas Gun

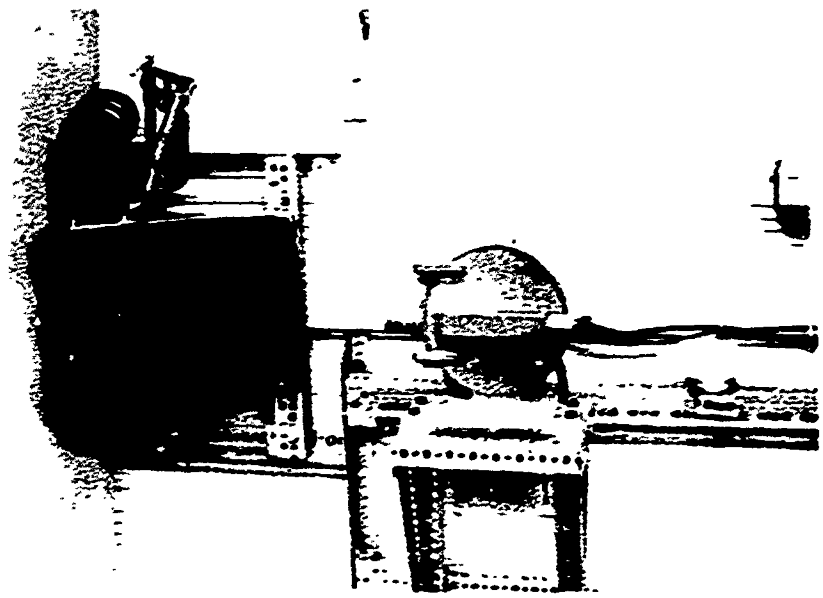

Fig. 18 Fastax Oscillographic Camera Setup

in Fig. 19. The mirror systems are used to align the images from the slits end-to-end on the film. The time between generation of the two images is the time required for the projectile to traverse the distance between the two slits. The projectile velocity is thus determined by knowing the distances between the slits and the elapsed time of travel between them (Ref 29:14-15).

Shock Pressure Measurement. The same basic procedures were used to measure flyer velocity as discussed in the fragment launch range section. The only deviation being that a Beckman and Whitley Model 326-3 Dynafax Camera was used to photograph the flyers.

Measurement Techniques

Flyer Velocity. The film records of the flyers produced in both phases of the experiment were translated into numerical data suitable

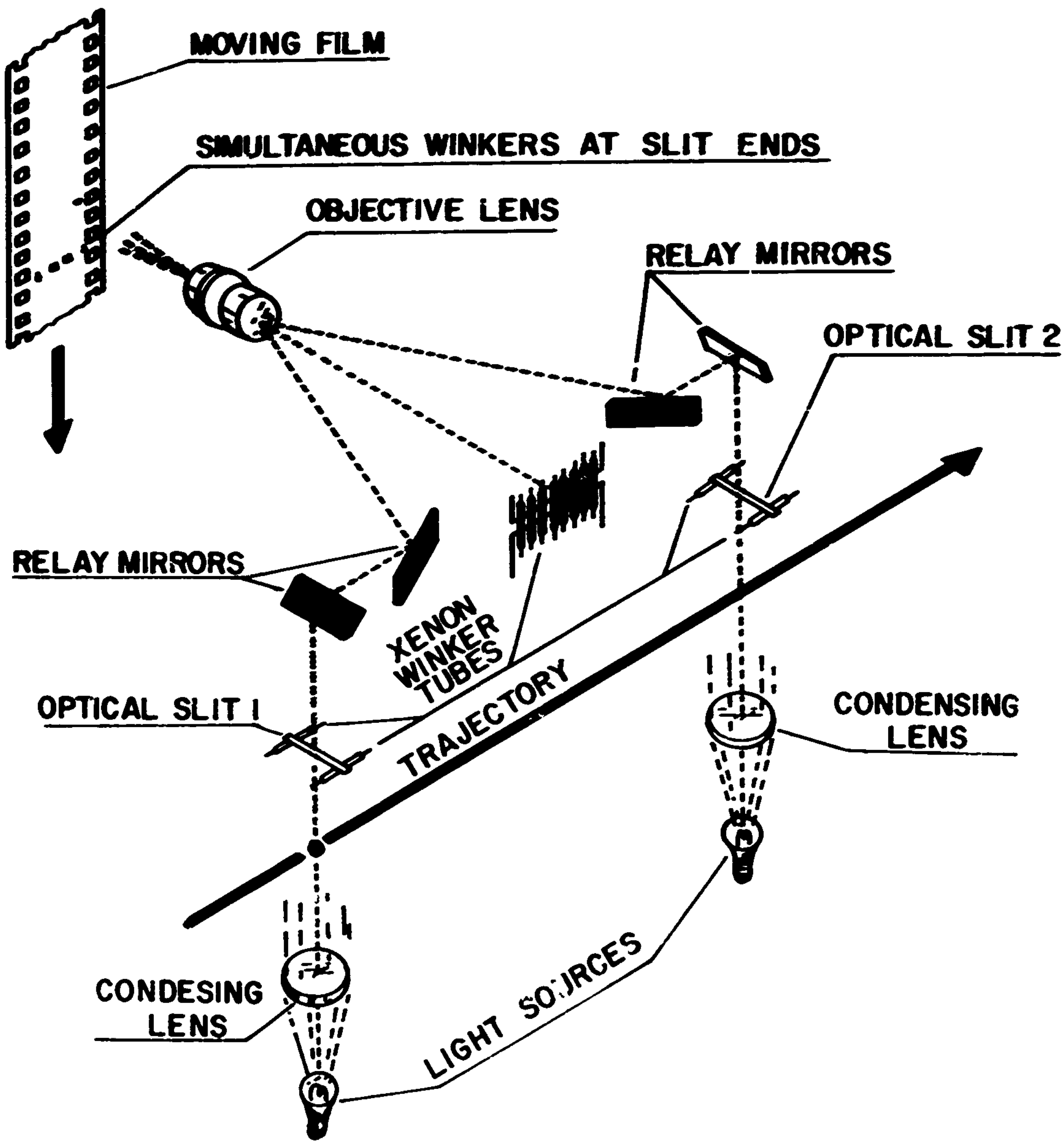

Fig. 19 Diagram of Streak Camera System

for input into the computer program mentioned previously with an automatic digital film reader (Fig. 20). A complete description of this system is contained in Ref 30. The film to be read is positioned on a microscope stage located in the object plane of the projection microscope. Micrometer drums drive the stage in two perpendicular directions. The image is projected on a screen which contains a pair of crossed reference lines. The film being read is positioned such that the reference line in each frame is aligned with the fixed reference on the screen. This reference position is then automatically punched on an IBM card by activating a switch. Next the flyer is positioned under the reference point on the screen and its coordinates are punched

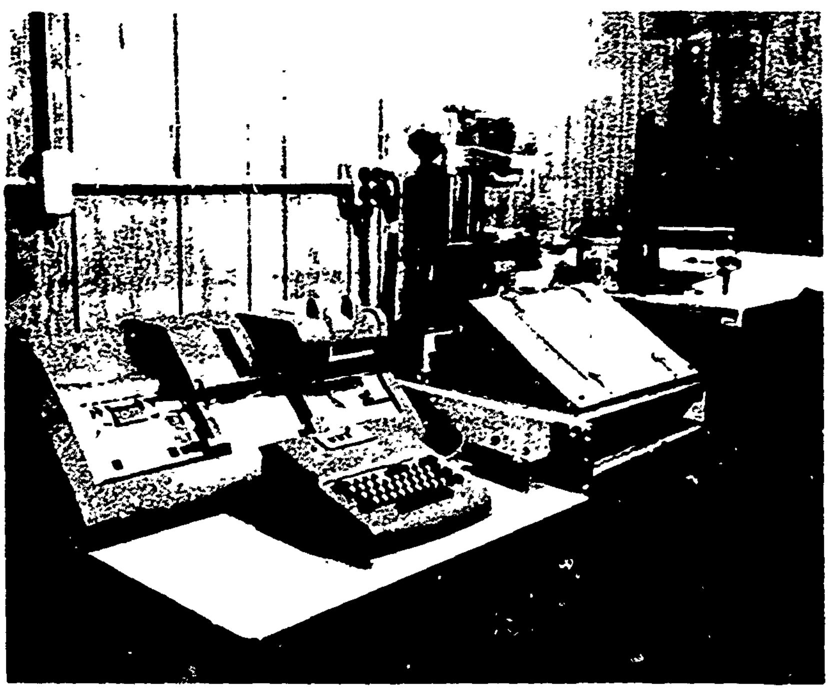

Fig. 20 Automatic Film Reader

on another IBM card by activating the switch again. This procedure is repeated for each flyer in the frame and for the successive frames of film containing information (Ref 26:50-51).

Crater Measurement. Crater depth and diameter measurements were obtained using a depth gage and microscope in conjunction with a machinists calibrated travel table (Fig. 21). The quantities to be measured are shown in Fig. 22. The procedure was to focus the microscope on an undeformed portion of the target surface. The target was traversed under the microscope until a ring of the crater wall came into focus and the cross hairs were aligned on it. The scale on the drive shaft of the calibrated travel table was zeroed at this point and the table was traversed across the crater until the opposite side of the crater ring came into focus. The cross hairs were then aligned on this side of the ring. The distance traveled is the crater diameter. For depth measurements, the microscope was focused on an undeformed portion of the target surface and the depth gage was set to zero. The table was then traversed to the approximate center of the crater and the microscope lowered till the bottom of the crater came into focus. The location of the crater bottom was achieved by repositioning the target and checking the focus of the crater bottom. Once having determined that the microscope is focused on the crater bottom, a reading of the crater depth is obtained from the depth gage. To eliminate reading errors, the crater diameters were measured at least four times for each target and the depth twice by different operators. The values listed in Table II are the results of averaging these readings.

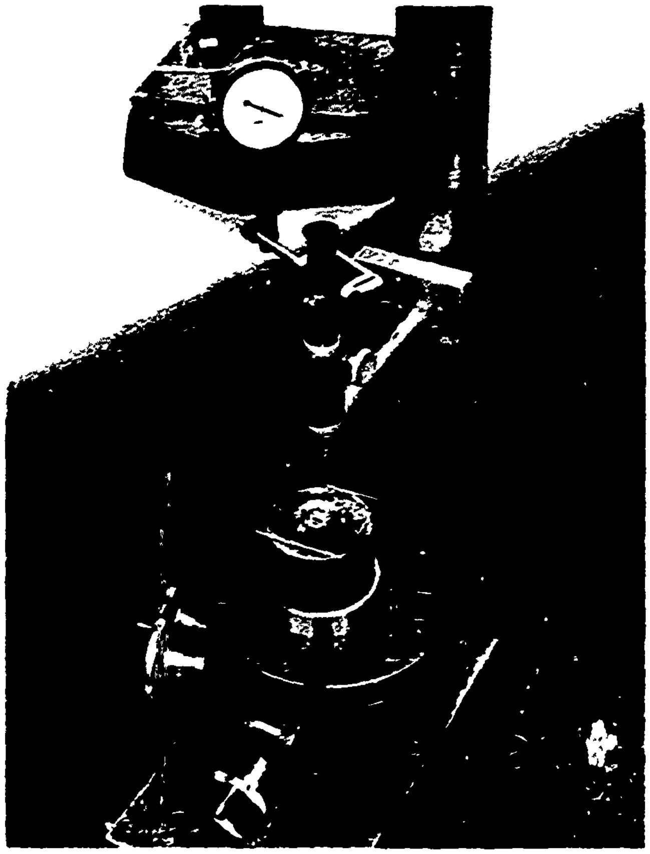

Fig. 21 Crater Measurement Setup

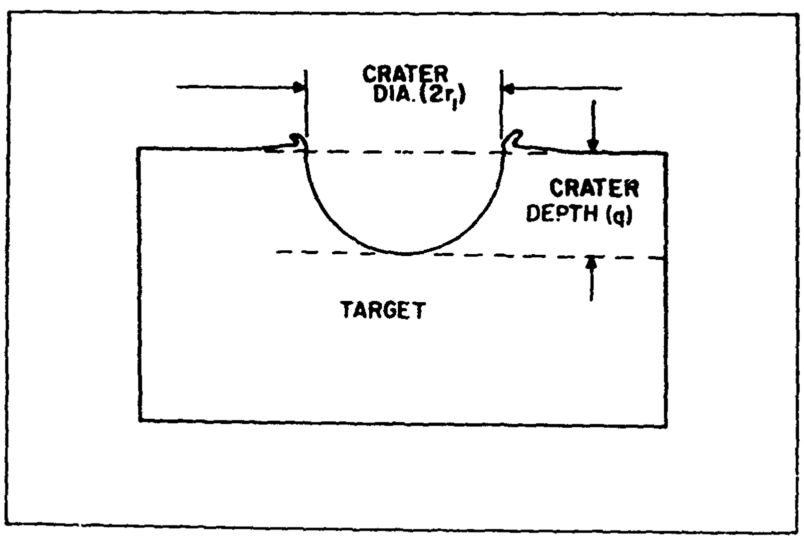

Fig. 22 Crater Measurement Technique

Projectiles and Targets

All targets were cut from 6061-H aluminum ingots. A Brinell hardness test of the material was conducted with results shown in Fig. 37. In addition, samples of the target material were subjected to a dynamic compression test using a Hopkinson Split Pressure Bar apparatus. Appendix B contains a description of the bar and procedures followed in the testing. The material constants shown in Table I for 6061-H are the results of these tests.

The projectiles were made from four different aluminum alloys: 1100-T0; 6061-T6; 2017-T4; and 7075-T6. The material constants for these materials are presented in Table I with appropriate references. The 2017-T4 projectiles were obtained commerically from Hartford Universal Company. The other projectiles were manufactured by the University of Dayton from bar stock of the specific alloy. The weight of each projectile fired was recorded and is presented in the Summary of Experimental Results, Table II.

The effect, if any, of the manufacturing process for the projectiles was also considered. Projectiles of each alloy were annealed to its designated temper in accordance with the requirements specified in Ref 21. These annealed projectiles were then fired at targets and the resulting craters compared with craters produced by work-hardened projectiles fired at or near the same velocity to determine the effect of cold working of the projectiles, if any. The results are presented and discussed in Appendix B.

IV. Experimental Results and Data Analysis

Cratering Results

For the purpose of graphically displaying the greatest contrast in the craters produced, photographs of selected craters over the impact spectrum of this experimental program for the 1100-T0 and 7075-T6 alloys are presented.

Figure 23 is a photograph of the selected 1100-T0 alloy projectile shots. It should be noted that each target is identified with shot number and impact velocity. The targets are arranged in order of impact velocity, with the lowest velocity target being the uppermost in the photograph. The lower velocity shots shown (velocity less than 1 km/sec) provided no cratering data due to the projectiles remaining in the craters. Any measurements would have necessitated costly cutting and machining. Consequently, these particular shots are not listed in any other part of this report.

Typical craters produced by the 7075-T6 alloy projectile are shown in Fig. 24; the comments made for the 1100-T0 alloy shots photograph are equally applicable to this photograph.

In Fig. 25 a very interesting and noteworthy result was observed. As shown in the figure, a hemispherical shell of the projectile material was lifted out of the crater. The hemispherical shape of this shell lends some credence to the assumption of the mode of projectile deformation

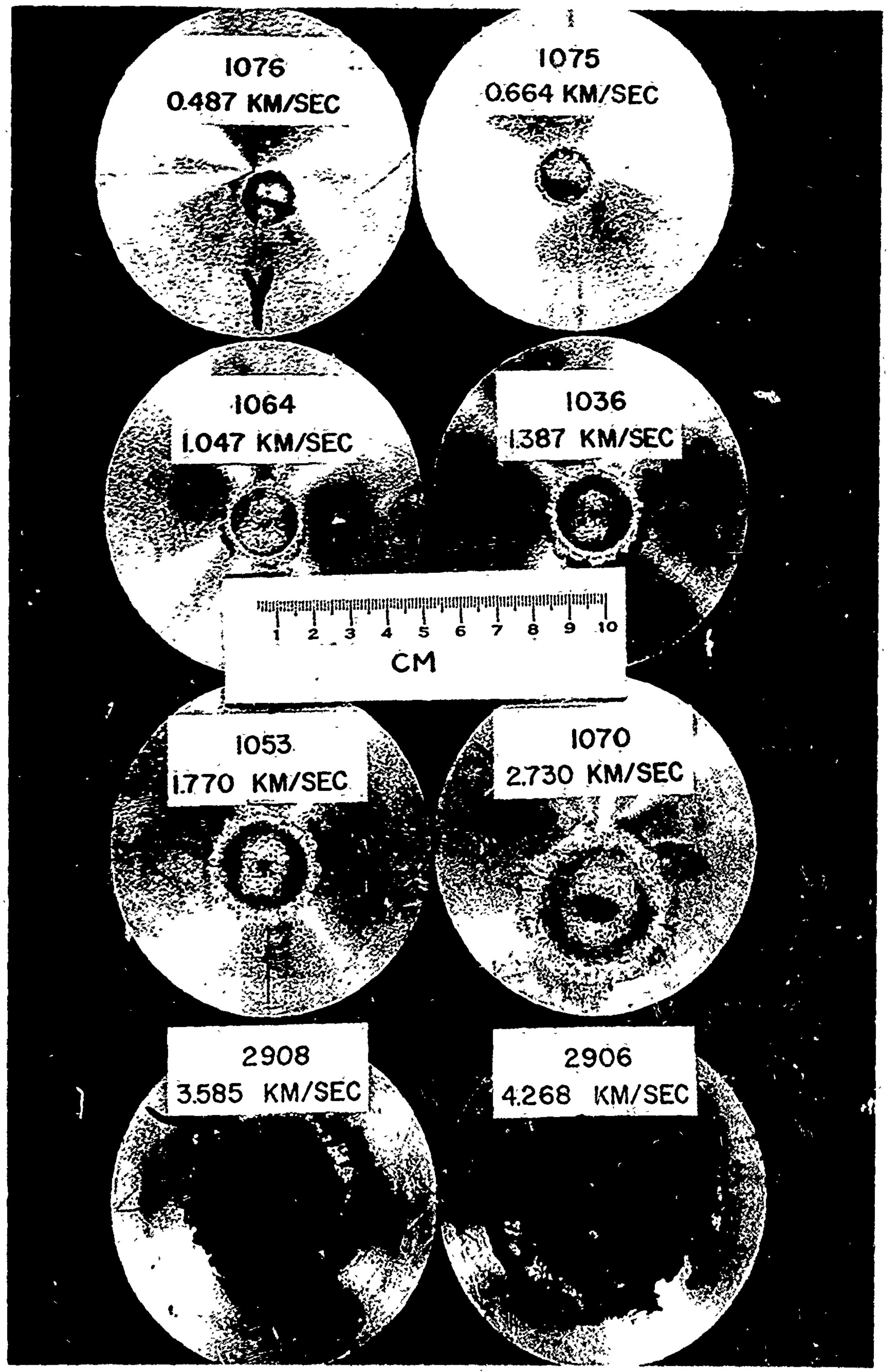

Fig. 23 Typical 1100-T0 Craters

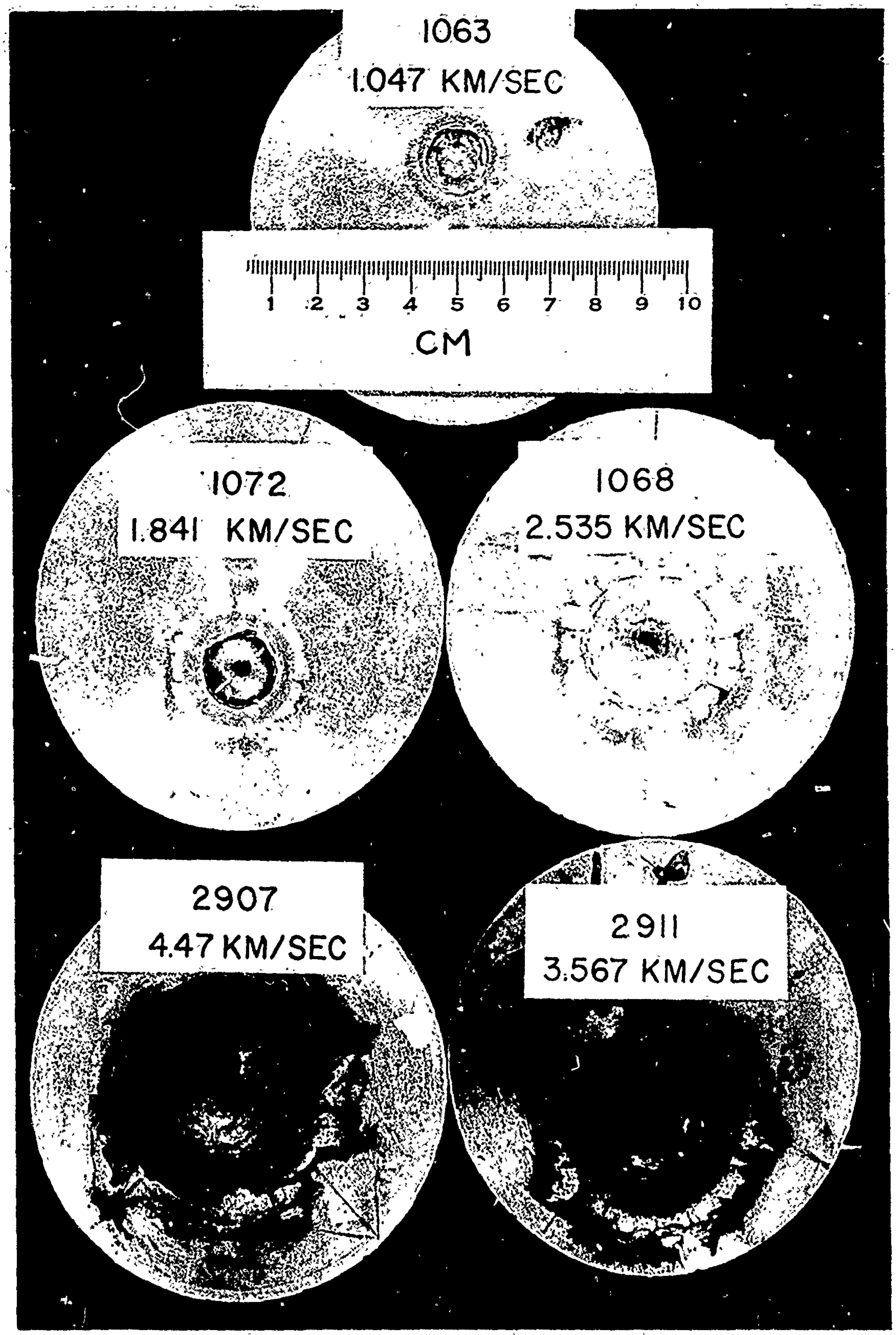

Fig. 24 Typical 7075-T6 Craters

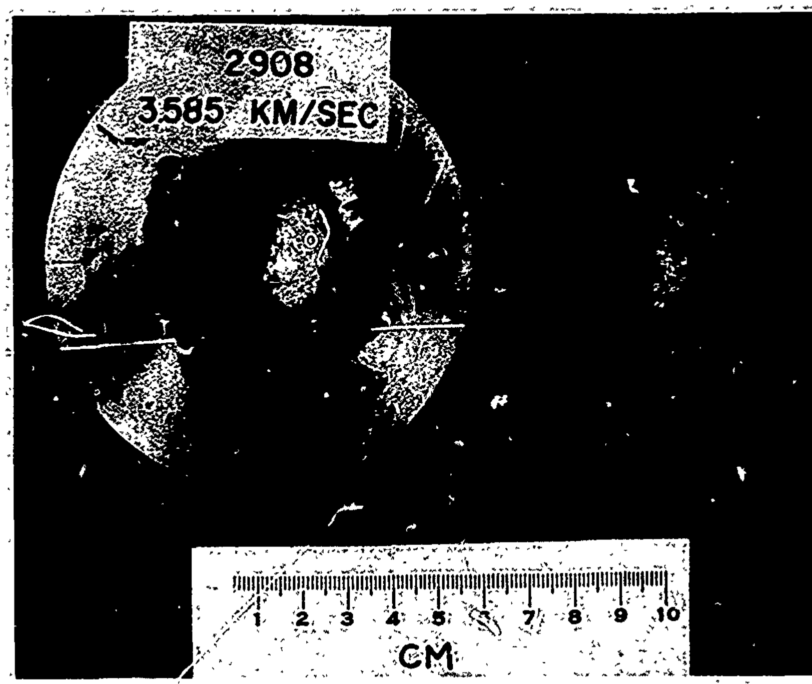

Fig. 25 Crater and Hemispherical Shell of Projectile Material

used in the Coupled Cratering Model development. This result, which was not reproduced as completely in any of the other experimental shots, is an excellent example of the large deformation undergone by the projectile during high velocity impact.

Diameter and Depth of Craters. A summary of the experimental cratering results are presented in Table II (Appendix D). The values of velocity V2 listed in Table II for shots fired on the Fragment Launch Range have been corrected for drag effects as described in Appendix A. The accuracy of velocity determination was ± 0.33% and ± 0.25 for the Fragment Launch Range and light-gas gun respectively. The craters formed were not exactly symmetrical; consequently, the results for crater diameter listed represent an average diameter. The crater diameter measurements were made to within ± 0.025 cm with an accompanying measurement error of ±2%. Crater depths were measured to within ±0.01 cm with an accompanying error of ± 3.6%.

Graphs of final crater depth and diameter vs impact velocity for the projectiles used in this study are presented in Appendix D. The curves presented on the graphs are first order polynomial least squares fits to the data. The standard deviation (σ) is shown as broken lines on the graphs. The shots using the specially annealed projectiles are shown as triangles, while all other data points are represented as octagons. The effect of manufacture is verified as negligible by the position of the annealed data points on the figures. This point is discussed more fully in Appendix B.

To portray graphically the effect of projectile strength on final crater dimensions and to prevent over cluttering the graph with data points, it was decided to present graphically the two materials representing the widest span in projectile strength (1100-T0 and 7075-T6). The results are shown in Fig. 26 and Fig. 27.

Figure 26 shows that the projectile strength has little effect on crater diameter over the velocity spectrum of this experimental program. However, the contrary is shown in the depth vs impact velocity data (Fig. 27). This graph shows that the crater depths for the two projectile materials differ significantly at lower velocities but are effectively the same for impact velocities of 3.5 km/sec or greater.

Shock Pressure Results

The results of the peak shock pressure experiments are

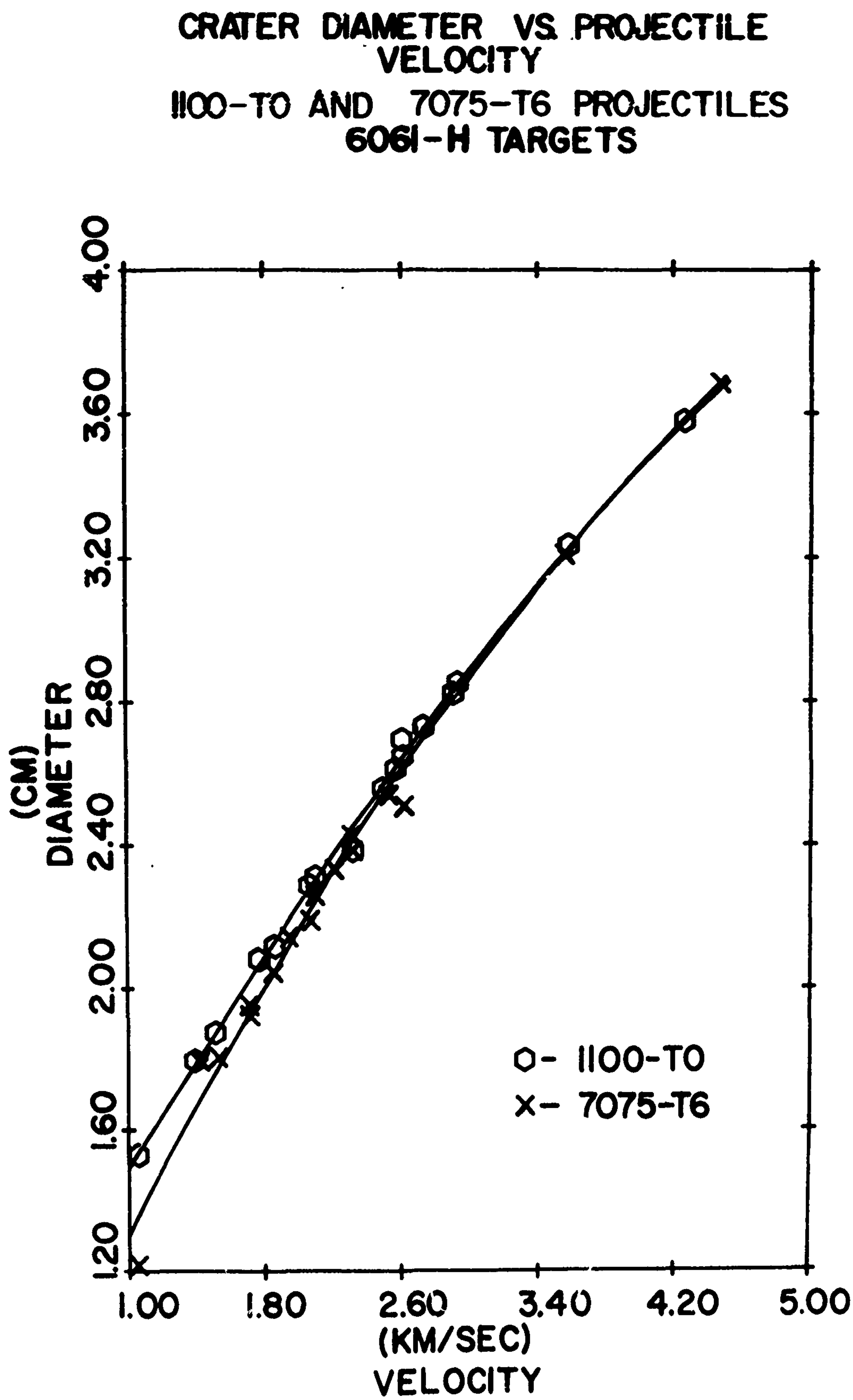

Fig. 26 Crater Diameter vs Projectile Velocity for 1100-T0 and 7075-T6 Projectile Shots

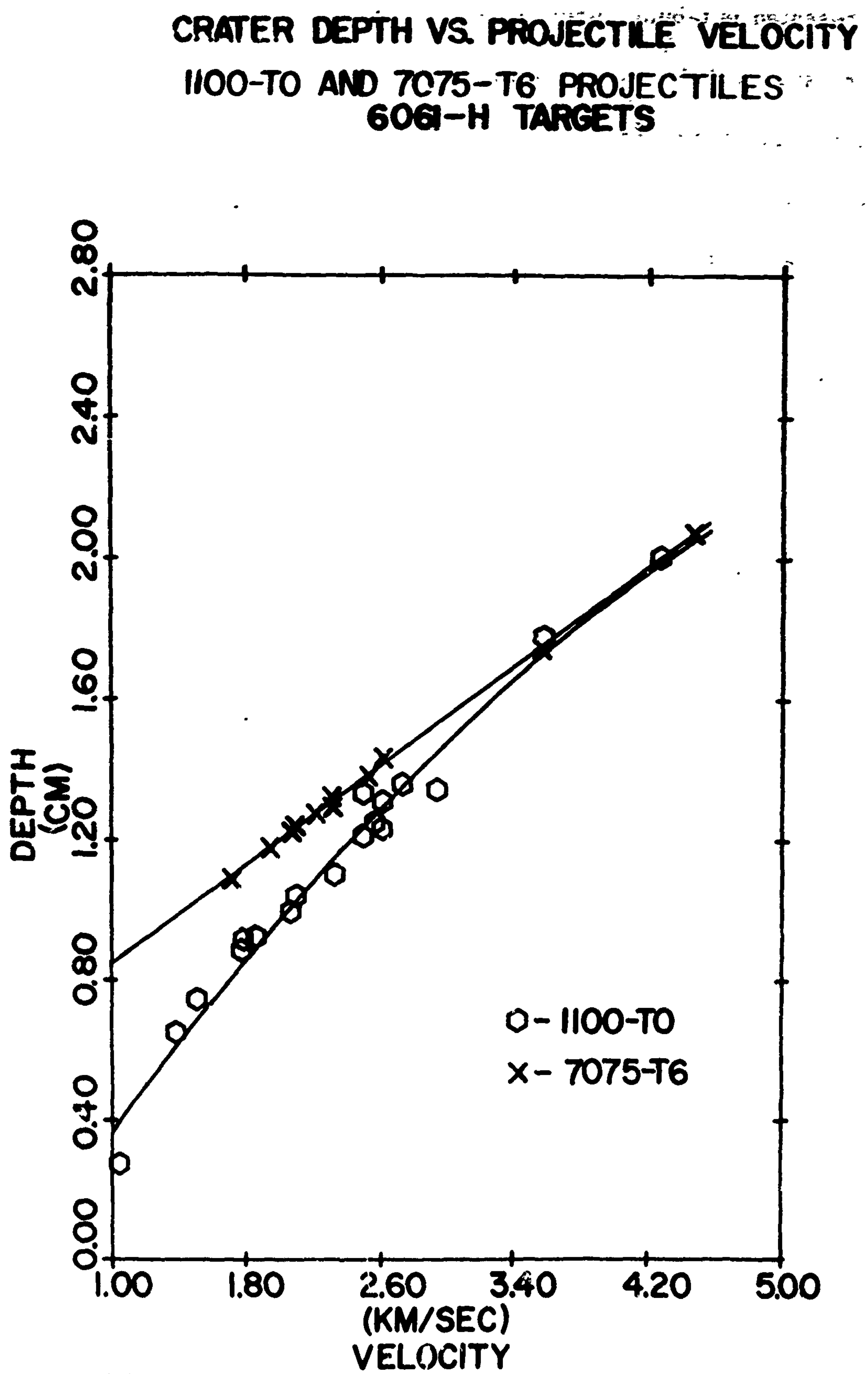

Fig. 27 Crater Depth vs Projectile Velocity for 1100-T0 and 7075-T6 Projectile Shots

presented in tabular form in Table IV (Appendix E). The values for pressure and flyer velocity shown were computed using the corrections and relationships presented in Appendix C. Graphs of shock pressure vs impact velocity for the specific projectile materials treated in this study are presented in Fig. 28.

Analysis of the shock pressure or flyer velocity data shows an unexpected high degree of scatter. This scatter prevents any meaningful conclusions being drawn from this portion of the experimental program. However, disregarding the data from the three highest velocity shots and extending the linear fits of the remaining data shows that these fits converge at approximately 3.5 km/sec for the 1100-T0 and 7075-T6 alloy shots. This observation is very interesting when considered in light of the final crater dimension result; however, there is no justification for disregarding the higher velocity shots. The experimental procedures and data reduction techniques were reviewed and no definite conclusions could be drawn as to the cause for the scatter. Other experimental programs using basically the same technique, but in a higher velocity impact region, did not experience this type of scatter (Ref 10 and 27).

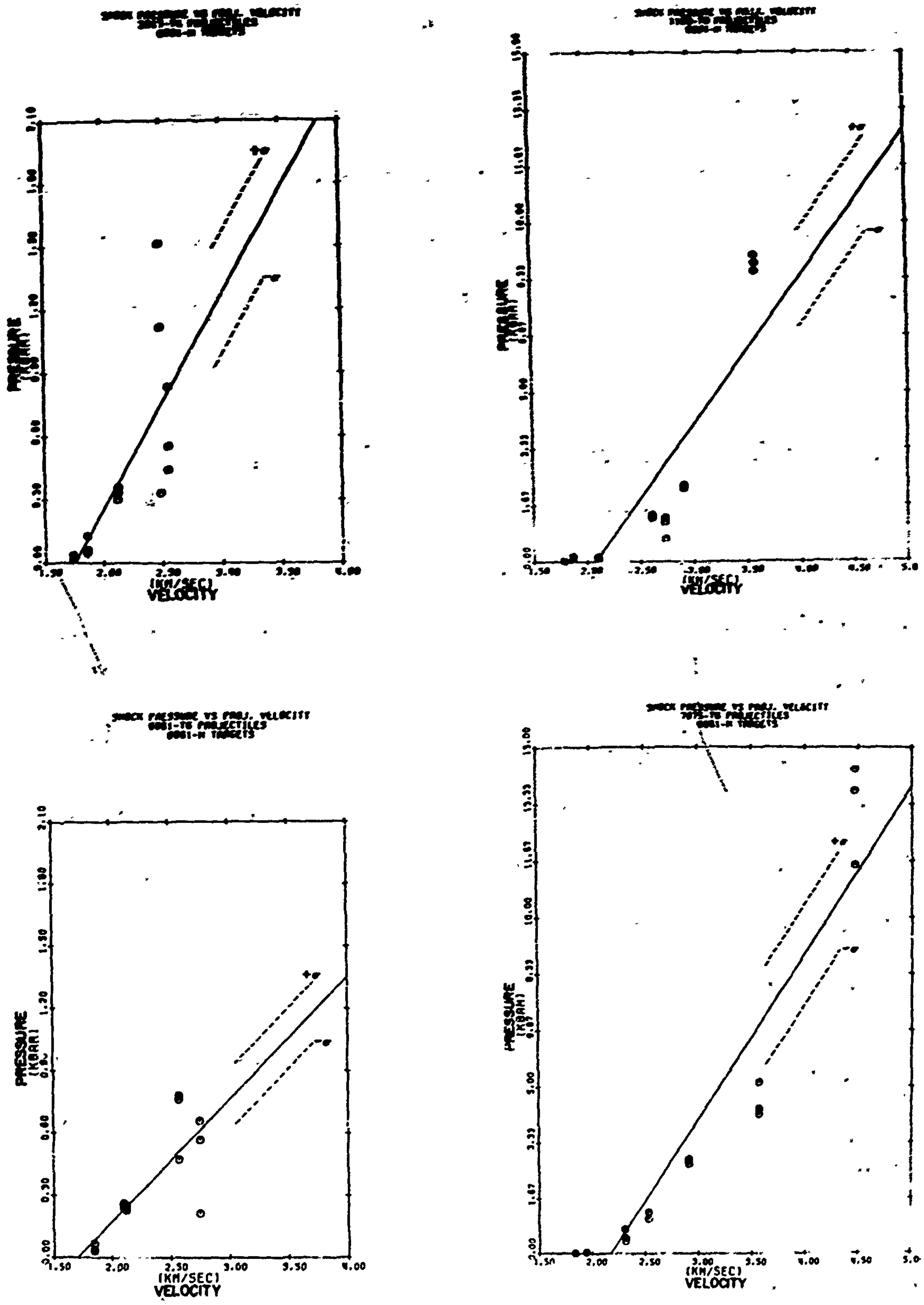

Fig. 28 Graphs of Shock Pressure vs. Impact Velocity

V. Coupled Model Predictions and Comparisons with Experimental Results

The Coupled Model's predictions were compared with the experimental results of this study and with some experimental results obtained at the Air Force Materials Laboratory Hypervelocity Facility. The results of these comparisons are treated separately in the following sections.

Comparison with Experimental Results of this Study

The solid lines shown on the graphs in Fig. 29 represent the output of a computer program of the Coupled Model developed in Section II. The experimental data points are shown on the graph as octagons.

Diameter Comparisons. From Fig. 29, it is seen that the model provides an excellent prediction of crater diameter for all of the projectile materials treated in this study. The 1100-T0 projectile graph shows that the model prediction is so close that it could be misconstrued to be a curve fit of the data. For the other projectile materials of this study, the model predictions are not as spectacular; however the general slope and shape of the curves appears to be qualitatively the same as the experimental data.

The variations between the predictions of the model and the experimental results range from essentially zero, in the case of 1100-T0, to within 0.16 cm or 8% for the 7075-T6 projectiles. It will

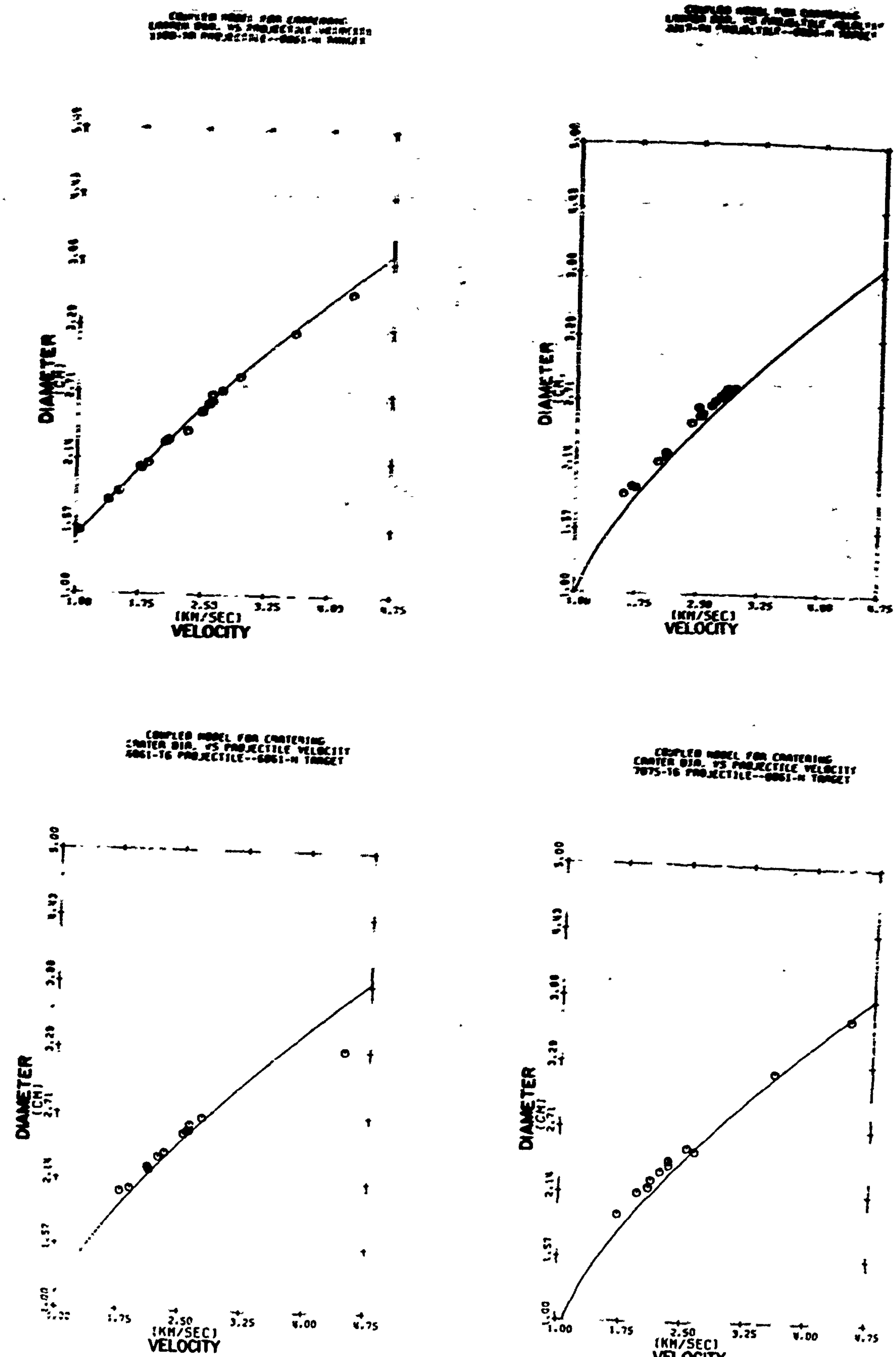

Fig. 29a Coupled Model Predictions

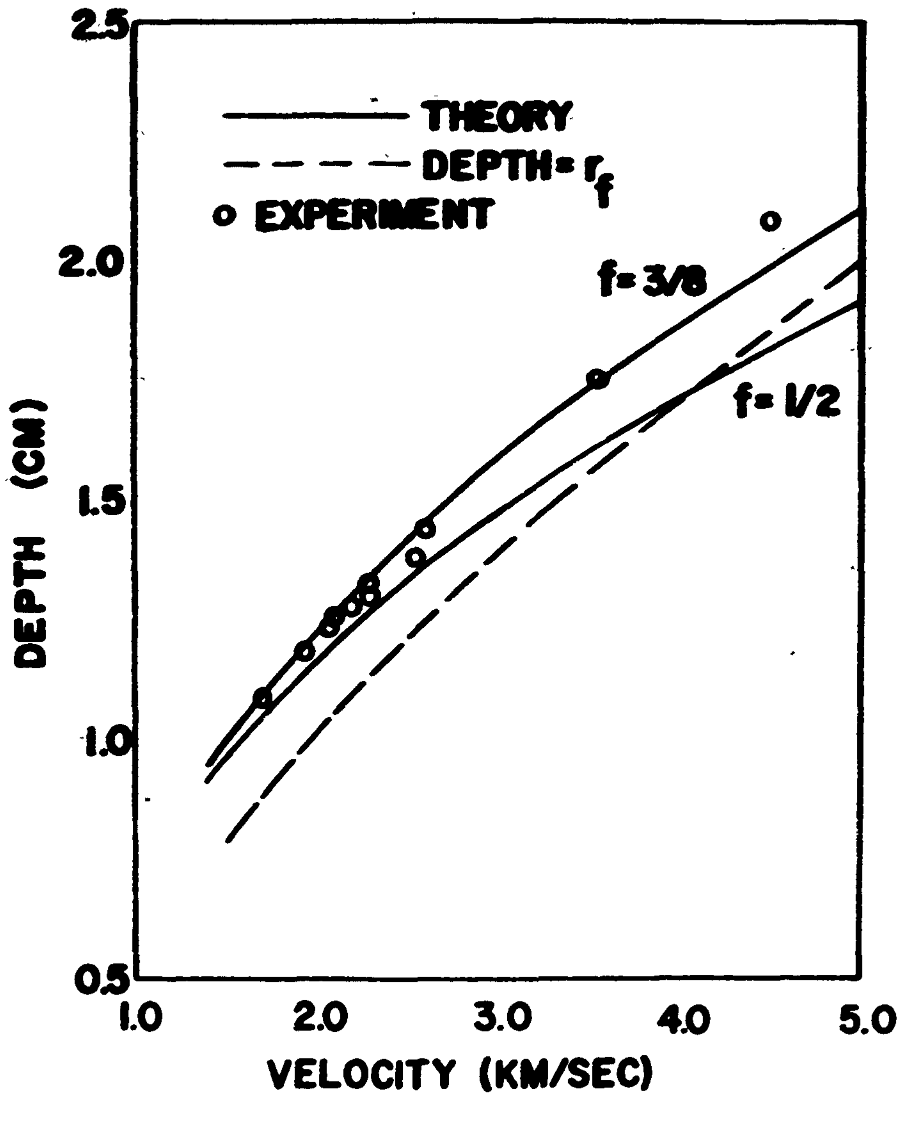

Fig. 29 b Coupled Model Predictions for the Impact of 7075-T6 projectiles onto 6061-H Aluminum Targets

also be noted that the variation between theory and experiment increases with projectile strength.

Crater Depth. The procedure for predicting crater depth as developed in Section II was not considered appropriate for the impact of 1100-TO projectiles onto 6061-H targets, since the yield strength of 1100-TO is less than half that of 6061-H. In such a case, the rigid penetrator theory employed in Phase I is not appropriate. Moreover, it is not appropriate to compare the penetration for projectiles of different yield strengths, for it was assumed in the development of the model that the complete destruction of the projectile, requiring an energy $Y_p D^3$, would take place during the cavity expansion phase. The details of the rate at which the projectile is consumed do not affect the predictions of the final crater diameter, as long as the destruction is complete, but would affect the prediction of the depth. It is assumed that the rate of destruction of the projectiles would be influenced significantly by the properties of the projectiles. For these reasons, only a comparison between theory and experiment for the strongest projectiles (7075-T6) is given here. Experimental data for 7075-T6 are repeated on Fig. 29b, and the solid lines are the predictions of the coupled model for the two assumed cases of assumed shell thickness. The lower curve corresponds to f = 1/2 (zero shell thickness), and the upper curve corresponds to f = 3/8, i.e. a shell thickness equal to the radius of the hemisphere. The dashed line represents the depth which would result if the crater were assumed to be hemispherical so that the depth would equal the predicted final crater radius. It can be seen from the figure that the theory predicts the crater depths remarkably well in the range of 1.5 to 2.5 km/sec. A value of f midway between the two limiting values would, in fact, give remarkable agreement. It is particularly significant that the theory gives a much better prediction of depth than the assumption of a hemispherical crater (depth = radius), which would lead to the dashed line. At higher velocities (above 3 km/sec), the agreement between the theory and the limited data obtained in these experiments suggests that the theory is not as successful. Calculations were performed for 6061-T6 and 2017-T4 projectiles; the results were virtually indistinguishable from the results for 7075-T6 for impact velocities above 1.5 km/sec.

Comparison with Hypervelocity Data

To test the applicability of the model in the hypervelocity range, the model predictions were compared with the results of some experiments conducted at the AFML Hypervelocity Facility. The specific experimental results are shown in Table V (Appendix F). It will be noted that the data is for two different target materials (1100-T0 and 6061-T6) and for spherical projectiles of two different diameters (3.18 mm and 6.35 mm). The results of these comparisons are shown in Fig. 30, with the model predictions again shown as continuous curves.

For the 6061-T6 target material shots, it is seen from Fig. 30a that the model provides a good prediction for crater diameter. The

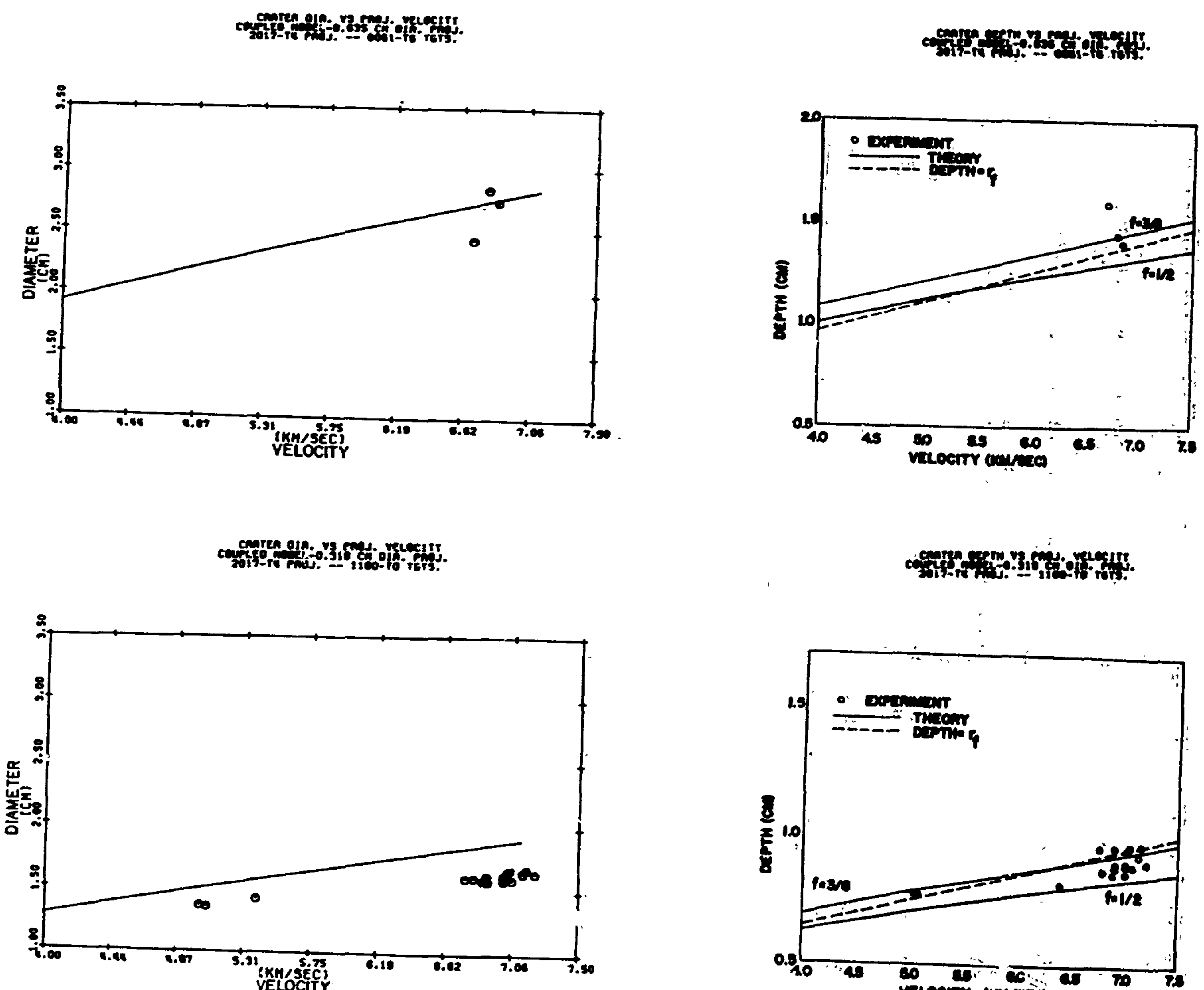

Fig. 30 Coupled Model Predictions (AFML Hypervelocity Data)

comparison with 1100-T0 target data (Fig. 30b) shows that the model predicts crater diameter to within 0.2 cm or 13%.

The predictions of depth are compared with experimental results in Figures 30c and 30d. The predicted crater radii are also shown as the dashed curves. At these velocities, the coupled model (using an intermediate value of f) leads to predictions of depth which differ but little from the crater radii. Either provides an estimation of depth which is within 15% of the data for 6061-T6 targets and considerably better in the case of 1100-T0 targets.

VI. Conclusions and Recommendations

Conclusions

The projectile strength does have an effect on final crater dimensions in the lower and middle part of the transition velocity range (Fig. 1) for the projectile and target materials considered in this study. Those materials were: for the projectiles--1100-T0, 2017-T4, 6061-T6, and 7075-T6; for the targets 6061-H. At 3.5 km/sec projectile strength effects are seen to disappear as evidenced by the craters becoming virtually indistinguishable for the different projectile alloys used in this study.

The shock pressure experiments provided no meaningful information due to the scatter in the data. This scatter indicates either something is wrong with the experimental procedures or that the physics associated with shock propagation in the velocity region of this experimental program is different from that found by Prater (Ref 27) and others in the hypervelocity region.

The Coupled Model provided excellent predictions of crater diameter for all of the projectile materials (1100-T0, 2017-T4, 6061-T6, and 7075-T6) of the experimental portion of this study. The variation between the predictions of the model and the experimental results range from essentially zero in the case of 1100-T0 and to within 0.16 cm or 8% for the 7075-T6 projectiles. The predictions of the model for crater depth showed good agreement with experimental results. The model is not applicable to impacts where the ratio of projectile strength to target strength is not great enough so that the projectile can be considered as a rigid penetrator in Phase I of the Coupled Model Theory. Comparison of the model with AFML hypervelocity data showed that the model again provides a good prediction for crater dimensions. The general shape and slope of the model predictions were qualitatively similar to the experimental results.

The results of the model comparisons indicate that using dynamic principles for modeling provides predictions which are remarkably good considering the simplifying assumptions and approximations used in the model development. The closeness and the qualitative similarity between predictions and experimental results indicate that the model holds great promise in providing a theoretical approach to the long standing problem of modeling the cratering phenomenon.

Recommendations

a. Additional experiments should be conducted with different projectile-target combinations to reaffirm that final crater dimension differences disappear with velocity.

b. The shock pressure experiments should be repeated using the same procedure as used in this study. However, careful consideration should be given to the validity of the method. Consequently, other experimental procedures should be devised to substantiate these results.

c. The Coupled Model should be compared with other cratering experimental data over a large range of projectile-target combinations and velocities.

Bibliography

1. Bertke, R. S. The Air Force Materials Laboratory Terminal Ballistic Research Facility. AFML-TR-69-215. Wright-Patterson Air Force Base, Ohio: AFML, October 1969.

2. Bois, G. P. Tables of Indefinite Integrals. New York: Dover Publication, Inc., 1961.

3. Bridgman, P. W. The Physics of High Pressure. London: G. Bell and Sons, Ltd., 1949.

4. Bridgman, P. W. Studies in Large Plastic Flow and Fracture. New York: McGraw-Hill Book Co., 1952.

5. Carson, J. M. and J. M. Hawn. Some Properties of Iron, Copper, and Selected Aluminum Alloys Including True Stress-True Strain at Reduced Temperatures. AFML-TR-68-215. Wright-Patterson Air Force Base, Ohio: AFML, September 1968.

6. Charters, A. C. "High-Speed Impact", Scientific American, 203:4, 128-140, October 1960.

7. Engel, O. G. Collisions of Liquid Drops with Liquids. WADD-TR-60-475, Part III. Wright-Patterson Air Force Base, Ohio: AFML, June 1966.

8. Fields, T. E. The Effect of Projectile Shape on the Ballistic Perforation of Thin Metal Plates. AFML-TR-69-202, prepared from M. S. thesis performed for the Air Force Institute of Technology. Wright-Patterson AFB, Ohio: AF Materials Laboratory, 1969.

9. Fung, Y. C. Foundations of Solids Mechanics. Englewood Cliffs, New Jersey: Prentice-Hall, Inc., 1965.

10. Gehring, J. W., W. L. Meyers, and J. A. Charest. "Experimental Studies of Impact Phenomena and Correlation with Theoretical Model", Proceedings, Seventh Hypervelocity Impact Symposium, Vol. V. Tampa, Florida: Martin Company, 1965.

11. Goodier, J. N. "On the Mechanics of Indentation and Cratering in Solid Targets of Strain-Hardening Metal by Impact of Hard and Soft Spheres", Proceedings, Seventh Hypervelocity Impact Symposium, Vol. III. Tampa, Florida: The Martin Company, 1965.

12. Halperson, S. M. "Comparisons Between Hydrodynamic Theory and Impact Experiments", Proceedings, Seventh Hypervelocity Impact Symposium. Vol. V. Tampa, Florida: Martin Company, 1965.

13. Hoerner, S. F. Fluid-Dynamic Drag. Midland Park, New Jersey: S. F. Hoerner, 1965.

14. Holt, D. L., S. G. Babcock, S. J. Green, and C. J. Maiden. "The Strain-Rate Dependence of the Flow Stress in Some Aluminum Alloys". Transactions, American Society of Metals, Vol. 60. 1967.

15. Hopkins, H. G. "Dynamic Expansion of Spherical Cavities in Metals", Progress in Solid Mechanics, Vol. I., R. Hill and I. N. Sneddon, Eds., Pregamon Press, 84-164, 1960.

16. Hu, L. W. and H. E. Shull. "Tensile Plastic Stress-Strain Relations of 2017-T4 Aluminum Alloys Under Hydrostatic Pressure". Journal of Applied Mechanics, Transactions of the ASME: 551-553, September 1964.

17. Instruction Book. Fastax Cameras. Rochester, New York: Wollensak Optical Company, 1954.

18. Instruction Book. Fastax Goose Control Unit. Rochester, New York.

19. KornHauser, M. Structural Effects of Impacts. Baltimore, Maryland: Spartan Books, Inc., 1964.

20. Lindholm, U. S. and R. L. Bessey. A Survey of Rate Dependent Strength Properties of Metals. AFML-TR-69-119. Wright-Patterson Air Force Base, Ohio: AFML, April 1969.

21. Metals Handbook. Vol. I. (Eighth Edition), ASM, 1961.

22. Morgan, D. T., et al. Measurement of Gruneisen Parameter and the Internal Energy Dependence of Solid Equation of State for Aluminum and Teflon. AVCO RAD TR 65-24, AD624320.

23. Operating Manual. Model 326-3 Dynafax Camera. San Carlos, California: Beckman and Whitley Inc., August 1965.

24. Operating Manual. Model 319-B Oscilloscope Camera. San Carlos, California: Beckman and Whitley, Inc., August 1965.

25. Operating Manual. A Split Pressure Bar System for Dynamic Materials Testing in Tension and Compression. San Antonio, Texas: Southwest Research Institute.

26. Operation Manual. Model 300 Continuous Writing Framing Camera. San Carlos, California: Beckman and Whitley, Inc., May 1966.

27. Prater, R. F. Hypervelocity Impact--Material Strength Effects on Crater Formation and Shock Propagation in Three Aluminum Alloys. Unpublished Dissertation, Wright-Patterson Air Force Base, Ohio: Air Force Institute of Technology, September 1970.

28. Preonas, D. D., and R. F. Prater. "Quantitative Motion Analysis for Rotating Mirror Framing Camera Records". Journal of the Society of Motion Picture and Television Engineers, 79 (7), pp. 586-589, 1970.

29. Rinehart, J. S. and J. Pearson. Behavior of Metals Under Impulsive Loads. New York: Dover Publications, Inc., 1965.

30. Smith, R. H. Investigation of Crater Growth and Ejecta Resulting from Hypervelocity Impact of Aluminum Spheres on Thick Aluminum Targets. AFML-TR-68-175, prepared from M. S. thesis performed for the Air Force Institute of Technology. Wright-Patterson Air Force Base, Ohio: AF Materials Laboratory, 1968.

31. Swift, H. F. The Air Force Materials Laboratory Hypervelocity Ballistic Range. AFML-TR-67-2. Wright-Patterson Air Force Base, Ohio: AFML, January 1967.

32. Swift, H. F., et al. "An Inexpensive Automatic Digital Film Reader". Journal of the Society of Photo-Optical Instrumentation Engineers, 8 (5), 185-186, August 1970.

33. Tate, F. "A Theory for the Deceleration of Long Rods After Impact", Journal for the Mechanics and Physics of Solids, 15:387-399, November 1967.

34. Turpin, W. C. Hypervelocity Perforation Mechanics of Thin Metal Plates. AFML-TR-69-203, prepared from M. S. thesis performed for the Air Force Institute of Technology. Wright-Patterson AFB, Ohio: AF Materials Laboratory, 1969.

35. Van Horn K. R. Aluminum Vol. I. Metals Park, Ohio: American Society for Metals, 1967.

36. Zel'dovich, Y. B. and Y. P. Raizer. Physics of Shock Waves and High Temperature Hydrodynamic Phenomena, Vol. II. New York. Academic Press, 1967.

Appendix A

Atmospheric Drag Effects

The velocity of the projectile was measured experimentally 82 cms ahead of the impact point. Since the fragment launch range is an open air range, a correction for drag effects must be considered in determining the impact velocity.

The drag force on the projectiles is given by the following relationship:

$$F_D = \frac{1}{2} C_D A \rho_a V^2 \tag{52}$$

where

C_D = dimensionless drag coefficient

ρ_a = the density of air

V = the projectile velocity

A = the frontal area of projectile

Using Newton's second law, Equation 52 can be expressed as:

$$-\frac{\pi}{6} D^3 \rho_p \frac{dV}{dt} = \frac{1}{2} C_D A \rho_a V^2 \tag{53}$$

where

D = projectile diameter

ρ_p = projectile density

Simplifying

$$\frac{dV}{dt} = -\frac{3 C_D \rho_a V^2}{4 D \rho_p} \tag{54}$$

and since $V = \frac{dx}{dt}$,

$$\frac{1}{V}\frac{dV}{dt} = \frac{dt}{dx}\frac{dV}{dt} = \frac{dV}{dx} = -\frac{3C_D\rho_a V}{4D\rho_p} \tag{55}$$

or in integral form, assuming C_D to be constant over the short distance x (82 cm)

$$\int_{V_o}^{V_p}\frac{dV}{V} = -\frac{3C_D\rho_a}{4D\rho_p}\int_0^x dx \tag{56}$$

Integrating yields:

$$\ln\frac{V_p}{V_o} = -\frac{3C_D\rho_a x}{4D\rho_p} \tag{57}$$

where

V_p = impact velocity

V_o = measured velocity

x = distance from measured point to impact point.

As seen in Ref 13, the drag coefficient for a sphere varies in an almost linear fashion for Mach number (velocity of projectile divided by local velocity of sound) between 2.0 and 5.5 (Ref 13:16-16). This approximate relationship is

$$C_D = 1 - \frac{0.08}{3.5}(M - 2.0) \qquad 2.0 \leqq M \leqq 5.5 \tag{58}$$

where M = Mach number. In the same reference, the drag coefficient for Mach numbers greater than 5.5 remains constant at 0.92.

The values of V2 (impact velocity corrected for drag) for shots fired on the fragment launch range (Table II) were calculated using the method described in this section. As an example, for shot 997 the drag force caused a loss of velocity from 1.998 km/sec to 1.946 km/sec or 2.6%.

The Eldorado Model 1400 counter timer used to record the elapsed time for velocity determination recorded the time to the nearest tenth of a microsecond. The distance x was measured to ± 0.25 cm and the velocity was calculated to the nearest 0.05 m/sec with a maximum error of ± 0.33%. Thus the drag losses are a factor of 8 larger than the experimental measuring error. Consequently, drag corrected velocities were used in all comparisons in this program for fragment launch range data.

The light-gas gun range is evacuated; thus the effect of drag becomes negligible as verified by observing the role of ρ_a in Equation 52. The accuracy of the streak camera system of velocity measurement used on the light-gas gun shots was within ± 0.25% (Ref 31:15).

Appendix B

Material Properties

The cratering theory developed requires a knowledge of certain material properties. These are: for the projectile--density and yield stress; for the target--density, Young's modulus, yield stress, and a tangent modulus, assumed to be constant for linear strain-hardening in true stress-true strain. Large strains and very high strain rates occur during the cratering process. The values selected to be used for the material constants in the cratering model should be obtained under conditions which closely reproduce the strains and strain rates of the cratering process.

A search of the literature revealed a paper by Holt, Babcock, Green, and Maiden titled "The Strain-Rate Dependence of the Flow Stress in Some Aluminum Alloys" (Ref 14:152-159). This paper contains stress-strain information at strain rates up to 10^3 in/in/sec for several aluminum alloys. Among these alloys were 1100-T0, 6061-T6, and 7075-T6. The material properties for these alloys presented in Table I were taken from this reference.

A further literature search failed to reveal any stress-strain information at high strain rates for the other alloys (6061-H and 2017-T4) used in this study. To obtain the material properties of the 6061-H and 2017-T4 alloys, a series of tests were run on the Air Force Materials Laboratory Split Hopkinson Bar facility. Figure 31 is a photograph of

Table I

Material Properties

Alloy	Density gm/cc	Yield Stress psi	Young's Modulus (Compression) psi	Tangent Modulus psi
1100-T0	2.71*	5,000**	10,020,000*	88,880**
2017-T4	2.7 *	53,000***	10,020,000*	
6061-H	2.7 *	12,200***	10,020,000*	93,900***
6061-T6	2.7 *	42,000**	10,020,000*	80,850**
7075-T6	2.8 *	60,000**	10,020,000*	

* Ref 21
** Ref 14
*** Split Hopkinson Pressure Bar Tests

the facility and Ref 25 contains a complete description of the facility. A brief description of the facility and its operation is included here along with a short treatment of theoretical principles involved.

Split Hopkinson Bar Procedure

Figure 31 is an overall view of the Split Hopkinson Bar System. The specimen is placed between the incident and transmitter pressure bars. Axial impact between the striker bar and the incident pressure bar produces the loading pulse. The striker bar is accelerated by a "sling-shot" type mechanism. A torsion bar provides the driving force

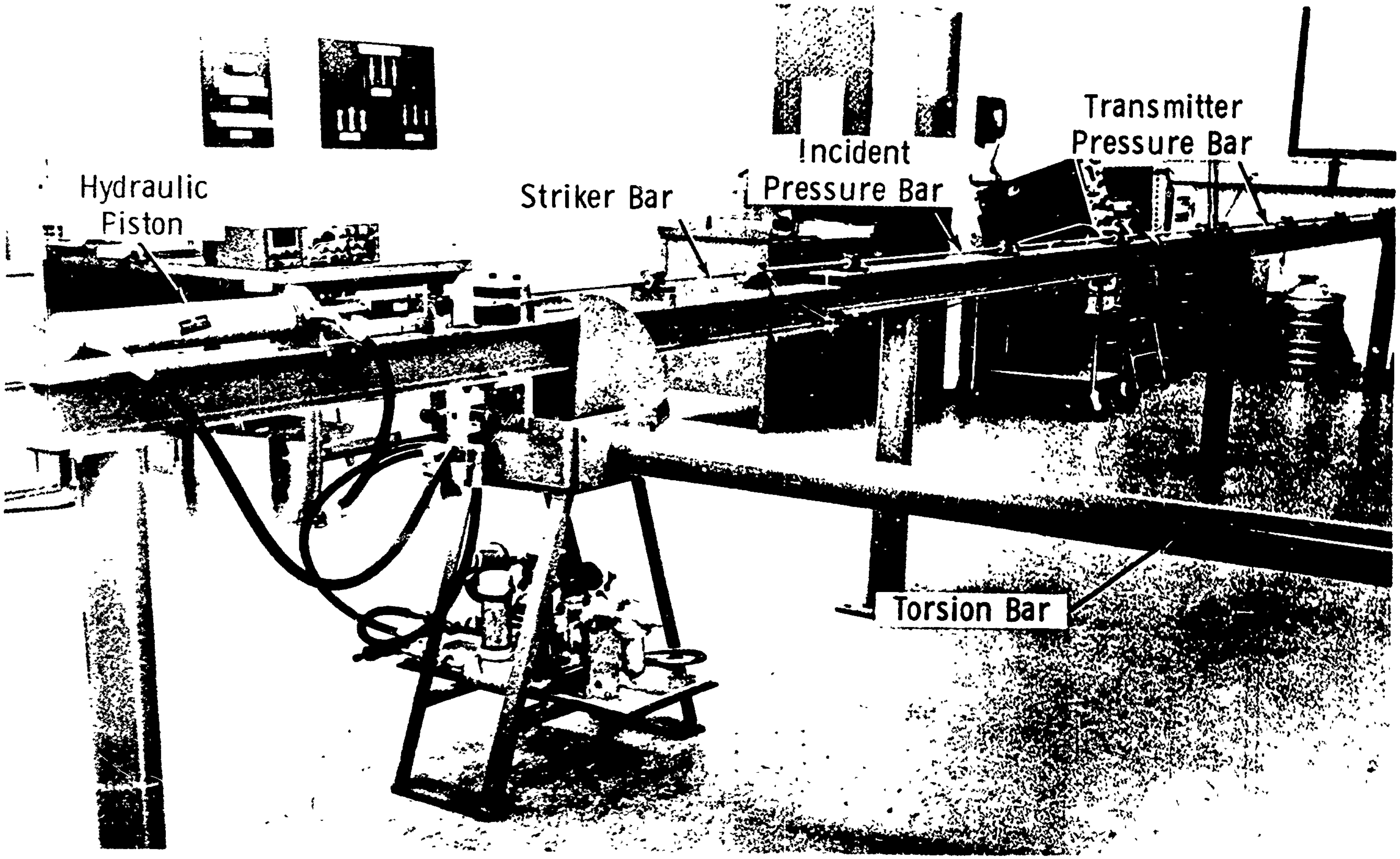

Fig. 31 Component Parts of Split Hopkinson Pressure Bar (Ref 25:4)

for this mechanism. This method of loading produces a pressure pulse of constant amplitude and finite duration. Since the striker bar unloads the incident pressure bar after the initial compression wave returns to the impact point, the pressure pulse in the incident bar is double the length of the striker bar, and has amplitude proportional to impact velocity. The impact velocity is varied by changing the release position of the "sling-shot" mechanism.

When the pressure pulse reaches the specimen, a portion is reflected and part is transmitted to the transmitter bar. The relative magnitude of these pulses will depend on the properties of the specimen. Due to the internal reflections in the short specimen and the relatively long duration of the loading pulse, the stress distribution in the specimen quickly approaches equilibrium.

The continuous strain-time histories of the three pulses, incident, reflected and transmitted are recorded by means of resistance strain-gages and associated electronic equipment. This information enables a determination of the force and displacement boundary conditions at both faces of the specimen (Ref 25:3-5).

Figure 32 shows a typical specimen used in these tests, and Fig. 36 shows the results of one test.

The following relations derived in Ref 25 are used to obtain the specimen stresses and strains.

$$\sigma_s = \frac{A}{A_s} E K_T V_\sigma \tag{59}$$

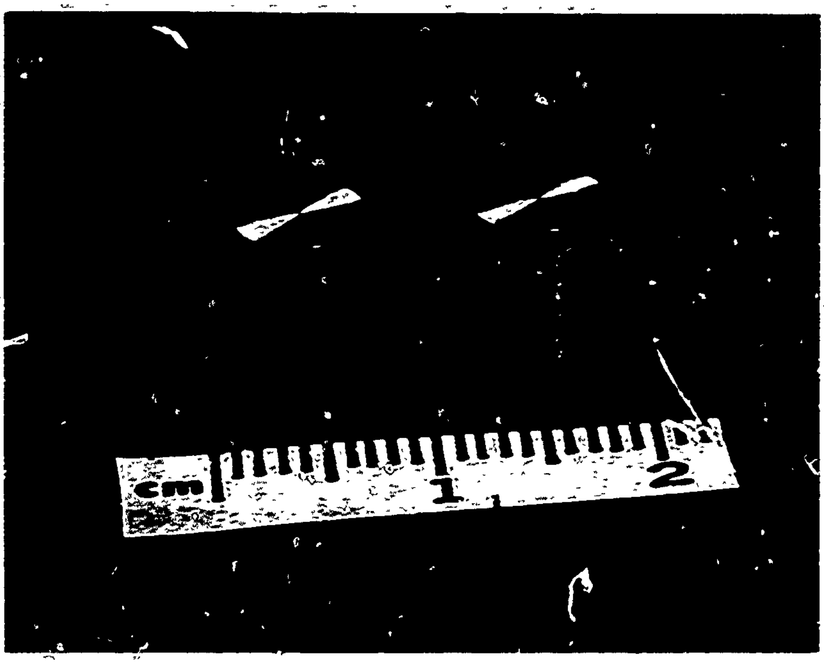

Fig. 32 Typical Split Hopkinson Pressure Bar Sample

$$\epsilon_s = \frac{2}{l_o} C_o K_i V_\epsilon \qquad (60)$$

Where

σ_s = Specimen normal stress

A = Cross sectional area of pressure bars

A_s = Cross sectional area of specimen

E = Young's modulus for pressure bars

V_σ = Voltage output of the stress portion of instrumentation package

C_o = Elastic wave velocity in pressure bars

l_o = Undeformed length of specimen

RC = Electronic integrator time constant

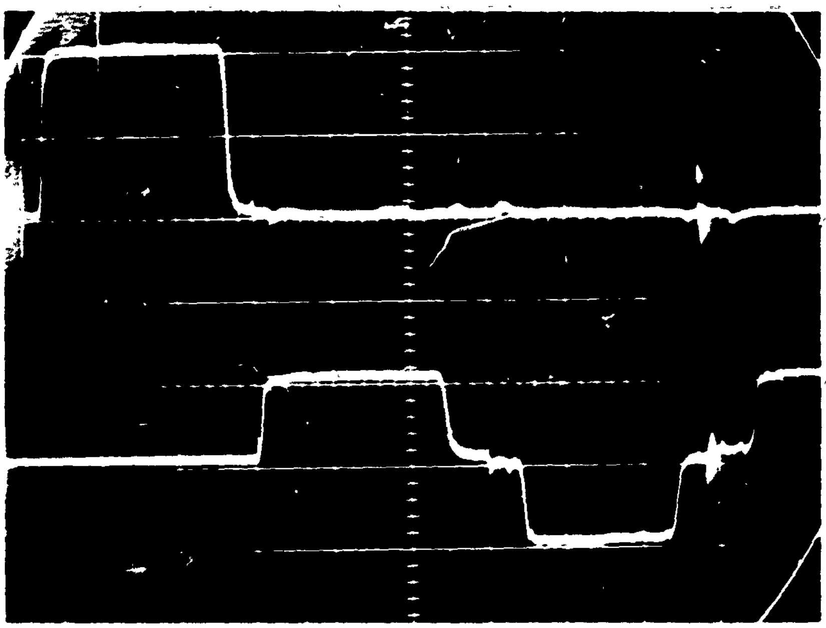

Fig. 33 Calibration-Upper-Trace is Strain Rate $\overline{V}_{\epsilon}$ (5×10^{-3} volts/division). Lower Trace is Stress (10×10^{-3} volts/division).

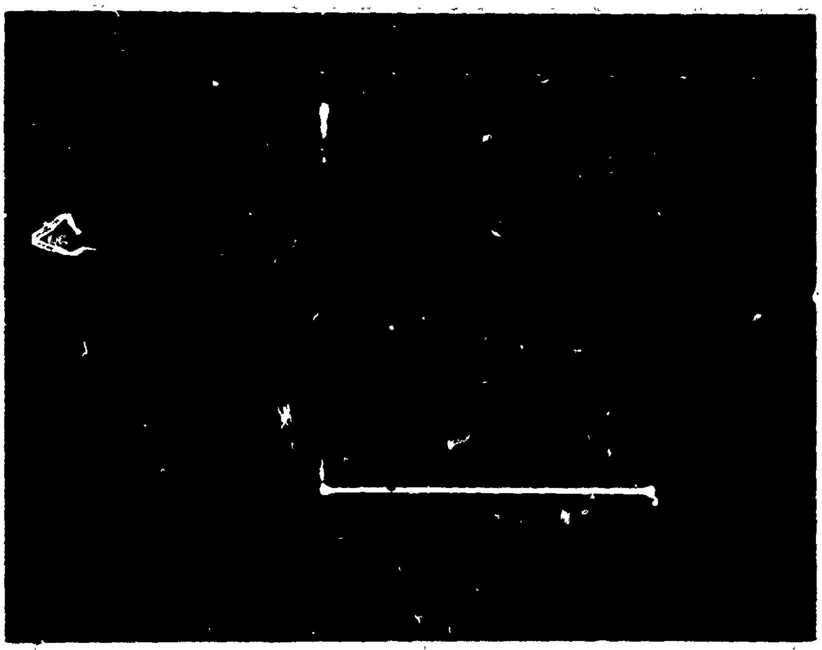

Fig. 34 Calibration-Vertical is Stress $\overline{V}_{\sigma}$(2×10^{-3} volts/division). Horizontal is Strain (0.5 volts/division).

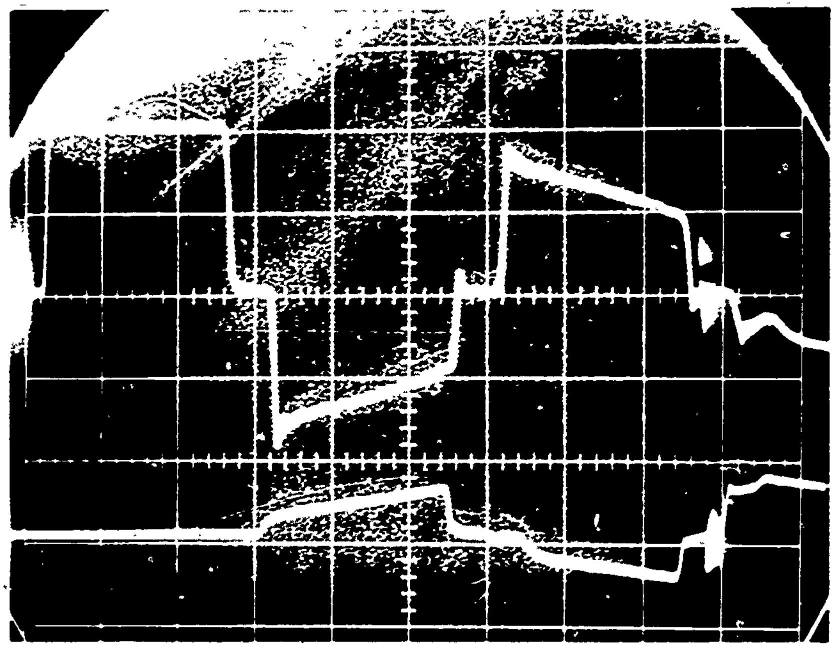

Fig. 35 6061-H Results Upper Trace is Strain Rate (5×10^{-3} volts/division). Lower Trace is Strain (10×10^{-3} volts/division).

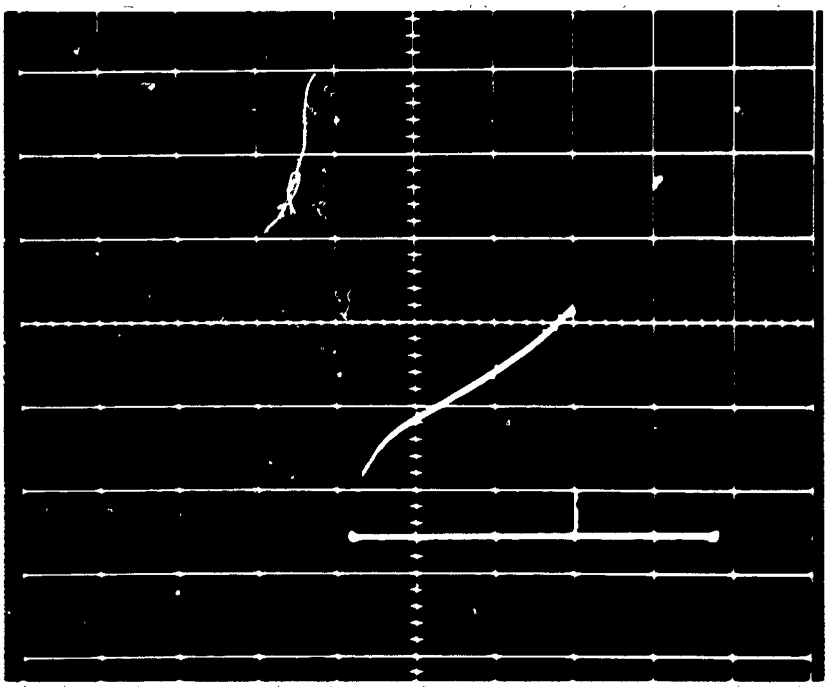

Fig. 36 6061-H Results-Vertical is Stress V_σ (2×10^{-3} volts/division). Horizontal Strain is V_ϵ (0.5 volts/division).

V_ϵ = Voltage output of the strain portion of instrumentation package.

K_I and K_T are calibration constants obtained by butting the two bars together without a specimen and loading the system. The equations for determining these values follows:

$$K_I = \frac{V_o}{2C_o}\frac{1}{\bar{V}_\epsilon} \tag{61}$$

$$K_T = \frac{V_o}{2C_o}\frac{1}{\bar{V}_\sigma} \tag{62}$$

Where

V_o = Impact velocity of striker bar

$\bar{V}_\epsilon$ = Voltage output of the strain rate portion of instrumentation package.

$\bar{V}_\sigma$ = Voltage output of the stress portion of instrumentation package.

(Ref 25:21-22)

The material properties for 6061-H and 2017-T4 aluminum alloys presented in Table I were obtained using this system and approach.

Brinell Hardness Test

As another check of the target material properties, a standard Brinell hardness test was run on a sample target. The results of this test are shown in Fig. 37. These results indicate a Brinell hardness number of 34.4 for the target material. Comparing this Brinell hardness number with the ones for 6061-T0 (Bhn 30) and 6061-T6 (Bhn 65) indicates the target material lies between the two (Ref 21:946).

Effect of Manufacture on Projectile Properties

Three projectiles of each alloy were annealed and returned to its initial temper in accordance with the requirements listed in Ref 21. These annealed projectiles were then fired at targets of the same target material and the resulting craters were compared with craters produced by unannealed projectiles.

There were six successful shots in this series. Those shots were:

Shot No.	Alloy
1077	1100-T0
1078	1100-T0
1082	7075-T6
1083	2017-T4
1084	2017-T4
1085	1100-T0

The shots for the 6061-T6 alloy projectile were voided due to the projectile striking the sabot plate in two shots and debris material from the shear disk impacting the target in the other.

The results of the six successful shots were plotted as triangles (Δ) in Figures 40, 41, 43, 44, and 45. From these figures, it can be concluded that manufacture did not introduce any noticeable change in the material properties of 1100-T0, 2017-T4, and 7075-T6 projectile.

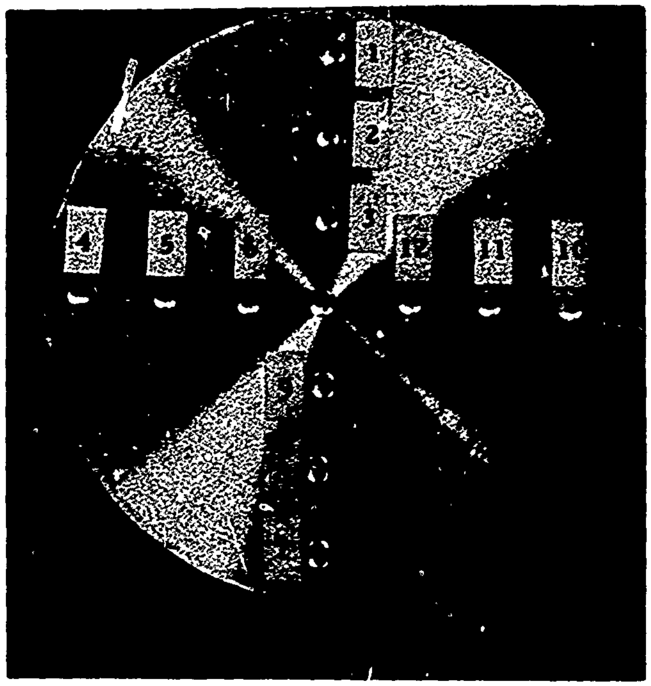

Fig. 37 Brinell Hardness Test Target

Brinell Hardness Test Results

10 mm Diameter Ball/Standard Brinell Test

	Diameter of Impression	Hardness Number (500 kg Load)
1.	4.2	34.4
2.	4.2	34.4
3.	4.2	34.4
4.	4.2	34.4
5.	4.2	34.4
6.	4.2	34.4
7.	4.2	34.4
8.	4.2	34.4
9.	4.2	34.4

Brinell Hardness Test Results (continued)

10 mm Diameter Ball/Standard Brinell Test

	Diameter of Impression	Hardness Number (500 kg Load)
10.	4.3	32.8
11.	4.2	34.4
12.	4.2	34.4
13.	4.2	34.4

With the lack of anything to indicate the contrary, the same result was assumed for the 6061-T6 alloy projectiles.

Appendix C

Shock Pressure Calculations

If the Hugoniot curve of a material is known, the measurement of one of the following variables behind a steady shock front allows calculations of all the others:

ρ = the density of shocked target material

U_p = the material velocity at any point

U_s = the shock speed at any point

P = the hydrodynamic pressure at any point

(Ref 27:106).

In this experimental program the material velocity U_p was selected as the variable to measure experimentally. This measurement was accomplished using the "flyer" technique described in Section III. This method provided a position-time record of the flyer by means of a high-speed movie camera.

The use of three flyers on the target and the inability to precisely control the projectile impact point necessitated correcting the free surface (flyer) velocity for both shock incidence angle and distance from impact point.

In Ref 27 a first order adjustment ignoring the effect of surface waves and shear waves generated upon reflections is developed. This relationship is

$$V_{fs(adjusted)} = \frac{V_{fs(measured)}}{\text{Cosine } \theta} \qquad (63)$$

where θ is the acute angle between the line perpendicular to the rear surface through the impact point and the line joining the impact point and the center of the specific flyer (Ref 27:314-315).

The method of correcting for the differing distances of flyers from impact point was to normalize the flyer velocity to a standard distance (target thickness). To accomplish this, the standard distance was taken to be the target thickness measured along the extended projectile trajectory. The normalized velocity is given by

$$V_s = V_m \left(\frac{D_m}{D_s} \right)^N \tag{64}$$

where V_s is the normalized velocity, V_m is the measured velocity, D_m is the measured distance between impact point and center of flyer, D_s is the standard distance, and N is an experimentally determined parameter. For this series of experiments, D_s was the target thickness and N was taken as 2.1 (Ref 27:172).

The values of VF1, VF2, and VF3 shown in Table III are the flyer velocities corrected for angle and distance as discussed. The values of D_m and θ are given in Table IV. Figure 39 shows a typical output of the computer program used for reducing the flyer film data and Fig. 38 shows typical results of the photographic technique used.

Using the well known free surface approximation

$$V_{fs} = 2\,U_p \tag{65}$$

where V_{fs} is the free surface flyer velocity and U_p is the material velocity behind the shock front (Ref 10:181). The shock pressure is

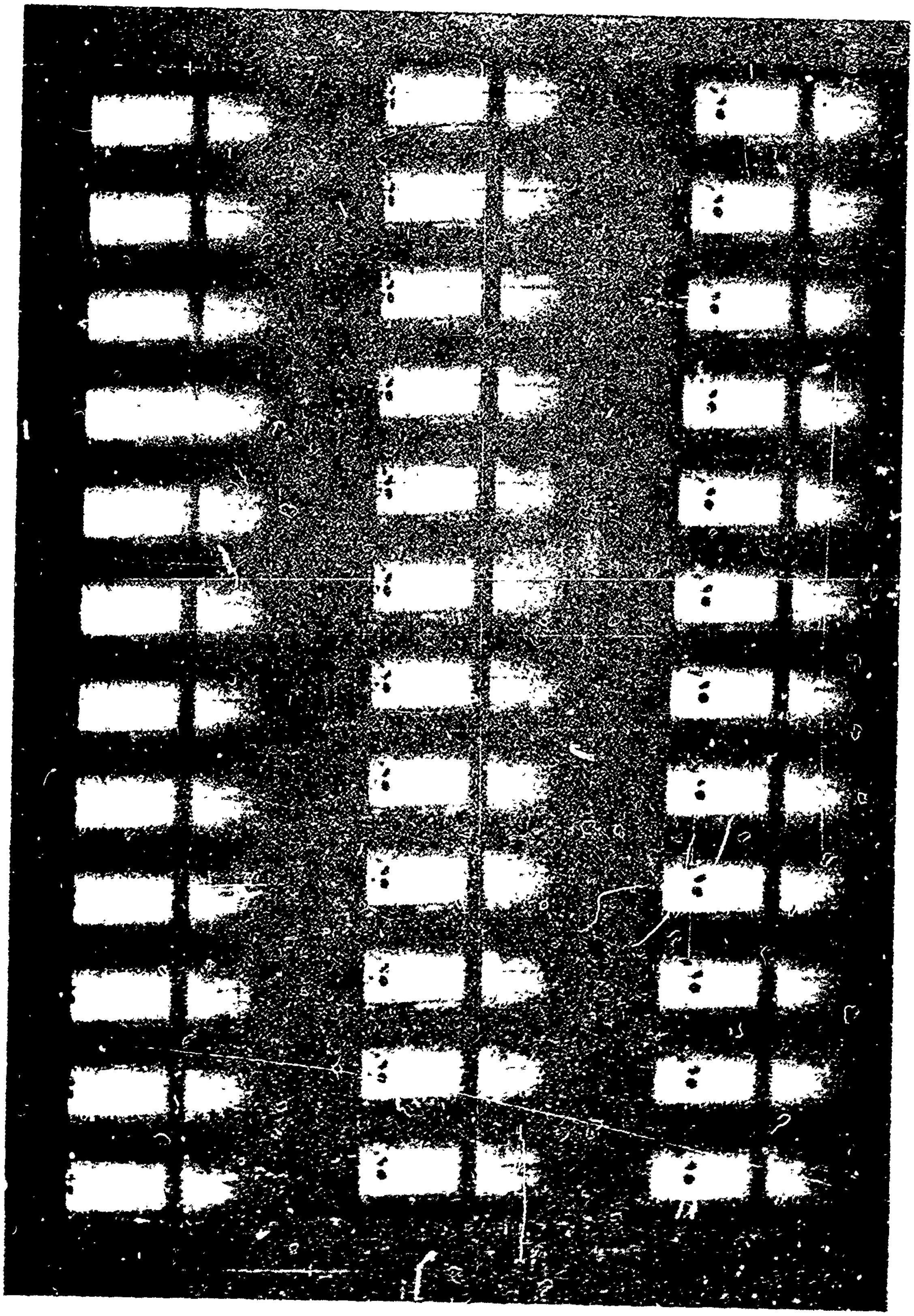

Fig. 38 Typical High-Speed Camera Results

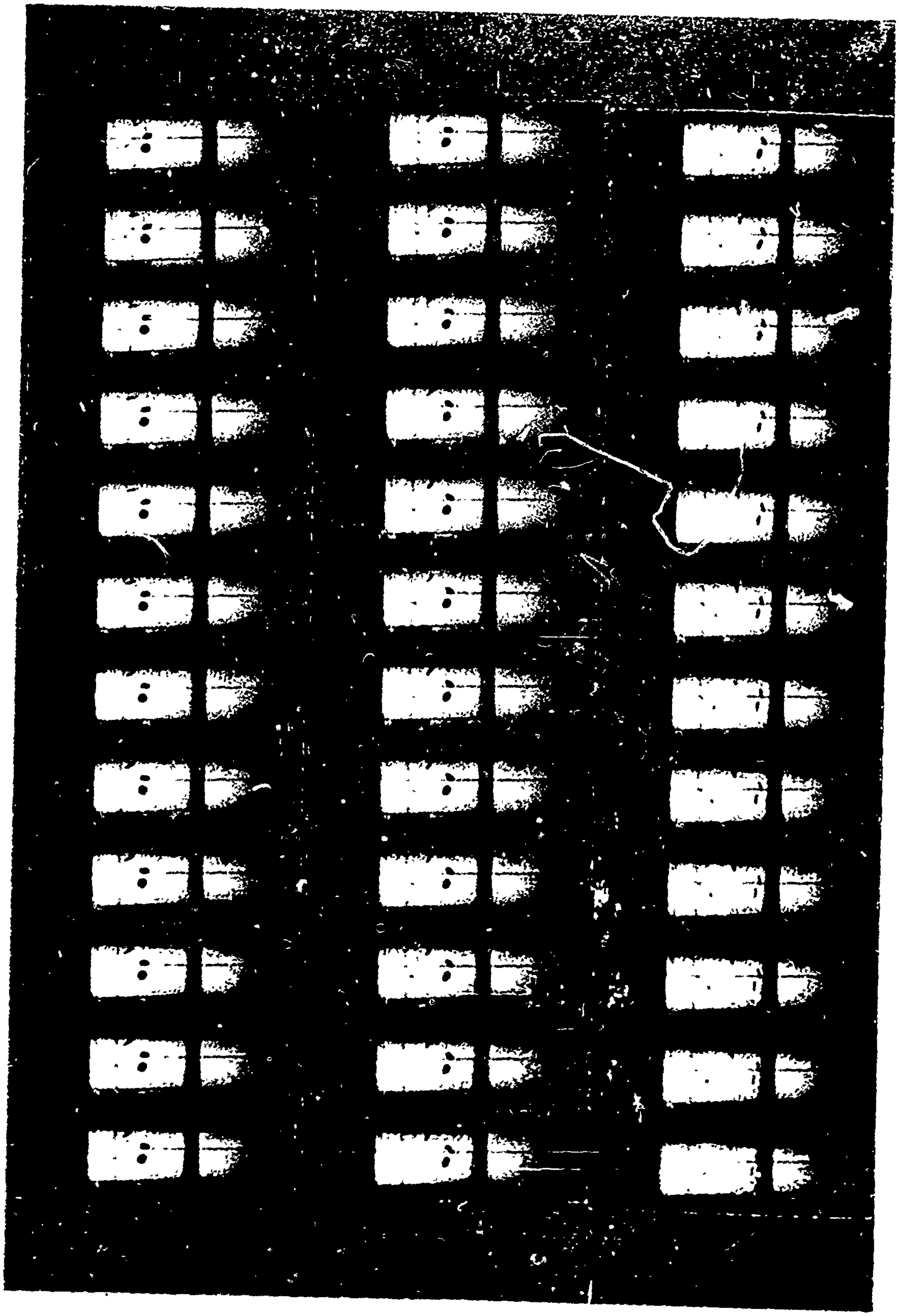

Fig. 38 (cont.) Typical High-Speed Camera Results

DYNAFAX
REDUCED DATA
SHOT NO.2911
ITEM NO. 1

A= 2.5147 VELOCITY -121.906 M/SEC STANDARD DEVIATION 0.1118 CM
THE VELOCITY DEVIATION IS 2.674 M/SEC (2.19 PERCENT)

FRAME NO.	Y POS. CM	TIME MSEC	DEVIATION CM
1	2.631	0.	0.116
3	1.592	0.078	0.031
5	0.535	0.156	-0.073
7	-0.478	0.235	-0.132
9	-1.437	0.313	-0.137
11	-2.146	0.391	0.108
13	-3.120	0.469	0.087

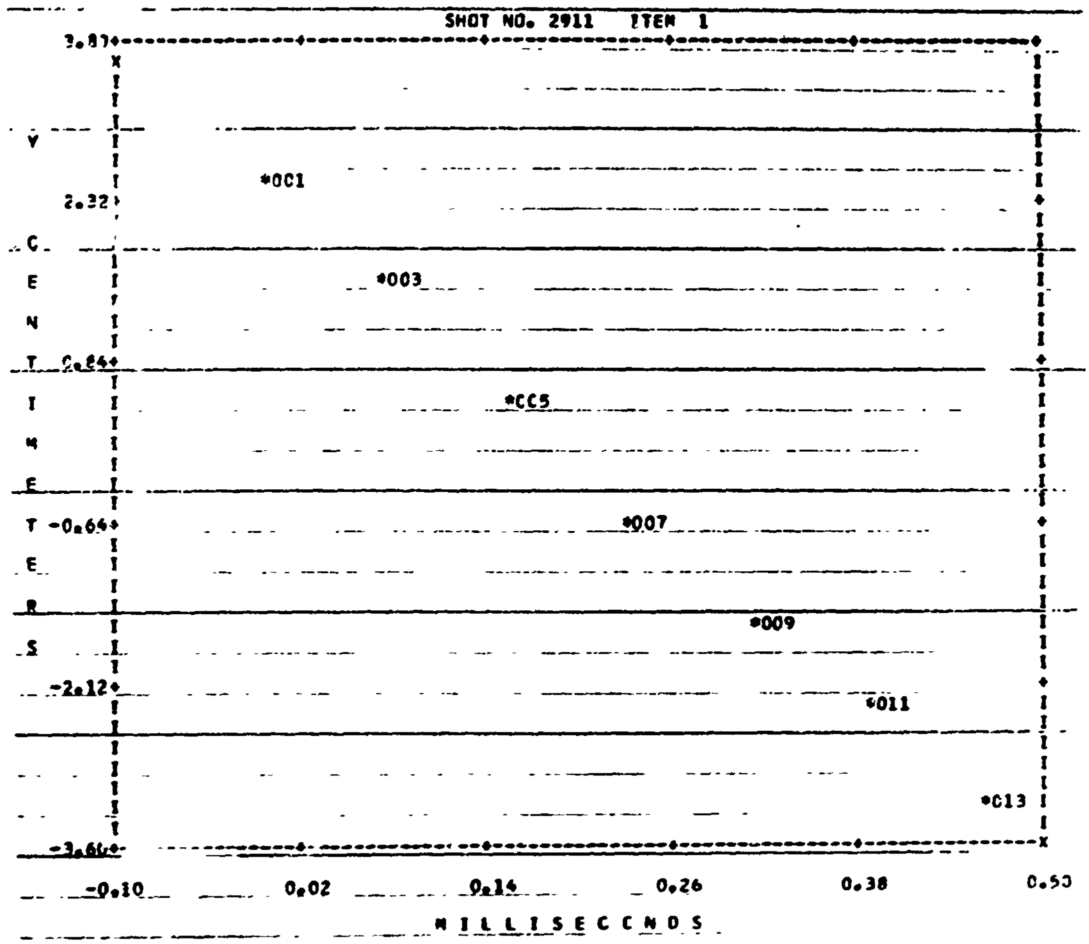

Fig. 39 Typical Output of Computer Program for Reducing Flyer Film Data

determined from the Hugoniot equation

$$P = \rho_o U_s U_p \tag{66}$$

where P is shock pressure, ρ_o is the initial target density, and U_s is shock front velocity. For many materials, the shock speed and particle velocity have been found to be adequately described by

$$U_s = C + S U_p \tag{67}$$

where C is the bulk speed of sound in the material, and S is an equation of state constant. Thus knowing the material velocity, C and S enables a calculation of the shock pressure.

The values of C and S for 6061-H target material were not available in the literature, but in Ref 27, it is shown that the aluminum alloys all have essentially the same shock speed. Consequently, the following shock speed relationship for 1100-T0 alloy was used in lieu of one being available for 6061-H:

$$U_s = 5.144 + 0.76 U_p \tag{68}$$

(Ref 22).

The values of pressure shown in Table III were computed using these relationships.

Appendix D

Cratering Experimental Results

This appendix is divided into three parts as listed below:

PART I

GRAPHS OF CRATER DIAMETER VS.
IMPACT VELOCITY FOR THE PROJECTILE
MATERIALS USED IN THIS STUDY

PART II

GRAPHS OF CRATER DEPTH VS.
IMPACT VELOCITY FOR THE PROJECTILE
MATERIALS USED IN THIS STUDY

PART III

TABLE OF CRATERING EXPERIMENTAL RESULTS

PART I

GRAPHS OF CRATER DIAMETER VS.
IMPACT VELOCITY FOR THE PROJECTILE
MATERIALS USED IN THIS STUDY

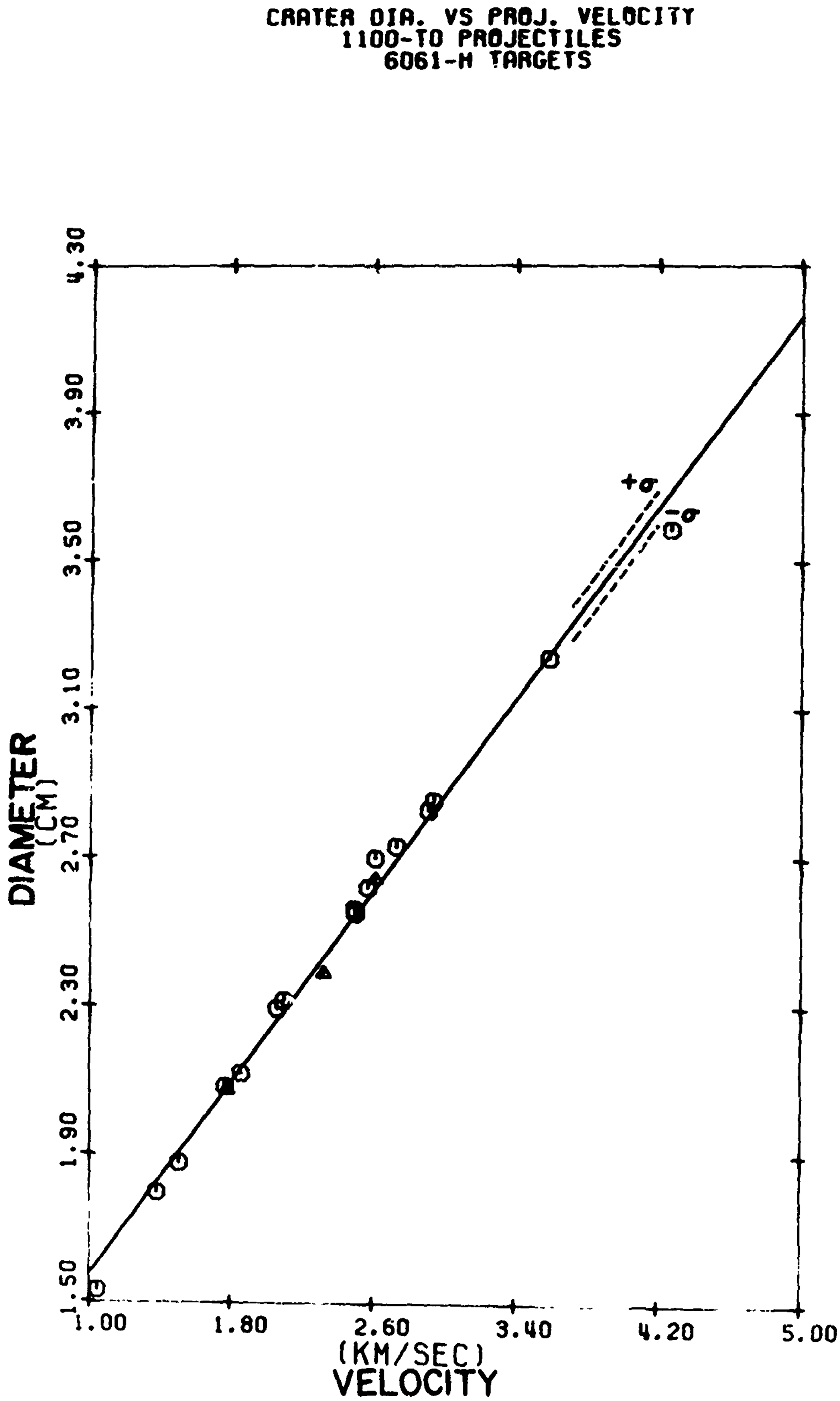

Fig. 40 Graph of Crater Diameter vs. Projectile Velocity for 1100-T0 Projectiles

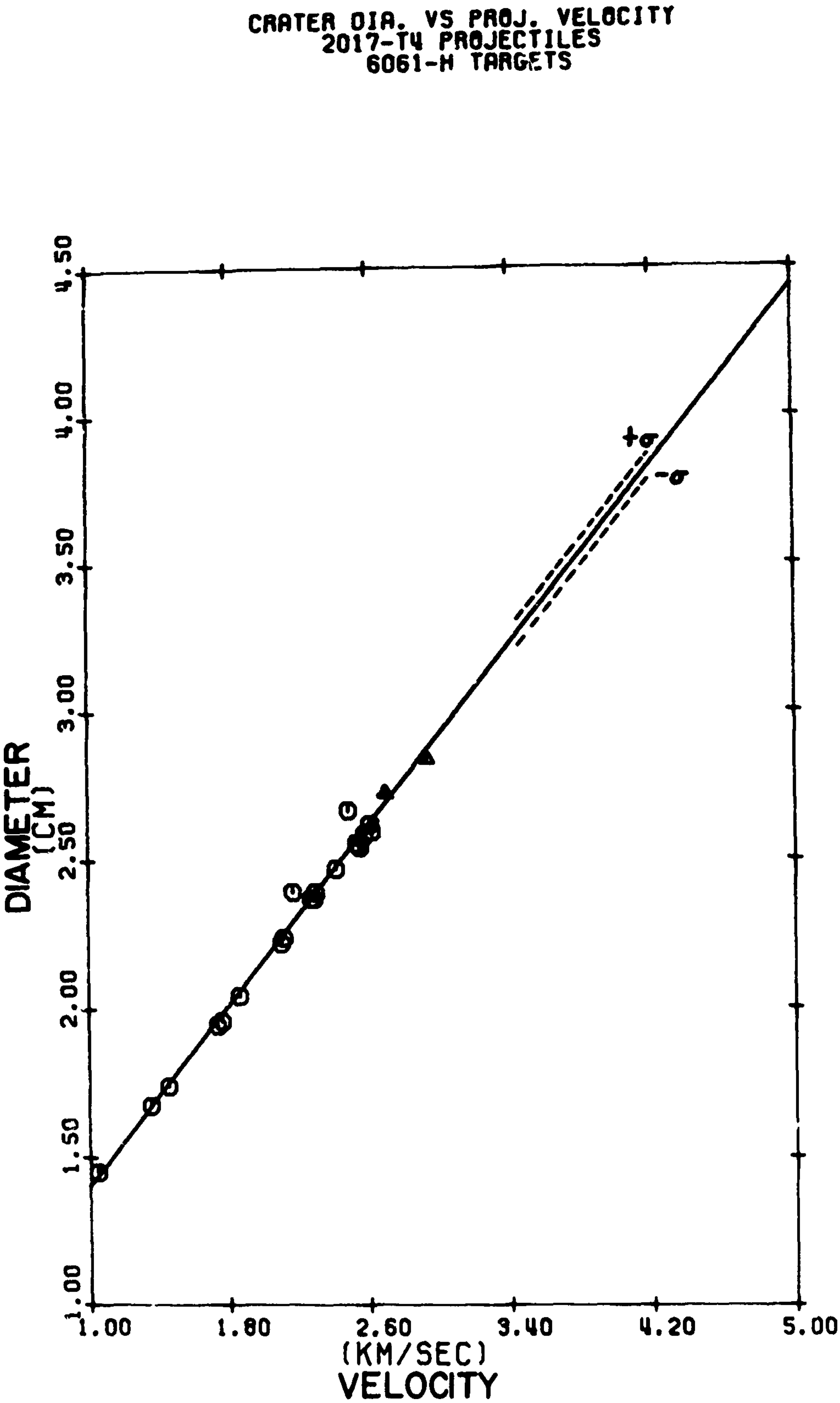

Fig. 41 Graph of Crater Diameter vs. Projectile Velocity for 2017-T4 Projectiles

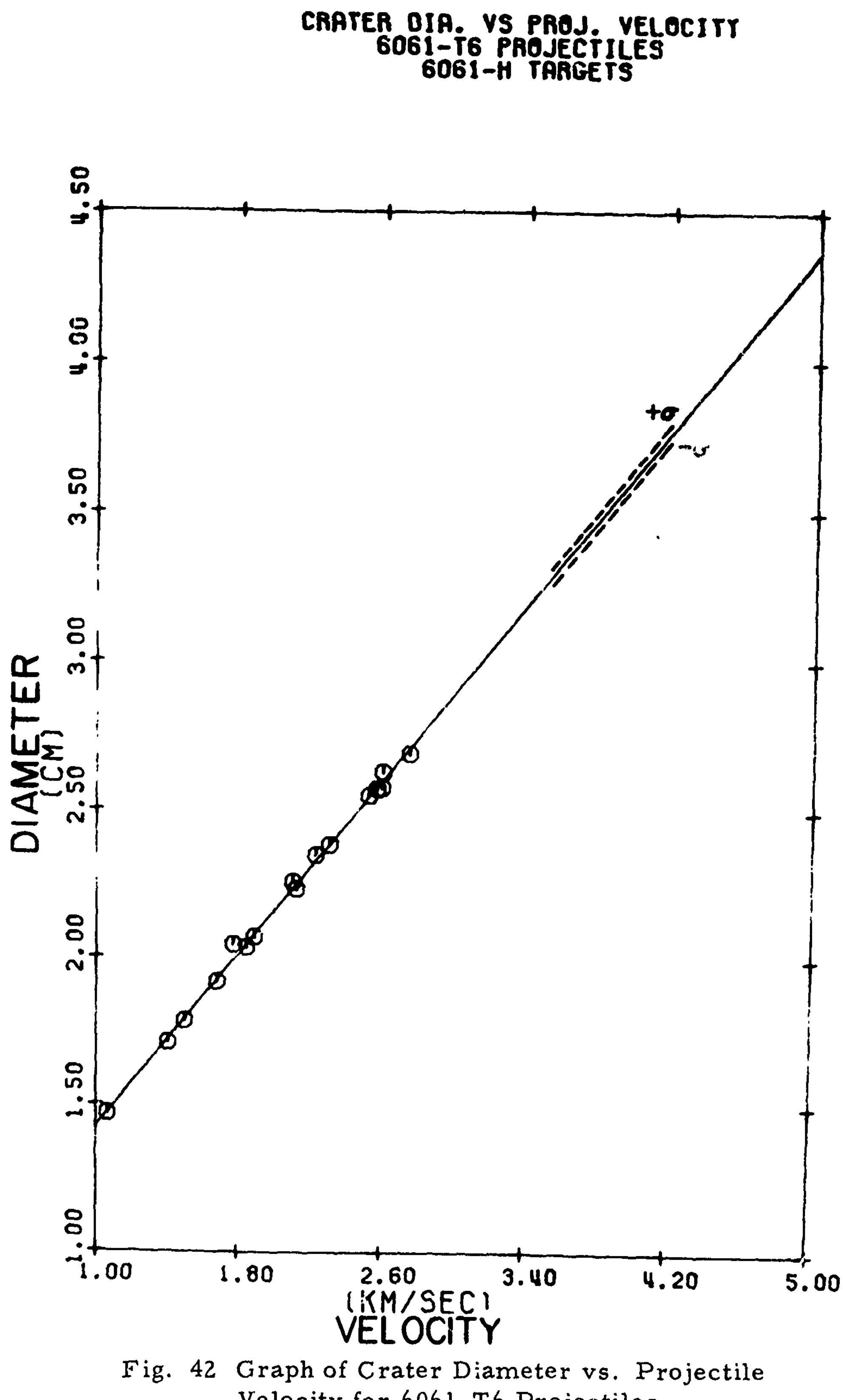

Fig. 42 Graph of Crater Diameter vs. Projectile Velocity for 6061-T6 Projectiles

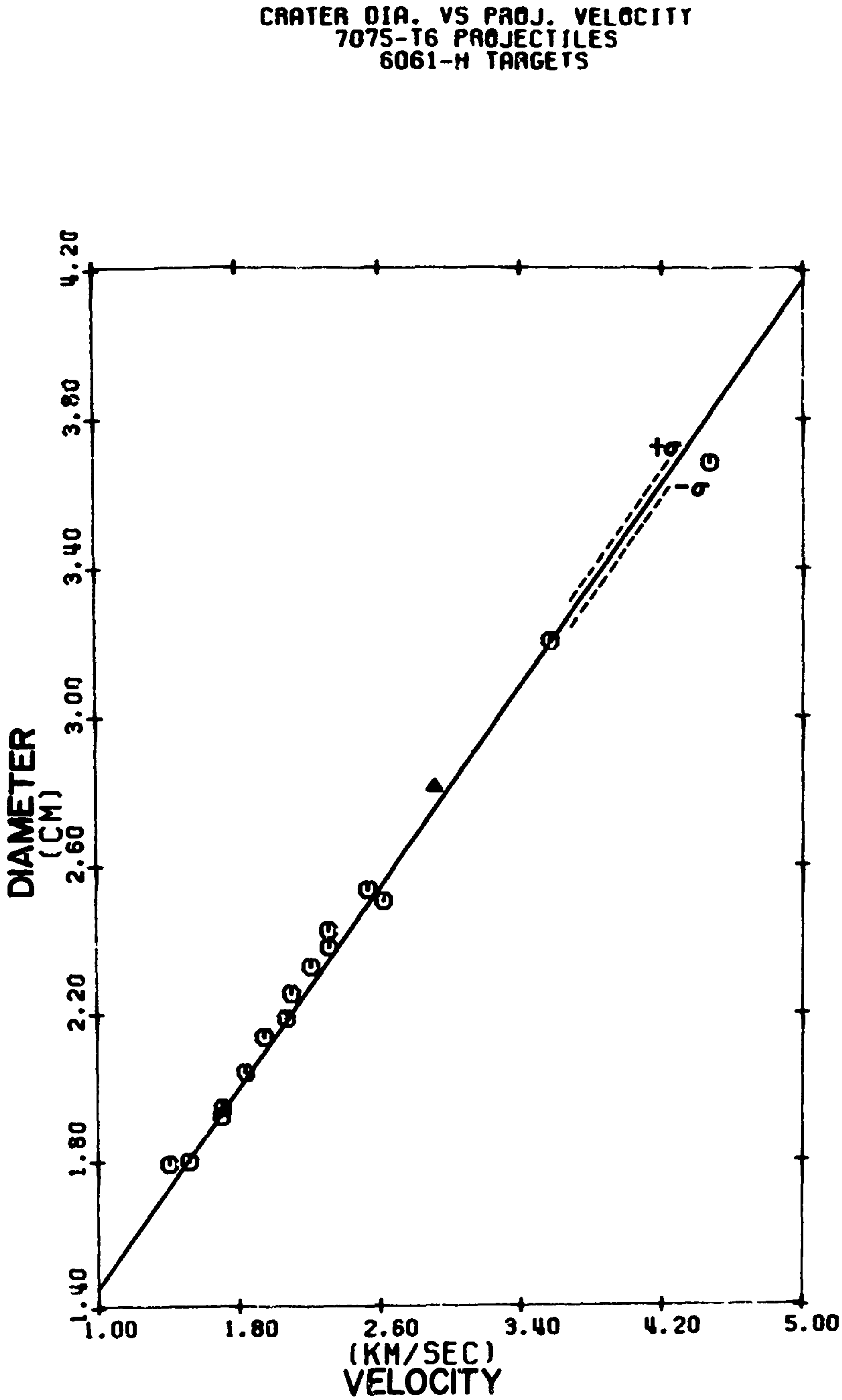

Fig. 43 Graph of Crater Diameter vs. Projectile Velocity for 7075-T6 Projectiles

PART II

GRAPHS OF CRATER DEPTH VS.
IMPACT VELOCITY FOR THE PROJECTILE
MATERIALS USED IN THIS STUDY

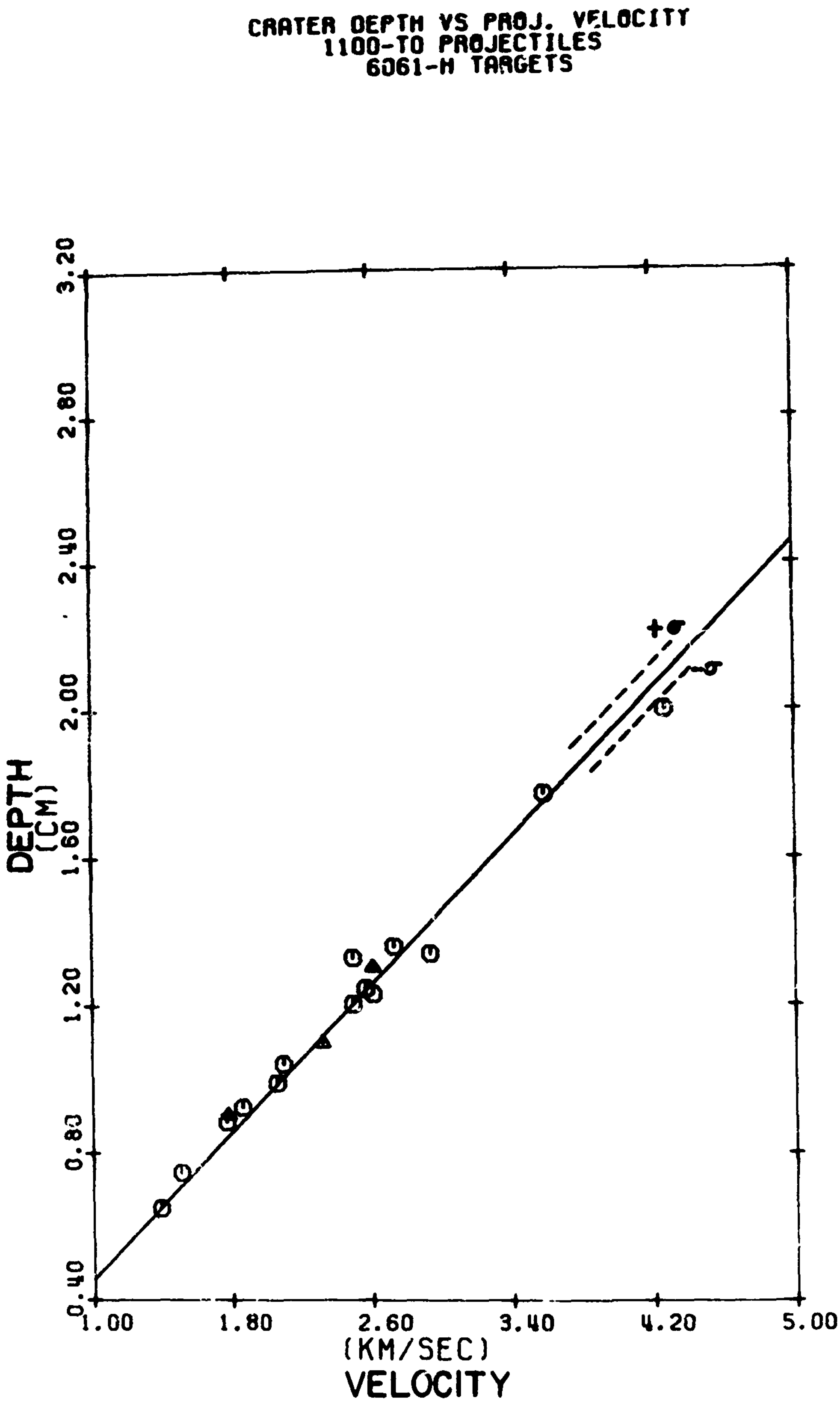

Fig. 44 Graph of Crater Depth vs. Projectile Velocity for 1100-T0 Projectiles

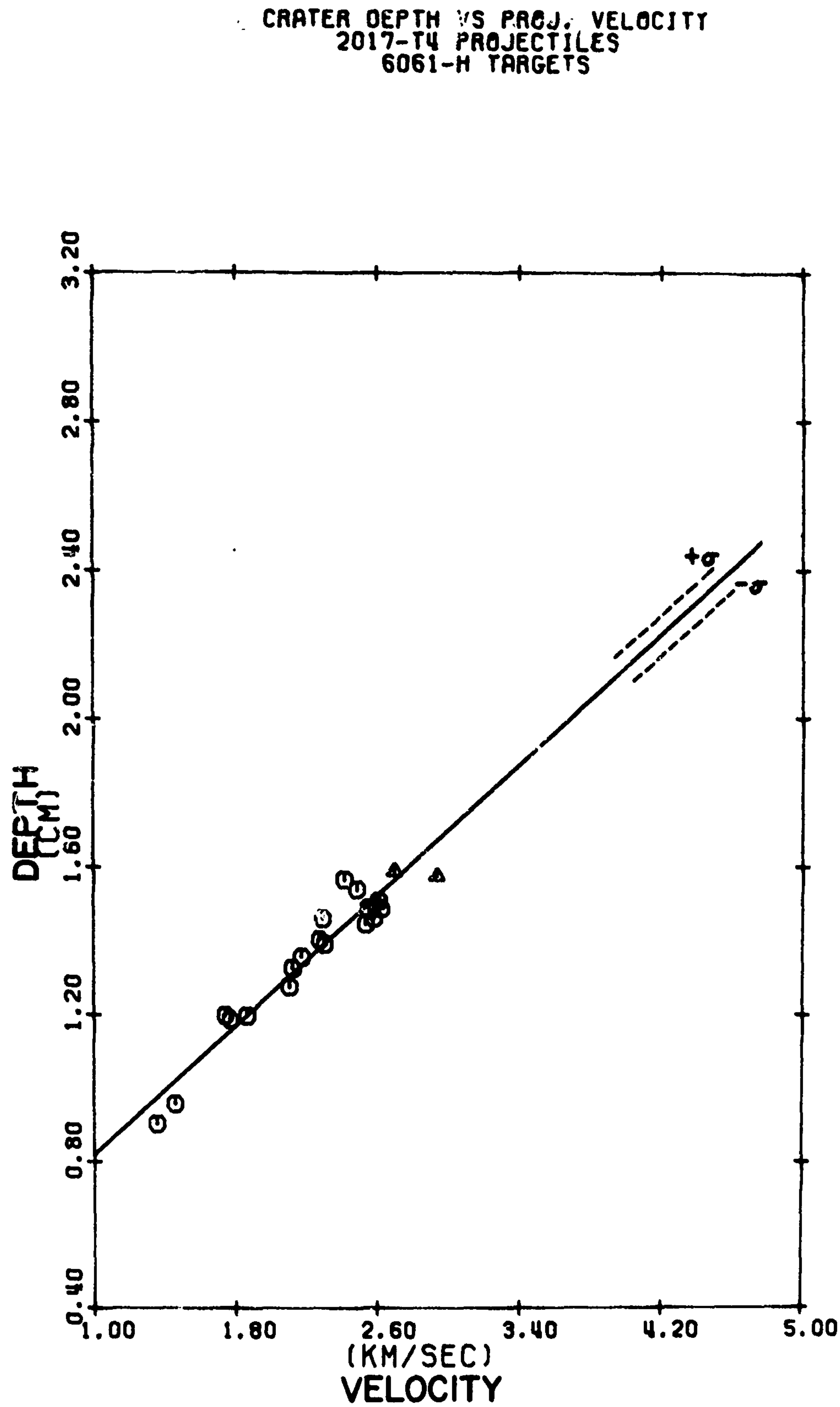

Fig. 45 Graph of Crater Depth vs. Projectile Velocity for 2017-T4 Projectiles

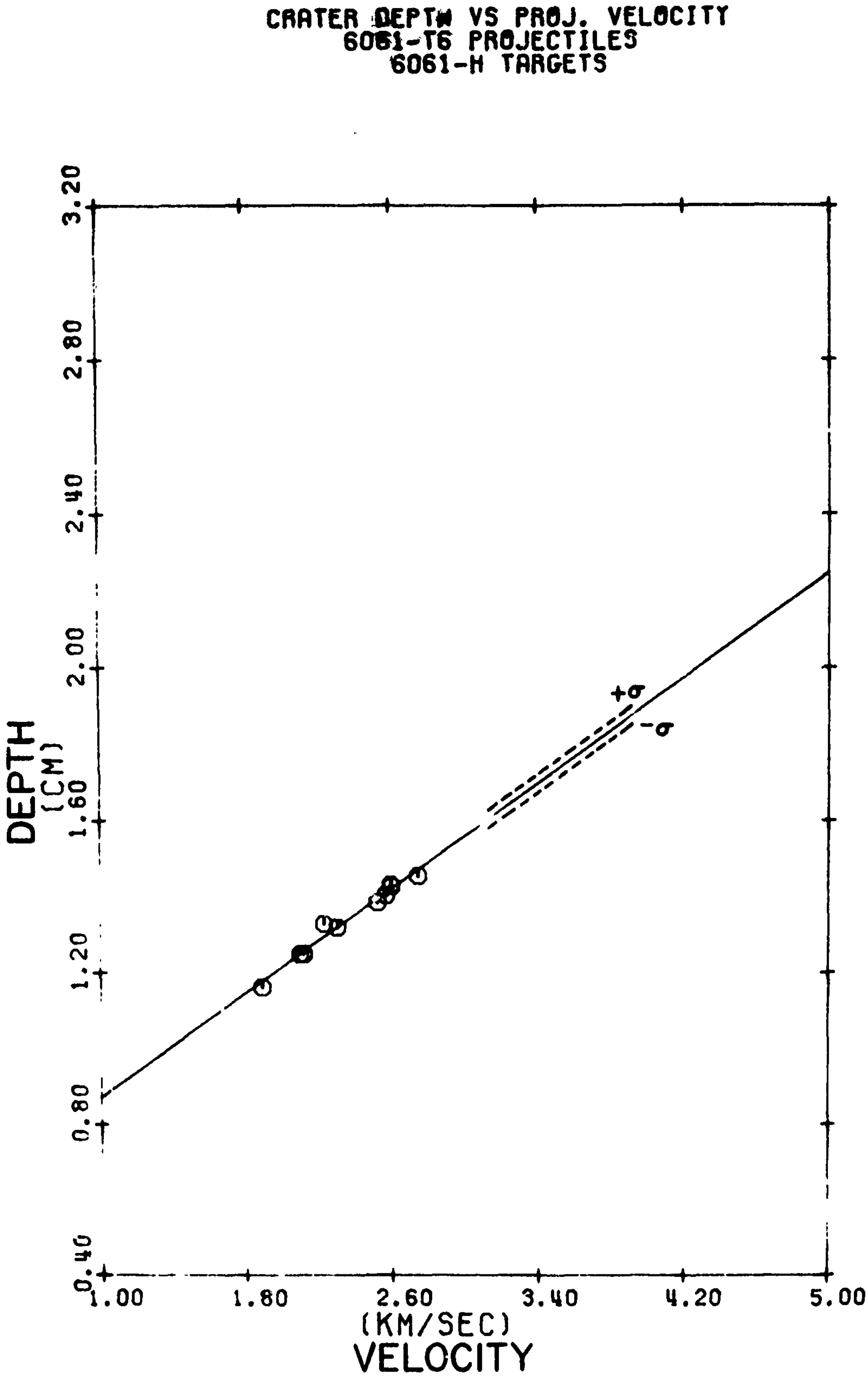

Fig. 46 Graph of Crater Depth vs. Projectile Velocity for 6061-T6 Projectiles

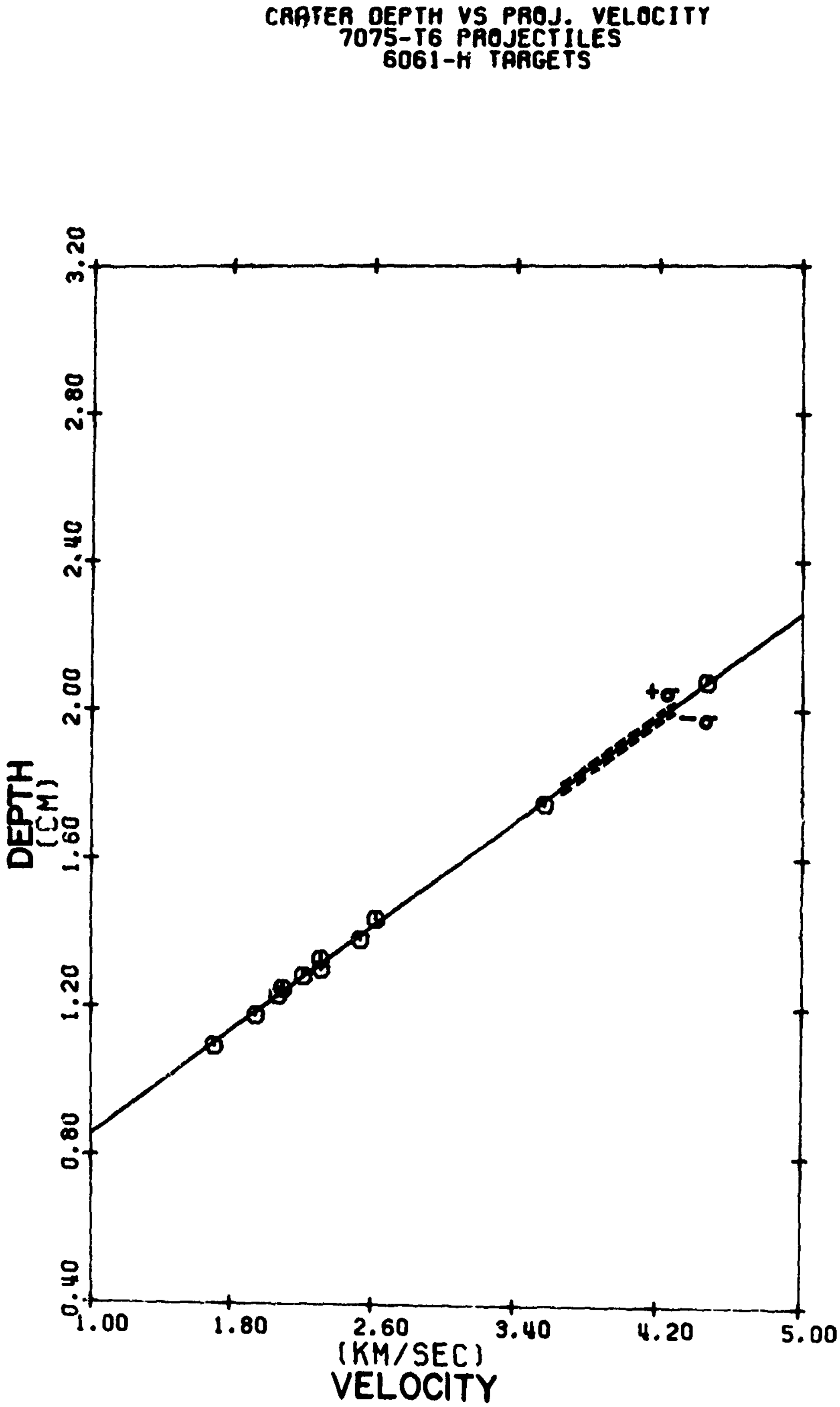

Fig. 47 Graph of Crater Depth vs. Projectile Velocity for 7075-T6 Projectiles

PART III

TABLE OF CRATERING EXPERIMENTAL RESULTS

TABLE II
CRATERING EXPERIMENTAL RESULTS SUMMARY

SHOT NO.	PROJ. MAT.	TGT. MAT.	PROJ. MASS (GRAMS)	PROJECTILE VELOCITY V1 (KM/SEC)	PROJECTILE VELOCITY V2 (KM/SEC)	PROJECTILE VELOCITY V2 (FT/SEC)	CRATER DIA. (CM)	CRATER DEPTH (CM)
997	7075-T6	6061-H	1.2251	1.9978	1.9461	6384.8207	2.141	1.178
998	1100-T0	6061-H	1.2274	2.1551	2.0994	6887.7590	2.316	1.043
1000	7075-T6	6061-H	1.2261	1.7531	1.7075	5602.0018	1.948	1.096
1001	2017-T4	6061-H	1.2667	2.2281	2.1723	7126.8303	2.311	1.358
1003	7075-T6	6061-H	1.2199	2.1556	2.0995	6888.2736	2.256	1.250
1004	7075-T6	6061-H	1.2225	2.1250	2.0699	6791.0051	2.189	1.232
1005	1100-T0	6061-H	1.2388	2.1172	2.0629	6768.1884	2.294	0.992
1007	2017-T4	6061-H	1.2672	2.3628	2.3036	7557.8296	2.394	1.392
1008	2017-T4	6061-H	1.2663	2.3327	2.2742	7461.2942	2.371	1.404
1010	6061-T6	6061-H	1.2273	2.1586	2.1029	6899.1264	2.258	1.251
1013	6061-T?	6061-H	1.2281	2.2917	2.2325	7324.6115	2.349	1.331
1014	2017-T4	6061-H	1.2784	2.5977	2.5332	8311.1653	2.555	1.447
1015	1100-T0	6061-H	1.2347	2.5635	2.4976	8194.3608	2.551	1.331
1016	1100-T0	6061-H	1.2355	2.5613	2.4956	8187.6127	2.562	1.206
1017	6061-T6	6061-H	1.2280	2.5955	2.5285	8295.5249	2.551	1.388
1021	2017-T4	6061-H	1.2664	2.6894	2.6220	8602.4508	2.595	1.489
1022	2017-T4	6061-H	1.2736	2.6784	2.6116	8568.4033	2.621	1.510
1023	2017-T4	6061-H	1.2753	2.6474	2.5815	8469.4597	2.585	1.463
1024	2017-T4	6061-H	1.2732	2.6178	2.5526	8374.5483	2.543	1.491
1026	6061-T6	6061-H	1.2228	2.6435	2.5750	8448.0724	2.574	1.407
1027	6061-T6	6061-H	1.2243	2.3671	2.3058	7564.8008	2.384	1.321
1028	2017-T4	6061-H	1.2719	2.3500	2.2914	7517.7452	2.371	1.461
1029	2017-T4	6061-H	1.2675	2.4774	2.4154	7924.4048	2.470	1.567
1034	2017-T4	6061-H	1.2719	1.3903	1.3545	4443.7747	1.676	0.904
1035	6061-T6	6061-H	1.2259	1.4484	1.4099	4625.5943	1.713	*
1036	1100-T0	6061-H	1.2280	1.4252	1.3872	4551.3417	1.797	0.650
1037	7075-T6	6061-H	1.2245	1.4455	1.4069	4615.9200	1.794	*
1038	6061-T6	6061-H	1.2241	1.5443	1.5034	4932.5562	1.787	*
1039	7075-T6	6061-H	1.2257	2.3708	2.3094	7576.7952	2.427	1.331
1040	6061-T6	6061-H	1.2249	2.6721	2.6029	8539.8009	2.631	1.431
1041	7075-T6	6061-H	1.2281	2.6910	2.6215	8600.7056	2.507	1.438
1042	6061-T6	6061-H	1.2260	2.6682	2.5992	8527.5426	2.579	1.434
1044	1100-T0	6061-H	1.2329	2.6374	2.5696	8430.3933	2.620	1.247
1046	7075-T6	6061-H	1.2258	1.5604	1.5192	4984.2434	1.802	*
1047	2017-T4	6061-H	1.2737	1.4946	1.4564	4778.2745	1.740	0.958
1048	1100-T0	6061-H	1.2291	1.5519	1.5110	4957.4480	1.877	0.748
1049	6061-T6	6061-H	1.2247	1.7292	1.6840	5525.0663	1.919	*
1050	7075-T6	6061-H	1.2256	1.7487	1.7031	5587.7269	1.925	*

* PROJECTILE REMAINED IN CRATER
** SHOT FIRED ON LIGHT GAS GUN
V1 MEASURED VELOCITY
V2 VELOCITY CORRECTED FOR DRAG

TABLE II (continued)
CRATERING EXPERIMENTAL RESULTS SUMMARY

SHOT NO.	PROJ. MAT.	TGT. MAT.	PROJ. MASS (GRAMS)	PROJECTILE VELOCITY V1 (KM/SEC)	PROJECTILE VELOCITY V2 (KM/SEC)	PROJECTILE VELOCITY V2 (FT/SEC)	CRATER DIA. (CM)	CRATER DEPTH (CM)
1051	6061-T6	6061-H	1.2240	1.9418	1.8915	6205.6996	2.071	1.164
1052	2017-T4	6061-H	1.2732	1.8107	1.7655	5792.1729	1.960	1.188
1053	1100-TO	6061-H	1.2313	1.8164	1.7696	5805.6473	2.084	0.886
1054	6061-T6	6061-H	1.2283	1.8212	1.7740	5820.3596	2.045	1.138
1056	1100-TO	6061-H	1.2330	1.9114	1.8622	6109.5809	2.120	0.925
1057	2017-T4	6061-H	1.2852	1.9094	1.8622	6109.6669	2.045	1.198
1058	7075-T6	6061-H	1.2258	2.3751	2.3136	7590.5873	2.383	1.303
1059	6061-T6	6061-H	1.2263	2.1792	2.1229	6964.7465	2.234	1.251
1060	2017-T4	6061-H	1.2750	2.1576	2.1039	6902.6292	2.223	1.277
1061	2017-T4	6061-H	1.2760	2.1746	2.1205	6956.9372	2.241	1.327
1063	7075-T6	6061-H	1.2261	1.0764	1.0470	3435.0105	1.218	*
1064	1100-TO	6061-H	1.2353	1.0760	1.0468	3434.5040	1.532	0.273
1065	6061-T6	6061-H	1.2264	1.0967	1.0668	3499.8516	1.470	*
1066	2017-T4	6061-H	1.2711	1.0721	1.0438	3424.6461	1.450	*
1067	7075-T6	6061-H	1.2263	2.2712	2.2125	7258.8365	2.330	1.284
1068	7075-T6	6061-H	1.2276	2.6022	2.5349	8316.7006	2.538	1.384
1069	2017-T4	6061-H	1.2715	2.5513	2.4877	8161.6386	2.666	1.541
1070	1100-TO	6061-H	1.2326	2.8023	2.7302	8957.3973	2.731	1.361
1071	6061-T6	6061-H	1.2267	2.8231	2.7501	9022.6375	2.692	1.458
1072	7075-T6	6061-H	1.2234	1.8896	1.8407	6038.9053	2.044	*
1073	6061-T6	6061-H	1.2282	1.8959	1.8470	6059.5605	2.036	*
1074	2017-T4	6061-H	1.2730	1.7825	1.7378	5701.5225	1.946	1.199
1077	1100-TO	6061-H	1.2355	1.8288	1.7818	5845.7839	2.075	0.905
1078	1100-TO	6061-H	1.2336	**	2.6110	8566.6908	2.642	1.304
1079	1100-TO	6061-H	1.2335	**	2.9390	9642.8589	2.854	1.341
1080	1100-TO	6061-H	1.2336	**	2.6110	8566.6908	2.699	1.232
1081	1100-TO	6061-H	1.2336	**	2.9080	9541.1479	2.827	*
1082	7075-T6	6061-H	1.2244	**	2.9120	9554.2719	2.812	*
1083	2017-T4	6061-H	1.2729	**	2.9340	9626.4539	2.837	1.576
1084	2017-T4	6061-H	1.2727	**	2.6960	8845.5759	2.724	1.590
1085	1100-TO	6061-H	1.2330	2.3825	2.3212	7615.4866	2.389	1.100
2905	6061-T6	6061-H	1.2350	**	4.4470	14590.6068	3.292	1.960
2906	1100-TO	6061-H	1.2250	**	4.2680	14003.3077	3.586	2.002
2907	7075-T6	6061-H	1.2390	**	4.4700	14666.0698	3.684	2.076
2908	1100-TO	6061-H	1.2250	**	3.5850	11762.3849	3.238	1.773
2911	7075-T6	6061-H	1.2250	**	3.5670	11703.3269	3.205	1.748

* PROJECTILE REMAINED IN CRATER
** SHOT FIRED ON LIGHT GAS GUN
V1 MEASURED VELOCITY
V2 VELOCITY CORRECTED FOR DRAG

Appendix E

Shock Pressure Data Summary

TABLE III
FLYER EXPERIMENTAL RESULTS SUMMARY

SHOT NO.	PROJ. MAT.	PROJ. VELOCITY (KM/SEC)	VF1 (M/SEC)	P1 (KBARS)	VF2 (M/SEC)	P2 (KBARS)	VF3 (M/SEC)	P3 (KBARS)
997	7075-T6	1.9461	*	*	11.39	0.034	10.59	0.029
998	1100-T0	2.0994	*	*	23.44	0.143	19.01	0.094
1019	6061-T6	2.1029	30.38	0.240	31.71	0.262	30.61	0.244
1024	2017-T4	2.5526	56.58	0.833	46.05	0.552	41.16	0.441
1026	6061-T6	2.5750	42.69	0.474	54.83	0.782	54.21	0.765
1056	1100-T0	1.8622	18.92	0.093	24.89	0.161	23.65	0.146
1057	2017-T4	1.8622	15.46	0.062	13.55	0.048	22.26	0.129
1058	7075-T6	2.3136	37.93	0.374	45.18	0.485	53.47	0.744
1059	6061-T6	2.1229	31.18	0.253	30.50	0.242	29.65	0.229
1061	2017-T4	2.1205	33.99	0.301	37.00	0.356	35.71	0.332
1068	7075-T6	2.5349	64.11	1.069	69.71	1.264	65.86	1.061
1069	2017-T4	2.4877	35.75	0.332	55.47	1.115	76.25	1.512
1070	1100-T0	2.7302	51.02	0.677	57.05	1.170	70.78	1.303
1071	6061-T6	2.7501	28.76	0.215	46.81	0.570	50.39	0.651
1072	7075-T6	1.8407	*	*	7.47	0.015	6.89	0.012
1073	6061-T6	1.8470	11.82	0.036	16.09	0.067	11.06	0.032
1074	2017-T4	1.7378	*	*	7.62	0.015	11.94	0.037
1077	1100-T0	1.7818	*	*	10.25	0.027	13.49	0.047
1078	1100-T0	2.6110	70.61	1.297	73.21	1.394	72.45	1.365
1081	1100-T0	2.9080	93.36	2.257	93.10	2.255	91.27	2.167
1082	7075-T6	2.9120	101.91	2.702	104.04	2.816	104.46	2.839
2907	7075-T6	4.4700	254.97	14.362	210.67	11.546	229.74	13.750
2908	1100-T0	3.5850	181.28	8.549	183.77	8.785	186.25	9.024
2911	7075-T6	3.5670	140.54	5.138	129.30	4.349	126.95	4.193

* FLYER NOT VISIBLE ON FILM

TABLE IV
FLYER EXPERIMENTAL RESULTS

SHOT NO.	PROJ. MAT.	VEL. (KM/SEC)	DM1 (CM)	DM2 (CM)	DM3 (CM)	THEA1 (RAD.)	THEA2 (RAD.)	THEA3 (RAD.)
997	7075	1.9461	5.1187	5.0833	5.1469	0.1231	0.0360	0.1614
998	1100	2.0994	5.1094	5.0881	5.1656	0.1073	0.0565	0.1823
1019	6061	2.1029	5.1551	5.0846	5.1129	0.1709	0.0424	0.1135
1024	2017	2.5526	5.1667	5.2113	5.3518	0.1830	0.2251	0.3200
1025	6061	2.5750	5.2499	5.1175	5.0820	0.2551	0.1211	0.0283
1056	1100	1.8622	5.4481	5.2402	5.1234	0.3697	0.2479	0.1303
1057	2017	1.8622	5.4315	5.2402	5.1410	0.3617	0.2479	0.1542
1058	7075	2.3136	5.2160	5.1057	5.0933	0.2288	0.1004	0.0724
1059	6061	2.1229	5.1347	5.0896	5.1435	0.1461	0.0615	0.1572
1061	2017	2.1205	5.1684	5.0927	5.1157	0.1852	0.0706	0.1182
1068	7075	2.5249	5.1219	5.0883	5.1535	0.1280	0.0571	0.1691
1069	2017	2.4877	5.2446	5.1613	5.1753	0.2512	0.1777	0.1922
1070	1100	2.7302	6.2821	6.0057	5.8058	0.6289	0.5626	0.5048
1071	6061	2.7501	5.1902	5.1324	5.1727	0.2064	0.1431	0.1897
1072	7075	1.8407	5.2599	5.1783	5.1835	0.2693	0.1951	0.2002
1073	6061	1.8470	5.1054	5.0841	5.1617	0.0998	0.0403	0.1782
1074	2017	1.7378	5.1910	5.1114	5.1501	0.2072	0.1109	0.1399
1077	1100	1.7818	5.2504	5.1191	5.0847	0.2555	0.1237	0.0432
1078	1100	2.6110	5.2868	5.1367	5.0876	0.2806	0.1487	0.0319
1081	1100	2.9080	5.1233	5.0915	5.1585	0.1301	0.0672	0.1745
1082	7075	2.9120	5.1388	5.0805	5.1212	0.1515	0.0140	0.1270
2907	7075	4.4700	5.1267	5.0869	5.1443	0.1359	0.0485	0.1582
2908	1100	3.5850	5.1387	5.0850	5.1302	0.1513	0.0441	0.1450
2911	7075	3.5670	5.2007	5.2387	5.3715	0.2158	0.2468	0.3510

Appendix F

AFML Experimental Data

Table V

AFML Experimental Data

Shot No.	Target Material	Projectile Material	Projectile Diameter (mm)	Projectile Weight (gm)	Projectile Velocity (km/sec)	Crater Diameter (cm)	Crater Depth (cm)
2385	1100-T0	2017-T4	3.18	0.0458	7.053	1.68	.96
2386	1100-T0	2017-T4	3.18	0.0459	7.034	1.65	.96
2387	1100-T0	2017-T4	3.18	0.046	7.01	1.59	.86
2455	1100-T0	2017-T4	3.18	0.0458	7.065	1.6	.89
2456	1100-T0	2017-T4	3.18	0.0459	7.01	1.62	.90
2457	1100-T0	2017-T4	3.18	0.0458	7.01	1.61	.89
2459	1100-T0	2017-T4	3.18	0.0457	6.891	1.59	.88
2460	1100-T0	2017-T4	3.18	0.0459	6.906	1.58	.90
2461	1100-T0	2017-T4	3.18	0.0499	6.815	1.61	.87
2462	1100-T0	2017-T4	3.18	0.0458	6.9	1.62	.96
2463	1100-T0	2017-T4	3.18	0.0457	6.76	1.61	.96

Table V (continued)

AFML Experimental Data

Shot No.	Target Material	Projectile Material	Projectile Diameter (mm)	Projectile Weight (gm)	Projectile Velocity (km/sec)	Crater Diameter (cm)	Crater Depth (cm)
2464	1100-T0	2017-T4	3.18	0.046	6.873	1.59	.86
2503	1100-T0	2017-T4	3.18	0.0459	7.162	1.68	.97
2504	1100-T0	2017-T4	3.18	0.0458	7.214	1.65	.9
2505	1100-T0	2017-T4	3.18	0.0457	7.135	1.65	.93
2515	1100-T0	2017-T4	3.18	0.0458	6.398	1.42	.81
2516	1100-T0	2017-T4	3.18	0.0457	5.026	1.36	.77
2517	1100-T0	2017-T4	3.18	0.0459	5.072	1.36	.76
2686	6061-T6	2017-T4	6.35	0.3732	6.858	2.74	1.41
2688	6061-T6	2017-T4	6.35	0.3732	6.699	2.43	1.59
2694	6061-T6	2017-T4	6.35	0.3727	6.794	2.836	1.44